DESIGN, MANUFACTURING, AND CHARACTERIZATION OF ELASTOMERIC DEVICES FOR BIOMEDICAL IMPLANTS

A Dissertation

Presented to the Faculty of the Graduate School

of Cornell University

In Partial Fulfillment of the Requirements for the Degree of

Doctor of Philosophy

by

Sanlin Sky Robinson

December 2017

DESIGN, MANUFACTURING, AND CHARACTERIZATION OF ELASTOMERIC DEVICES FOR BIOMEDICAL IMPLANTS

Sanlin Sky Robinson, Ph. D.

Cornell University 2017

3D printing has been used extensively in medicine for education, surgical planning, and diagnostic assistance. It has also proven effective for load bearing structural implants, for addressing craniomaxillofacial reconstruction, and airway obstructions. To date, however, there are no clinical examples of additively manufactured soft devices. In this thesis, I will present an approach for the rapid prototyping of a patient-specific left atrial appendage (LAA) occluder via 3D printing and static molding of inflatable silicone/polyurethane balloons. The LAA is a structure known to be highly variable in geometry and the primary source of stroke for patients with atrial fibrillation. I describe the design workflow, fabrication, and deployment of these patient-specific occluders as a proof-of-concept, and show their efficacy using 3D printed anatomic models, *in vitro* flow loops, and an *in vivo* large animal model. My work demonstrates the first patient-specific LAA occluder. This occluder could offer a non-pharmacological alternative to current methods, particularly in cases where the morphology causes occlusion to be challenging. Additionally, the design process and manufacturing methods I present could be used in any application where patient-specificity and soft materials are necessary.

Proper delivery and deployment of LAA occluders requires exquisite knowledge of spatial orientation in delicate and complex anatomy. While real-time 3D ultrasound offers excellent navigation and interaction with soft-tissues, it requires a high level of expertise and implant materials with distinct ultrasound signatures for proper visualization and orientation. By incorporating sensory feedback into the skin of occluders, it could mitigate the need for complex imaging and expert skills. These skins

would provide direct feedback of their degree of inflation as well as contact pressure with surrounding tissues. In my thesis, I will show my work on soft, stretchable sensors that can be directly printed onto pre-fabricated devices via direct ink writing. This printing technique uses two inks—an ionically conductive hydrogel and an electrically insulating silicone—which are patterned and photopolymerized into capacitive sensors. When printed onto a pneumatically actuated haptic device, these sensors enabled the detection of a compressive force of ~2 N, and an internal pressurization of as low as ~ 10 kPa.

BIOGRAPHICAL SKETCH

Sanlin Robinson was born in Corpus Christi, Texas in the Fall of 1988. As a child, she spent most of her time outdoors, building forts, climbing trees, and exploring. At the age of 12 her family moved to the US Virgin Islands, where she further developed her great love and respect for nature and biology.

At 14 years old, she enrolled part-time in classes at the University of the Virgin Islands (UVI). Her passion for science was ignited by the wonderful professors there who pushed her to take challenging courses and perform research. Her drive and love of learning has only increased since then. Starting college at such a young age granted her the ability to explore her many areas of interest; she spent time learning chemistry, biology, theater, foreign languages, and SCUBA diving. She also took some time away from her studies to travel to Mexico and Spain, to increase her knowledge in Spanish language, history, and art. She graduated *magna cum laude* from UVI in 2011 with a Bachelor of Science in Chemistry.

In August 2011, she moved to Ithaca, NY to pursue a doctoral degree in Materials Science and Engineering at Cornell University. She joined Professor Robert Shepherd's Organic Robotics Lab where she worked on developing polymeric inks for extrusion printing of soft, compliant materials. In August 2015, she traveled to Weill Cornell Medical in New York, NY to work with Professor Bobak Mosadegh and Professor Simon Dunham, on the development and fabrication of an elastomeric biomedical implant for one year. She returned to Cornell's Ithaca campus to work on directly 3D printing these biomedical devices. Throughout her PhD, Sanlin has developed a strong intuition for the design, manufacturing, and characterization of soft materials systems.

To the ants and the stars, thank you for giving me perspective.

ACKNOWLEDGMENTS

First and foremost, I would like to thank my advisor, Rob Shepherd. He has always been incredibly kind, encouraging, and insightful. I am so happy and grateful to have been a member of his lab! I would like to thank Professor Bobak Mosadegh and Professor Simon Dunham; they were great mentors to me while I was in NYC, they helped me to grow as a scientist and engineer. I would like to thank James Min and Millie Gomez for giving me the opportunity to be a part of the Dalio Institute of Cardiovascular Imaging at Weill Cornell Medical. Their expertise in radiology and cardiology were invaluable to me. I would like to thank my committee members Professor Emmanuel Giannelis and Professor Christopher Ober for their excellent advice throughout my PhD. I would like to thank Professor Archer, Professor Van Dover, and Michele Conrad, I had a very challenging first year as a PhD student and these wonderful people were very kind and compassionate toward me. Of course, I would like to thank my lab mates Huichan, Kevin, Ben, Bryan, TJ, James, Shuo, Chris, Patricia, Cameron, Anand, Hannah, Jordyn, Maura, Autumn, Hamid, Amir, Lillia, Lihong, Yaqi, and Wanyang. They are a wonderful group of scientists and engineers, I am so lucky to have had a chance to work with them. Additionally, I have been lucky enough to work with some incredible undergraduates, I hope I was a good mentor toward them. I would like to thank my friends and family, they have all been so wonderful to me throughout my PhD. They were incredibly patient when I had to cancel plans for work, they were always there when I needed to talk, and often gave me a different perspective to life. In the end, they helped me grow, become more compassionate, and be a better human. They mean the world to me and I love them dearly. I would like to single out my sister, Kotti. She is an amazing, wonderful, kind, and sweet person. She encourages me, lifts me up, and prays for me – probably daily. I have always appreciated her insight, gentle advice, and out-of-control laughter. Finally, I would like to thank my home planet, Earth, it gives us everything and I hope one day soon we will return the favor.

TABLE OF CONTENTS

LIST OF FIGURES

LIST OF TABLES

CHAPTER 1

INTRODUCTION

1.1 Rapid Prototyping for Personalized Medicine

Rapid prototyping was coined in the mid-80s as a group of technologies to quickly form 3D objects from layered material[1]. In the last ten years, this technology has received a lot of widespread attention due to the availability of low-cost, desk-top systems, such as the Fab@Home multi-material 3D printer pioneered by Cornell students. This technique transforms computer-aided-designs (CADs) into physical models by slicing the design into multiple layers and then depositing the desired material layer-by-layer, until the arbitrary geometry is realized. Depending on the chosen method of fabrication, a wide variety of materials are available, from soft, tissue-like, hydrogels to rigid metals.

Additive manufacturing has been used extensively in medicine for the fabrication of 3D models of organ systems for education, surgical planning, and diagnostic assistance (See Appendix A)[2-4]. These models are particularly useful in patients whose anatomy is abnormal due to birth defects, or a diseases state[3]. Additionally, if a surgeon needs to practice a procedure, or test out an off-the-shelf device on a patient's anatomy then using a printed model of the patient is an ideal option. There have been major advancements in the use of virtual reality for surgical planning, but these systems can be expensive and we are naturally more adept at understanding a physical, tactile model.

3D bioprinting is another application of additive manufacturing in medicine. The goal of bioprinting is to be able fabricate tissue constructs, vessels, or even whole organs for transplants, drug development, and basic research[5]. This field is heavily researched and will revolutionize personalized medicine.

The obvious application of 3D printing in medicine is for the fabrication of synthetic, patient-specific prosthesis and biomedical devices. The work in this area has been limited by material selection, cost, and the FDA approval process.

1.3 Left atrial appendage

The left atrial appendage (LAA) is a remnant of the embryonic left atrium that develops during the third week of gestation[6]. It is a small, irregularly shaped, and blind ended structure that protrudes from the left atrium of your heart (Fig. 1.1). Until recently, this appendage was considered to be of little importance to cardiac anatomy. It is now well accepted that more than 90% of thrombi in patients with non-rheumatic atrial fibrillation (AF) originate in the LAA[7]. The overall morphology and internal architecture are targeted as the main reasons for the increased incidence of clot formation in the LAA[6]. Removal or occlusion of the LAA for the prevention of a thromboembolic event is recommended for high risk patients with a contra-indication to anticoagulants[7].

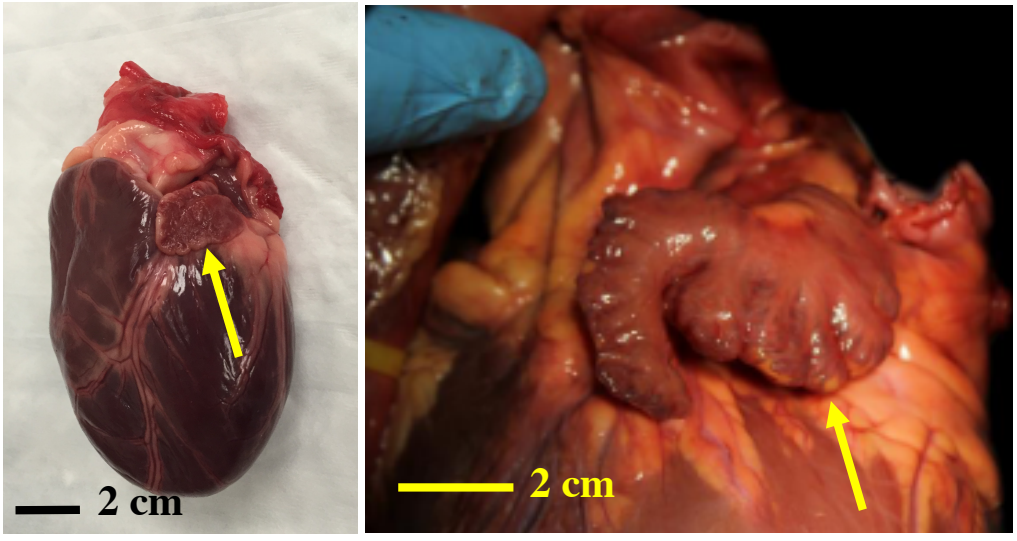

Figure 1.1| Explanted canine heart with left atrial appendage marked by arrow. This image shows the size and position of the LAA in relation to the whole heart. The image on the right also has the LAA marked by a yellow arrow. This is an adult, human specimen, the morphology of the LAA is highly irregular in morphology. (This image

is from a conference talk by Dr. Reisman from the University of Washington, TCT 2015.)

1.3.1 Anatomy

The LAA can have a variable number of lobes – which are used to classify the morphology type (Figure 1.2, top)[8]. Four major categories have been established by Di Biases et al: Cactus, Chicken Wing, Windsock, and Cauliflower. The cactus has one main central lobe with smaller lobes protruding from it. The Chicken Wing LAA has a central lobe that looks like it was bent half way down. The Windsock (Fig. 1.1, right) has a central lobe that curves back on itself in two places. The Cauliflower LAA is the most irregular of all – it has a variable number of lobes and lacks a central lobe. Additionally the overall size of the LAA is highly variable, its length can range from 16 – 51 mm and its volume ranges from 0.7 – 19.2 mL[9]. The ostium is the opening between the left atrium and the LAA [10]. From the endocardial surface the ostium is well defined by ridge-like folds of the atrial wall (Fig 1.2, bottom left). Su et al. used 31 heart specimens to measure the long and short diameters of the ostium; they show that the ostium is typically elliptical in shape and the long diameter ranges in size from 10-24.1 mm long while the short diameter ranges from 5.2-19.5 mm wide[10]. Pectinate muscles can be found within the body of the LAA; large (at least 0.5mm in diameter) muscles are visible on computed tomography (CT) scans. Pectinate are large muscle bars that run from the top of the LAA to the bottom. The endocardial wall between the pectinate muscles can be extremely thin and delicate (Figure 1.2, bottom right). The LAA is surrounded by several key anatomical landmarks. On the endocardial surface, the LAA is in very close proximity (~10 mm) to the superior and inferior left pulmonary veins and the mitral valve (Fig. 1.2, bottom left). The circumflex artery runs just below the LAA along the epicardial surface (Fig. 1.2, bottom right)[10].

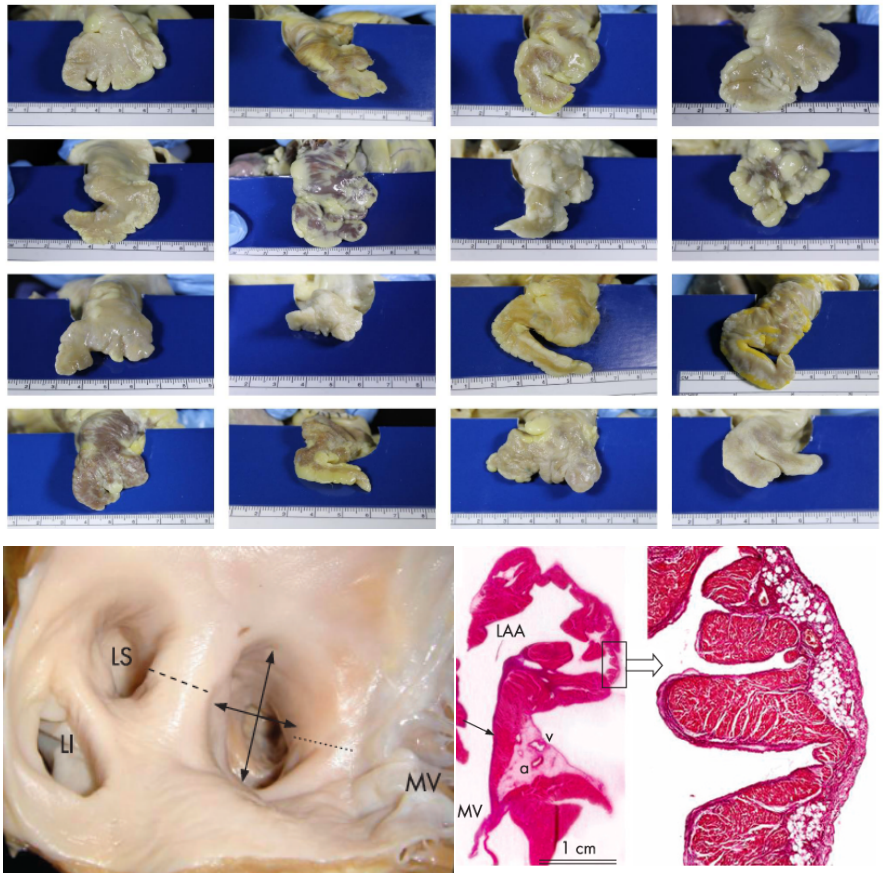

Figure 1.2| Left atrial appendage anatomy. The LAA morphology is categorized based on the number and placement of its lobes. (Top image was adapted from a conference talk by Dr. Reisman from the University of Washington, TCT 2015). Image on the left is an internal view of the ostium of the LAA with the long and short diameters marked by black arrows. The mitral valve (MV) can be seen to the right of the opening. Left superior and inferior (LS & LI) pulmonary veins are seen to the left of the ostium. The image on the right is a histology slice of the LAA. It shows the position of the circumflex artery (a) and vein (v). It also demonstrates how thin some regions of the LAA tissue wall can be between the pectinate muscles (enlarged on bottom right). (This image was adapted from Su et al, *Interventional cardiology*, 2008.)

1.3.2 Atrial Fibrillation, Stroke, and the LAA

Atrial fibrillation (AF) is a very common cardiac arrhythmia effecting 2-4% of our elderly population[11]. Patients with AF have an increased risk of stroke that is independent of other risk factors, such as age and coronary artery disease[12]. This was particularly evident in a drug trial where participants with multiple cardiac diseases, (i.e. atrial fibrillation, hypertension, coronary heart disease) were given anticoagulants and an 80% reduction in stroke was observed. Since these drugs are only beneficial in the prevention of blood clot formation, and do not help with diseases such as hypertension and coronary heart diseases, it seems likely that AF was the main cause of stroke in the majority of these participants[12]. More recent studies have shown that approximately 20-25% of all strokes each year are contributed to AF [7]. A study performed by Stoddard et al. has shown that patients with acute (<3 days) AF form clots in the left atrium and these clots are typically located inside of the LAA[11]. In a study performed by Blackshear et al., 23 separate studies were reviewed, they concluded that 91% left atrial thrombi originated from the LAA in patients with non-rheumatic AF[13].

1.3.3 Treatment Options

Pharmaceutical

Currently the gold standard of treatment for the prevention of stroke in patients with AF is oral anticoagulation therapy (i.e. Warfarin)[14], however, there are several challenges associated with the long-term use of Warfarin and other oral anticoagulants. Patients taking these drugs have to be vigilant with their food, alcohol, and drug intake as these could have negative interactions with the anticoagulants [7]. Additionally, Warfarin is associated with a narrow therapeutic window, therefore frequent blood draws for dose adjustments and monitoring needs to be performed[7]. If the dosage is too high, then the patient is at risk for internal hemorrhaging, however, if the dosage is too low then there is a risk of a thromboembolic event occurring. Currently, newer

anticoagulants are being developed that will hopefully avoid some of these challenges, however there is still a population of patients with AF who have contra-indications to the use of blood thinners, these patients need an alternative therapy[14,15].

Surgical

Surgical closure or removal of the LAA is guideline recommended for patients who are having other open heart procedures such as mitral valve operations or Maze procedures[16]. There are currently two surgical approaches to achieve LAA obliteration, (1) *amputation* of the LAA at the base and stapling/suturing the epicardium closed, (2) *exclusion* of the LAA via suturing, stapling, or clipping (using a AtriClip™) at the base. Although these surgical techniques are relatively straightforward, they often result in incomplete closure[17,18], or remnant LAA present[19].

Katz et al. looked at 50 patients who underwent LAA obliteration via suture ligation and found that 36% had incomplete closure and therefore residual blood flow into the LAA[17]. This same value was reported again in a more recent study by Aryana et al., additionally, they showed there is a 24% increased risk of stroke in patients with incomplete LAA closure[18]. Closure success was also explored by Kanderian et al., they found that patients undergoing LAA amputation, 27% of patients had a remnant LAA present (cul de sac)[19]. Additionally, purse string sutures, used to ligate the LAA can leave a puckered suture line on the endocardial surface, these ridges are possible areas of thrombus formation[10].

The AtriClip is a device made of rigid, titanium tubes held together by nitinol springs, the tubes have been covered with polyester fabric (Fig. S2.12). These tubes are opened and the LAA is slid in between them, the tubes are then clamped down at the base of the LAA. While initial studies have shown promising results using this device, there are still questions concerning damage to the LAA and surrounding structures, as this is a bulky, rigid device clamped to the delicate, thin tissue of the LAA in the epicardial space. Additionally, there may still be an issue if the clamp cannot get close

enough to the ostium, or if the endocardial surface is folded in such a way that would promote thrombus formation.

Percutaneous interventions

Currently there are several devices available that can be implanted percutaneously (Fig. 1.3). This means that the device can be loaded into a small diameter catheter which is guided up through your femoral vein into your heart and delivered to the LAA by pushing it out of the end of the catheter. Some of these devices are available for clinical use in Europe and clinical trials in the United States[9]. There are only two devices FDA approved for clinical use in the USA, the Watchman and the LARIAT suture device. The majority of these devices are composed of a self-expanding nitinol frame with a polymeric covering, they are all circular in shape but claim conformability due to the architecture of the frame[9]. These devices come in a limited number of sizes.

The LARIAT suture delivery system is unique to these other devices because it is placed on the epicardial surface. It is essentially the same as suture ligating the LAA, which was discussed in the previous surgical section. This device works by placing a catheter on the internal, distal end of the LAA and then placing a second catheter on the external surface, both catheters have a small magnet at their tips and can therefore locate and stick to each other. The suturing loop is then passed over the external catheter and the LAA, with the goal of placing it at the base of the LAA where it will be cinched down around the ostium. This is a very tricky method and has resulted in laceration of the LAA and emergency open heart surgery. The FDA has recently administered a warning concerning the clinical use of the LARIAT.

The Prolipsis device is also unique because it does not use a nitinol frame. This device is made of a latex balloon with a polyurethane covering. The balloon is filled with contrast solution until it blocks the ostium of the LAA, next a type of surgical glue is delivered to the polyurethane patch to glue it to the internal wall of the appendage. This spherical device is currently undergoing animal trials[20].

As mentioned above, the ostium of the LAA is typically elliptical in shape, while the majority of the devices discussed here are round in geometry. This mismatch in shape can cause crevices to form on either side of the device which leads to peri-device flow into the LAA[10]. To overcome this issue, interventionalists typically oversize the device they are implanting, with the goal of stretching the ostium into the shape of the device. This practice could lead to several problems: (1) hooks used to anchor the device could pierce deeply into the thin LAA tissue, possibly all the way through to the pericardial space, (2) anatomical structures that are in close proximity of the LAA can be damaged/blocked by the oversized device, (3) devices that are severely oversized can embolize from the LAA into the atrial space[10].

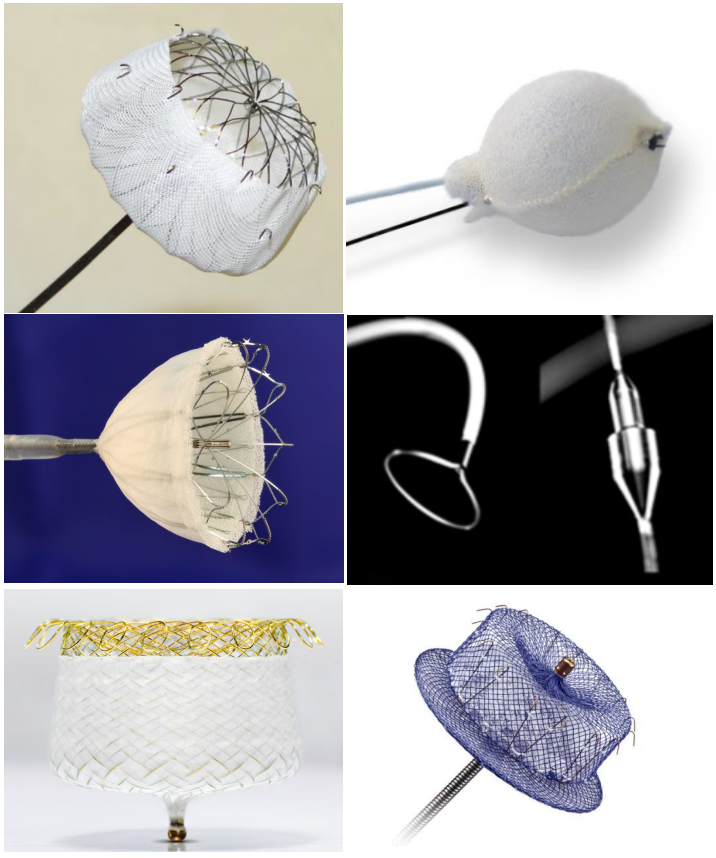

Figure 1.3| Percutaneous occluders. Clockwise from top left: Watchman Flex, device produced by Boston Scientific, Nitinol frame with polyethylene terephthalate (PET) covering. Prolipsis, soft occluder by Sideris, composed of polyurethane patch around a latex balloon, spherical in shape. Lariat Suture Delivery by Sentre Heart. Amulet device

by St. Jude Medical, nitinol frame with Dacron polyester. Occlutech, nitinol frame with nanospun polyurethane covering. Coherex WaveCrest, nitinol frame with polytetrafluoroethylene (ePTFE) covering. (This image was adapted from multiples talks at TCT 2015; Sievert, H. et al., CardioVascular Center; Sideris, E.B.; Saw, J., University of British Columbia; Malik, I. Hammersmith Hospital; Whisenant, B., Intermountain Heart Institute.)

1.4 Dissertation Scope and Organization

The main body of my dissertation is broken up into three chapters. The first and second chapters describe the design, fabrication, and characterization of two generations of patient-specific, soft LAA occluders. The third chapter describes an approach for 3D printing soft, capacitive sensors onto the surface of a prefabricated object.

The first generation LAA occluder, described in Chapter 2, is the *first* demonstration of a soft, cardiovascular implant based on 3D printing. I present a new class of cardiac occluder that can truly fully occlude any shape of the LAA by using two design schemes: (i) fabricating a soft material occluder that can inflate to conform the anatomy of the LAA, and (ii) using a patient-specific design derived from CT images. The occluder is an elastomeric device comprised of the following components: (i) a composite silicone material that dictates the mechanics of the balloon, (ii) a polycarbonate-urethane coating to provide hemocompatibility, (iii) a monolithically integrated valve to hold pressure upon inflation, (iv) a biocompatible filling liquid that cures to a solid to reduce long-term risk of leakage, (v) a monolithic plug that can be sutured to the LAA to prevent embolization of the occluder, (vi) a patient-specific design to ensure proper occlusion of the LAA without impinging on the surrounding tissue. I developed workflows for the design, fabrication, and deployment of this soft, patient-specific LAA occluder to prevent stroke in patients with atrial fibrillation. This device demonstrates a novel approach for fabrication of personalized cardiovascular implants, which are durable and hemocompatible. Furthermore, the approach or similar incarnations can be applied more broadly to treat a variety of cardiovascular diseases,

where the size and shape of conventional implants and/or complex patient anatomy exclude patients from treatment, or result in decreased device efficacy.

While the molding LAA occluder offers a robust workflow, scalable process, and large material variety it is a multi-step, labor intensive fabrication route with a minimum three day turn around and a minimum wall thickness of ~ 500 um. In order to decrease the time it takes to get these devices to patients in need, as well as decrease the wall thickness of the device, I chose to directly 3D print the second generation of occluders using Continuous Liquid Interface Production. This paper describes the design process and workflow for fabricating very robust 3D printing occluders in under 12 hours. These occluders also show improved mechanics and reliability over the first generation.

The described occluders do not currently have any sensing capabilities. This added functionality would improve the positioning and deployment of this occluder. In the Chapter 4 I describe my work on 3D printing a sensing skin directly to the surface of a pre-fabricated (molded silicone) object. To enable this printing method I developed two viscoelastic inks – one that is a conductive acrylamide hydrogel, another that is an insulating silicone. By patterning these inks into alternating layers and then photopolymerizing them, I fabricated highly stretchable capacitive sensors.

REFERENCES

[1] I. Campbell, D. Bourell, I. Gibson, *Rapid Prototyping Journal* **2012**, *18*, 255.

[2] L. Lao, S. S. Robinson, B. Peele, H. Zhao, B. C. Mac Murray, J. K. Min, B. Mosadegh, S. Dunham, R. F. Shepherd, *Adv. Eng. Mater.* **2016**, *19*, 1600591.

[3] M. Vukicevic, B. Mosadegh, J. K. Min MD, S. H. Little MD, *JACC: Cadiovascular Imaging* **2017**, *10*, 171.

[4] A. A. Giannopoulos MD, L. Chepelev, A. Sheikh, A. Wang, W. Dang, E. Akyuz, C. Hong, N. Wake, T. Pietila, P. B. Dydynski, D. Mitsouras, F. J. Rybicki, *3D Printing in Medicine* **2015**, *1*, 1.

[5] S. V. Murphy, A. Atala, *Nature Biotechnology* **2014**, *32*, 773.

[6] N. M. Al-Saady, O. A. Obel, A. J. Camm, *Heart* **1999**, *82*, 547.

[7] B. Kong, Y. Liu, H. Huang, H. Jiang, C. Huang, *J Thorac Dis* **2015**, *7*, 199.

[8] L. Di Biase MD, P. Santangeli MD, M. Anselmino MD, P. Mohanty, I. Salvetti MD, S. Gili MD, R. Horton MD, J. E. Sanchez MD, R. Bai MD, S. Mohanty MD, A. Pump MD, M. Cereceda Brantes MD, G. J. Gallinghouse MD, J. D. Burkhardt MD, F. Cesarani MD, M. Scaglione MD, A. Natale MD, F. Gaita MD, *JACC* **2012**, *60*, 531.

[9] N. C. Wunderlich, R. Beigel, M. J. Swaans, S. Y. Ho, R. J. Siegel, *JACC: Cardiovascular Imaging* **2015**, *8*, 472.

[10] P. Su, K. P. McCarthy, S. Y. Ho, *Heart* **2008**, *94*, 1166.

[11] M. F. Stoddard MD, P. R. Dawkins MD, C. R. Prince MD, N. M. Ammash MD, *JACC* **1995**, *25*, 452.

[12] P. A. Wolf MD, R. D. Abbott, W. B. Kannel MD, *Stroke* **1991**, *22*, 983.

[13] J. L. Blackshear MD, J. A. Odell FRCS(Ed), *Ann Thorac Surg* **1996**, *61*, 755.

[14] C.-M. Yu, A. A. Khattab, S. C. Bertog, A. P. W. Lee, J. S. W. Kwong, H. Sievert, B. Meier, *Nat Rev Cardiol* **2013**, *10*, 707.

[15] S. A. Luis, D. Roper, A. Incani, K. Poon, H. Haqqani, D. L. Walters, *Cardiology Research and Practice* **2012**, *2012*, 1.

[16] V. Badhwar MD, J. S. Rankin MD, R. J. Damiano MD, A. M. Gillinov MD, F.

G. Bakaeen MD, J. R. Edgerton MD, J. M. Philpott MD, P. M. McCarthy MD, S. F. Bolling MD, H. G. Roberts MD, V. H. Thourani MD, R. M. Suri MD, R. J. S. MD, S. Firestone MS, N. Ad MD, *Ann Thorac Surg* **2017**, *103*, 329.

[17] E. S. Katz, T. Tsiamtsiouris, R. M. Applebaum, A. Schwartzbard, P. A. Tunick, I. Kronzon, *JACC* **2000**, *36*, 468.

[18] A. Aryana, S. K. Singh, S. M. Singh, P. G. O'Neill, M. R. Bowers, S. L. Allen, S. L. Lewandowski, E. C. Vierra, A. d'Avila, *Heart Rhythm* **2015**, *12*, 1431.

[19] A. S. Kanderian, A. M. Gillinov, G. B. Pettersson, E. Blackstone, A. L. Klein, *JACC* **2008**, *52*, 924.

[20] S. Toumanides MD, E. B. Sideris MD, T. Agricola MD, S. Moulopoulos MD, *JACC* **2011**, *58*, 2236.

[21] D. Mozaffarian, E. J. Benjamin, A. S. Go, D. K. Arnett, M. Blaha, M. Cushman, S. de Ferranti, J.-P. Després, H. Fullerton, V. Howard, M. Huffman, S. Judd, B. Kissela, D. Lackland, J. Lichtman, L. Lisabeth, S. Liu, R. Mackey, D. B. Matchar, D. K. McGuire, E. Mohler III, C. Moy, P. Muntner, M. Mussolino, K. Nasir, R. Neumar, G. Nichol, L. Palaniappan, D. Pandey, M. Reeves, C. Rodriguez, P. Sorlie, J. Stein, A. Towfighi, T. Turan, S. Virani, J. Willey, D. Woo, R. Yeh, M. Turner, *Circulation* **2015**.

[22] G. Ailawadi MD, M. W. Gerdisch MD, R. L. Harvey MD, R. L. Hooker MD, R. J. Damiano MD, T. Salamon MD, M. J. Mack MD, *J Thorac Cardiovasc Surg* **2011**, *142*, 1002.

[23] J. Snyder, A. M. Engel, K. C. White, N. Budiansky, J. M. Smith, *SS* **2012**, *03*, 28.

[24] J. D. Moss, *Curr Cardiol Rep* **2014**, *16*, 448.

[25] J. M. Lee, J. Shim, J.-S. Uhm, Y.-J. Kim, H.-J. Lee, H.-N. P. MD, M.-H. Lee, B. Joung, *The American Journal of Cardiology* **2014**, *113*, 963.

[26] J. F. Viles-Gonzalez MD, S. Kar MD, P. Douglas MD, S. Dukkipati MD, T. Feldman MD, R. Horton MD, D. Holmes MD, V. Y. Reddy MD, *JACC* **2012**, *59*, 923.

[27] J. O'Brien, D. Al-hassan, J. Ng, M. Joshi, C. Hague, S. Chakrabarti, J. Leipsic,

Int J Cardiovasc Imaging **2014**, *30*, 819.

[28] A. M. Reed, J. Potter, M. Szycher, *Journal of Biomaterials Applications* **1994**, *8*, 210.

[29] M. C. Bélanger, Y. Marois, R. Roy, Y. Mehri, E. Wagner, Z. Zhang, M. W. King, M. Yang, C. Hahn, R. Guidoin, *Artif Organs* **2000**, *24*, 879.

[30] E. Braunwald MD, E. C. Brockenbrough MD, C. J. Frahm MD, J. Ross MD, *Circulation* **1961**, *24*, 267.

[31] L. Lao, S. S. Robinson, B. Peele, H. Zhao, B. C. Mac Murray, J. K. Min, B. Mosadegh, S. Dunham, R. F. Shepherd, *Adv. Eng. Mater.* **2016**, *19*, 1600591.

[32] A. A. Giannopoulos MD, D. Mitsouras, S.-J. Yoo, P. P. Liu, Y. S. Chatzizisis, F. J. Rybicki, *Nat Rev Cardiol* **2016**, *13*, 701.

[33] S. Anwar MD, G. K. Singh MD, J. Varughese, H. Nguyen MD, J. J. Billadello MD, E. F. Sheybani MD, P. K. Woodard MD, P. Manning MD, P. Eghtesady MD, *JACC: Cardiovascular Imaging* **2016**, 1.

[34] F. Mahmood MD, K. Owais MD, C. Taylor, M. Montealegre-Gallegos MD, W. Manning MD, R. Matyal MD, K. R. Khabbaz MD, *JACC: Cardiovascular Imaging* **2015**, *8*, 226.

[35] D. B. Kolesky, K. A. Homan, **2016**.

[36] B. Mosadegh, G. Xiong, S. Dunham, J. K. Min, *Biomed Mater* **2015**, *10*, 034002.

[37] D. Y. Cheung, B. Duan, J. T. Butcher, *Expert Opin Biol Ther* **2015**, *15*, 1155.

[38] B. Derby, *Science* **2012**, *338*, 921.

[39] S. H. Sündermann, M. Gessat, N. Cesarovic, T. Frauenfelder, P. Biaggi, D. Bettex, V. Falk, S. Jacobs, *Interactive CardioVascular and Thoracic Surgery* **2013**, *16*, 417.

CHAPTER 2

PATIENT-SPECIFIC DESIGN OF SOFT OCCLUDER FOR THE LEFT ATRIAL APPENDAGE

Sanlin S. Robinson, Seyedhamidreza Alaie, Hannah Sidoti, Jordyn Auge, Lohendran Baskaran, Kenneth Avilés-Fernández, Samantha D. Hollenberg, Robert F. Shepherd, James K. Min, Simon N. Dunham, and Bobak Mosadegh, *Nat. Biomed. Eng.*, **(2017)**

2.2 Introduction

Atrial fibrillation (AF) is the most common cardiac arrhythmia, with 0.8 % to 1.9 % of the population affected[21]. Patients with AF are found to have a five-fold increase in the incidence of stroke[12], often attributed to the embolism of cardiac thrombi. Studies have shown that 90% of these thrombi originate in the LAA[13]; a tubular, blind-ended, and hooked structure protruding from the left atrium[6,8]. The LAA allows blood to become stagnant and clot when the atrium does not effectively contract (as is the case in patients with AF)[6,11]; stroke occurs when these clots embolize to the brain. Currently, oral anti-coagulants (i.e. warfarin) are considered the gold standard of treatment for stroke prevention in patients with AF, however, the patients taking warfarin have a five-fold increase in the risk of intracranial hemorrhage[7,14]. Non-pharmacological strategies that locally prevent the development of thrombi in the LAA include surgical excision or exclusion[17,19,22,23], and percutaneous occlusion of the LAA[7,9,14,20]. Recently, several companies have designed devices to occlude the LAA via transcatheter delivery[7,14,20,24]. Recently, the Watchman device from Boston Scientific was given FDA approval (but only for use in patients counter-indicated for oral anti-coagulants), giving much promise for transcatheter delivery of LAA occluders. Eventually, transcatheter embodiments of the device described here could have a huge impact,

however, a significant proportion of patients with AF still undergo open-heart surgery for other treatments, thus maintaining a need for LAA occluders that can be delivered during a surgical procedure. In fact, surgical excision or exclusion (stapling, suturing, or clipping) of the LAA is guideline-recommended concomitantly in AF patients undergoing mitral valve, coronary artery bypass, or aortic valve replacement surgery[16,18]. Despite evidence showing that surgical management of the LAA is effective, many surgeons do not perform this procedure due to significant risks associated with incomplete closure of the LAA (~60% of cases)[17,19]. Incomplete closure of the LAA has been reported to increase the risk of stroke from 2% to 24%[18]. Patients with incomplete closure often need to remain on anticoagulants, thus negating the goal of the procedure[18]. Also, suturing techniques can leave a puckered suture line on the endocardial surface of the atrium that could promote thrombus formation, while stapling methods can tear the paper-thin walls of the LAA[10].

The poor outcomes of surgical techniques for excluding the LAA may be rooted in the fact that the size, morphology, and internal anatomy of the LAA varies dramatically among patients[8,9,25,26]. This variability may make it difficult for standard devices or techniques to seal the appendage[26]. The body of the LAA ranges between 0.77 and 19.27 cm^3 in volume and is trabeculated with small pectinate muscles[6,10,15]. Furthermore, even though cardiac radiologists categorize the shape of the LAA into general types – such as Chicken Wing, Cactus, and Cauliflower – the morphology and size is still highly variable within each of these categories [8,9,25,26]. The opening in the atrium that leads to the LAA is called the ostium. This eccentric, elliptical landmark varies dramatically in size with a short diameter ranging from 5-27 mm, and a long diameter of 10-40 mm[6,10]. Full closure of the LAA using current methods may become more challenging as the eccentricity of the ostium increases[26,27]. Without fully sealing the LAA, clot formation is promoted within the appendage (both on and off the device), ultimately increasing the chance of an embolic event[25].

To address the issues of incomplete exclusion of the LAA, we have developed a patient-specific, soft LAA occluder. This occluder is an inflatable balloon with a geometry matching the anatomical morphology of the patient's own LAA, as ascertained by non-invasive CT imaging (Fig. 2.1a). While a spherical balloon, composed of soft materials can conform to most shapes, patient-specificity is needed to minimize strain on (*i*) the elastomeric material of the balloon when inflated to fill complex, multi-lobular structures, and (*ii*) the LAA tissue and neighboring structures. Over-inflation of a spherical balloon to obtain full occlusion can impinge upon nearby anatomy[10] or result in unfavorable hemodynamic interfaces at the ostium of the LAA. From the CT images, we used segmentation software to produce 3D renderings of the blood volume within a patient's LAA. This blood volume is then used as a template to make a thin-walled elastomeric occluder. Our lab has developed a composite elastomeric material comprising three commercially available polymers, two that are easily molded using 3D printed parts (defining the primary mechanics of the occluder), and a third that is known to be thromboresistant and biocompatible[28,29]. We chose compliant materials (extensibilities > 200%) yielding occluders that conform to the LAA morphology upon inflation. The occluder is monolithically integrated with a soft valve that enables the surgeon to fill the occluder without leakage once disengaged from the deployment apparatus (Fig. 2.1b, right). Following implantation, the occluder is filled with a biocompatible epoxy to stabilize it within the LAA. The full process of imaging a patient's LAA, fabricating a patient-specific occluder, and surgically implanting the occluder into that same patient, has been performed on a single large animal model (Fig. 2.7). Although further experiments are needed to assess the long-term performance of this novel device, this work serves as a proof-of-concept that 3D printing can be used to fabricate patient-specific and inflatable endovascular devices.

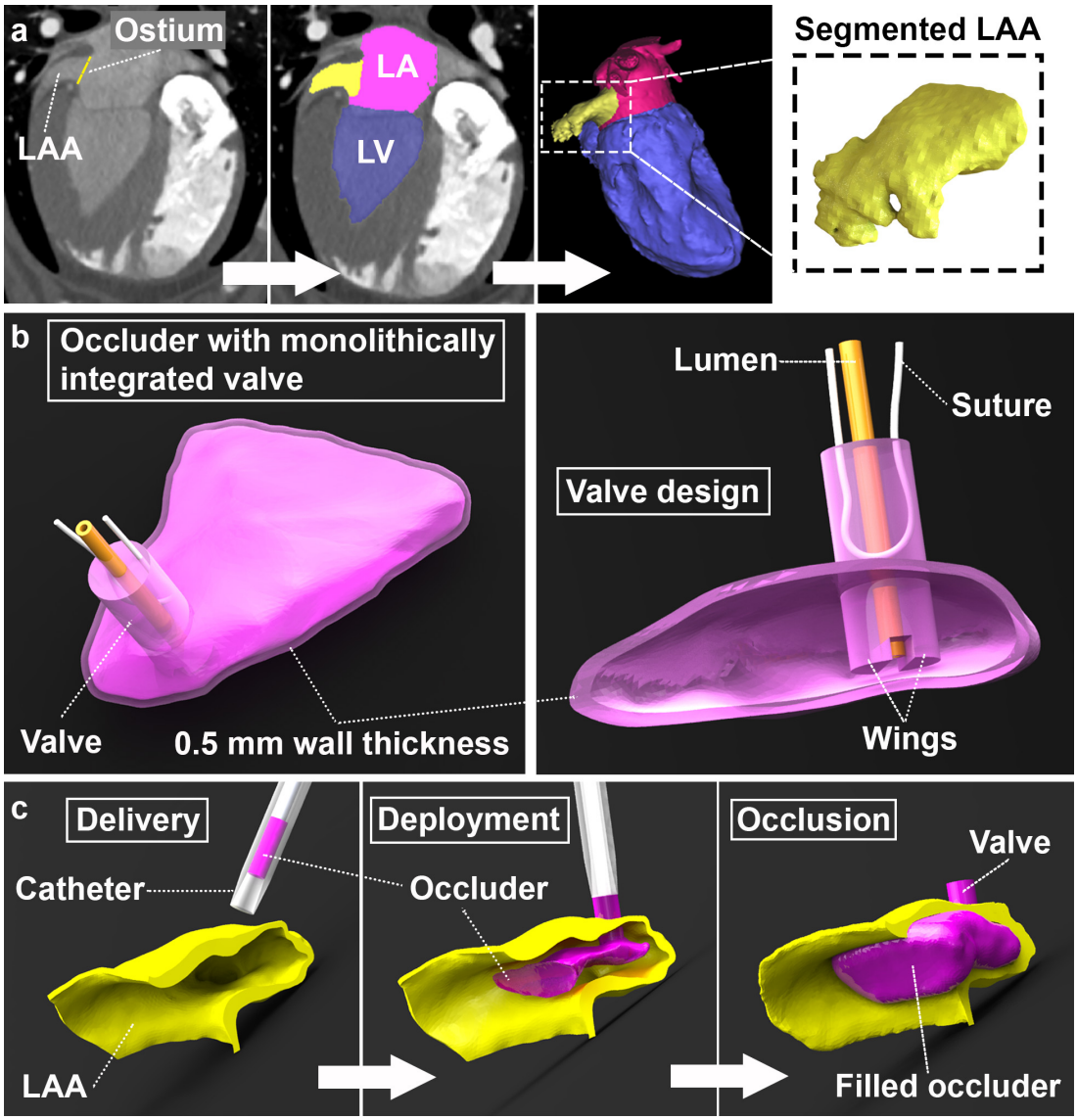

Figure 2.1| Patient-specific occluder design and deployment. (**a**) CT segmentation and image post-processing to isolate LAA (canine model). Left most image is cropped CT scan before segmentation to illustrate regions of interest. The next three images are after segmentation has been performed in Mimics®. In the segmented images the LAA is filled in with yellow, the left atrium (LA) is filled in with pink, and the left ventricle (LV) is filled in with blue. (**b**) We used the segmented LAA to design a patient-specific, soft occluder with a monolithically integrated valve. This occluder is hollow with a wall thickness of ~0.5 mm. We intended the valve for filling, anchoring, and retrieval of the occluder during the deployment process. A lumen is pierced through the valve to inject a filling solution. A suture made of nylon is threaded through the valve to retrieve this

occluder. (**c**) The occluder is delivered to the distal tip of the LAA using a catheter. The evacuated occluder is pushed out of the catheter during deployment. Finally, the occluder is filled through the lumen, until it fully occludes the LAA, and the catheter system is removed. The valve keeps the filling solution inside of the occluder to maintain the final volume. (**b** and **c** are SolidWorks® renderings of canine occluder deployment.)

2.3 Design Considerations for a surgically deployed soft LAA occluder

We chose to use a patient-specific design to enable stable anchoring and full occlusion of the LAA. Current occluder devices localize to the ostium of the LAA, and have standard circular geometries, resulting in potential leakage around the device in LAAs with an eccentric ostium[10,26]. Often these devices are oversized by 10-20% to achieve full occlusion; however, this puts unnecessary stress on the LAA tissue and surrounding anatomy[10,26]. By having a patient-specific occluder that inflates into the distal regions of the LAA, the anchoring surface area is maximized, thus minimizing the local stress required to achieve stable anchoring of the device in the LAA. Furthermore, filling the LAA volume prevents potential contractile forces from the LAA to induce hydraulic flow on the occluder, potentially causing its embolization. Also, the use of soft, elastomeric materials mitigates the risk of perforating the atrial wall and damage to other neighboring anatomical structures. The compliance of these elastomers also enables the occluder to conform to the anatomy of the LAA upon inflation, again, maximizing anchoring surface area. Since the elastomeric materials have relatively high levels of strain to failure (> 200%, Fig. S2.6), we undersized the occluder, facilitating easier insertion into the LAA. We also used smoothing operations, during the segmentation procedure, to simplify the geometry of the occluder, so its alignment to the morphology of the LAA does not need to be exact for proper occlusion. We designed a three-step fabrication process that leverages the advantages of 3D printing (i.e., simple fabrication of arbitrary geometries) and commercially available elastomers (i.e., with robust mechanics and biocompatibility). In the *first* step, we used a high-resolution 3D printer

to build a patient-specific template. In the *second* step, we used conventional molding techniques to fabricate a thin-walled occluder of a custom silicone blend of commercially available materials. In the *third* and final step, we dip-coated the molded silicone occluder in a polycarbonate urethane, which Bélanger et al. has shown to be safe for blood-contacting applications, such as heart valves and ventricle assist devices[29]. This three-step fabrication strategy allowed us to decouple the mechanics of the occluder from its hemocompatibility since our ability to fabricate robust occluders directly from the polycarbonate urethane was limited. We added a multifunctional valve to the occluder to enable inflation, delivery, recovery, and additional anchoring. We chose to use a biocompatible epoxy for the *in vivo* study for three reasons: (*i*) while it was a liquid its viscosity is low enough to flow through a 1 mm diameter lumen to inflate the occluder, (*ii*) its pot life of several hours was more than enough time to inflate/deflate the occluder several times throughout a procedure until the proper orientation was achieved, (*iii*) once hardened there is less risk of long-term damage of the occluder due to contractions of the LAA.

2.4 CT Image Guided Patient-Specific Design

To address the limitations of current LAA closure devices, we developed a patient-specific design based on non-invasive CT imaging. Radiologists routinely perform cardiac CT imaging in preparation for LAA closure procedures; thus, this approach does not add unnecessary clinical imaging. Using image segmentation software (itk-SNAP© 3.4; University of Pennsylvania, and Materialise Mimics® 18.0; Materialise), we isolated 3D surface profiles of the LAA blood volume from the surrounding cardiothoracic anatomy through a combination of automatic and manual segmentation methods (Fig. 2.1a). We then used computer aided design (CAD; Geomagic Wrap® 2015; 3D Systems, and SolidWorks® 2016; Dassault Systèmes) to modify this 3D segmented LAA blood volume and design the occluder device (Fig. 2.1b, S2.1). We performed several post-processing procedures in Geomagic Wrap® to generate a 3D printable file: (*i*) removed non-moldable features of the LAA (i.e. pectinate muscles),

(*ii*) reduced the size of the LAA by offsetting its surface profile inward by 1 mm (offsetting, unlike scaling, maintains the shape and proportion of the LAA morphology), (*iii*) smoothed the surface features of the LAA to meet the resolution of the 3D printer, (*iv*) shelled the surface profile to obtain the desired LAA occluder wall thickness of 0.5 mm (which we determined experimentally to be the thinnest we could produce robustly using our current molding techniques), and (*v*) reduced the number of elements in the CAD in order to process the file in SolidWorks® (Fig. S2.1). Once we generated a shelled 3D rendering of the occluder, we assembled it with a custom-drawn multifunctional valve in SolidWorks® to enable coupling with a catheter (Fig. 2.1b). Next, we designed molds in SolidWorks® using this assembly as a template (Fig. 2.2a, S2.1). By producing occluders with geometries that match the morphology of the LAA, we may reduce the risk of leakage and dislodgement thereby potentially eliminating the exclusion of patients due to device incompatibility.

2.5 Fabrication of Elastomeric Occluder

We printed the above mold designs on a high-resolution 3D printer (Objet260 Connex™, Stratasys) using both hard (Veroclear, Stratasys) and soft (Tango+, Stratasys) materials (Fig. 2.2b, S2.2). We designed the molds to facilitate a two-step fabrication of the silicone base of the occluder: first we formed the two halves of the occluder, and second, we bonded those halves together (Fig. 2.2b, S2.3). We designed the molds for the top-half of the occluder to include the integration of the multifunctional valve. We formed the two halves of the occluder by aligning the rigid (convex) molds, to their soft (concave) mates. We then filled the molds with a homogenous silicone blend of 69wt% Dragon Skin®20 (DS20; Smooth-On, Inc.), 10.3wt% Silicone Thinner® (Smooth-On, Inc.), and 20.7wt% Sylgard®184 (Dow Corning; Fig. 2.2b). We added two drops of Smooth-On Ignite® Fluorescent Pink Color Pigment (Smooth-On, Inc.) to the translucent pre-polymer solution for better visualization throughout the molding process. We placed the molds containing the silicone blend in the oven at 100˚C for 35 minutes. Next, we carefully removed the

partially cured silicone part from the surface of the rigid, inner-wall molds and positioned them in the soft, outer-wall molds (Fig. S2.3). We designed these two soft, outer-wall molds such that the alignment structures on them fit together snugly. We bonded the two halves of the occluder together by carefully lining the edges of the silicone wall with DS20 pre-polymer, and then returning the molds to the oven at 100˚C for one hour. We used pure DS20 instead of the silicone blend for the seams because the pure DS20 had a higher viscosity and tended to stay in position after placement on the seam. We removed the fully formed silicone occluders from the molds and baked them at 100˚C overnight to ensure they were fully cured (Fig. 2.2c). We analyzed the uniformity and total thickness of the occluders by taking multiple cross-sections and imaging them on an optical microscope (Zeiss Stereoscope, Fig. 2.2d). When we excluded the seam region, we found a 25% variation in total wall thickness. We determined that the seams were up to twice as thick as surrounding areas (1 mm max).

We then plasma treated the molded silicone occluder and soaked it in 12% by volume 3-glycidoxypropyltrimethoxysilane (Silane, Sigma-Aldrich) in anhydrous ethanol (Sigma-Aldrich) for one hour. After cleaning and drying the occluder, we dipped it into a solution of ~10wt% polycarbonate urethane (PCU; ChronoFlex AR®, AdvanSource Biomaterials) in dimethylacetamide (Sigma-Aldrich; Fig. 2.2e). We placed the occluder into a 70˚C oven for 2 hours and then dipped it again into the PCU solution. Finally, we put the occluder in a 70˚C oven overnight to fully cure the PCU surface coating. We imaged multiple cross-sectional areas of the occluder using SEM (Nova NanoSEM, FEI) and found the maximum local variation of PCU layer thickness to be less than 18%; the PCU layer was between 11-16 μm (Fig. 2.2f). For most LAA occluders, the surface of the device facing the left atrium will be covered by endothelial cells approximately 45 days after implantation, creating a wall of tissue between the left atrium and the LAA. Therefore, we tested the PCU surface material for compatibility with human endothelial cells and compared it to the silicone blend as well as a polystyrene control (full details in the Supplemental Information, SI). We found that

endothelial cells could attach to both the PCU and silicone blend materials, but that proliferation rates were lower than polystyrene, which we expected (Fig. S2.4).

Using the methods described above, we fabricated patient-specific occluders of three typical morphologies of human LAAs: Cauliflower, Chicken Wing, and Cactus (Fig. 2.3, S2.5)[8,25]. The Cauliflower (CF) LAA morphology is the most complex and irregular among these; it is typically multi-lobular, can have either a circular or elliptical ostium, and lacks a main lobe region[8,25]. The Chicken Wing (CW) LAA has a dominant central lobe with a large bend in its mid-region[8,25]. The Cactus (CC) LAA has a dominant lobe with smaller lobes extending from it in many directions[8,25].

We tested the inflation performance of the occluders using a programmable syringe pump (Fig. S2.6, see SI). We attached the occluders to the syringe pump and a pressure sensor via their integrated valve, we then used LabVIEW™ (2013, National Instruments) to control the syringe pump to increase the volume at a rate of 2.5 mL/min while measuring the pressure until the occluder burst. We found that the occluders can go to at least ten times higher pressures and two times higher volumes than needed for LAA occlusion (Fig. 2.4a-b). Left atrial pressure is on average <2 kPa (<11 mmHg)[30] (Fig. 2.4a, left, red dashed line), while the occluders can achieve at least ~20 kPa of pressure before bursting. The three LAA morphologies we used for this study are not of equal size, therefore to achieve full occlusion, we inflated the occluders to different volumes: CF occlusion volume is ~6 mL, CW occlusion volume is ~5 mL, and the CC occlusion volume is ~3 mL (Fig. 2.4a, right, red dashed lines; Fig. 2.4b, red box). We associate the variation in burst volumes to defects possibly created during the fabrication process (i.e. air bubbles either in the seams or the occluder walls), however, we found that the burst volumes of the PCU coated occluders are at least 127% above the required amounts for full LAA occlusion.

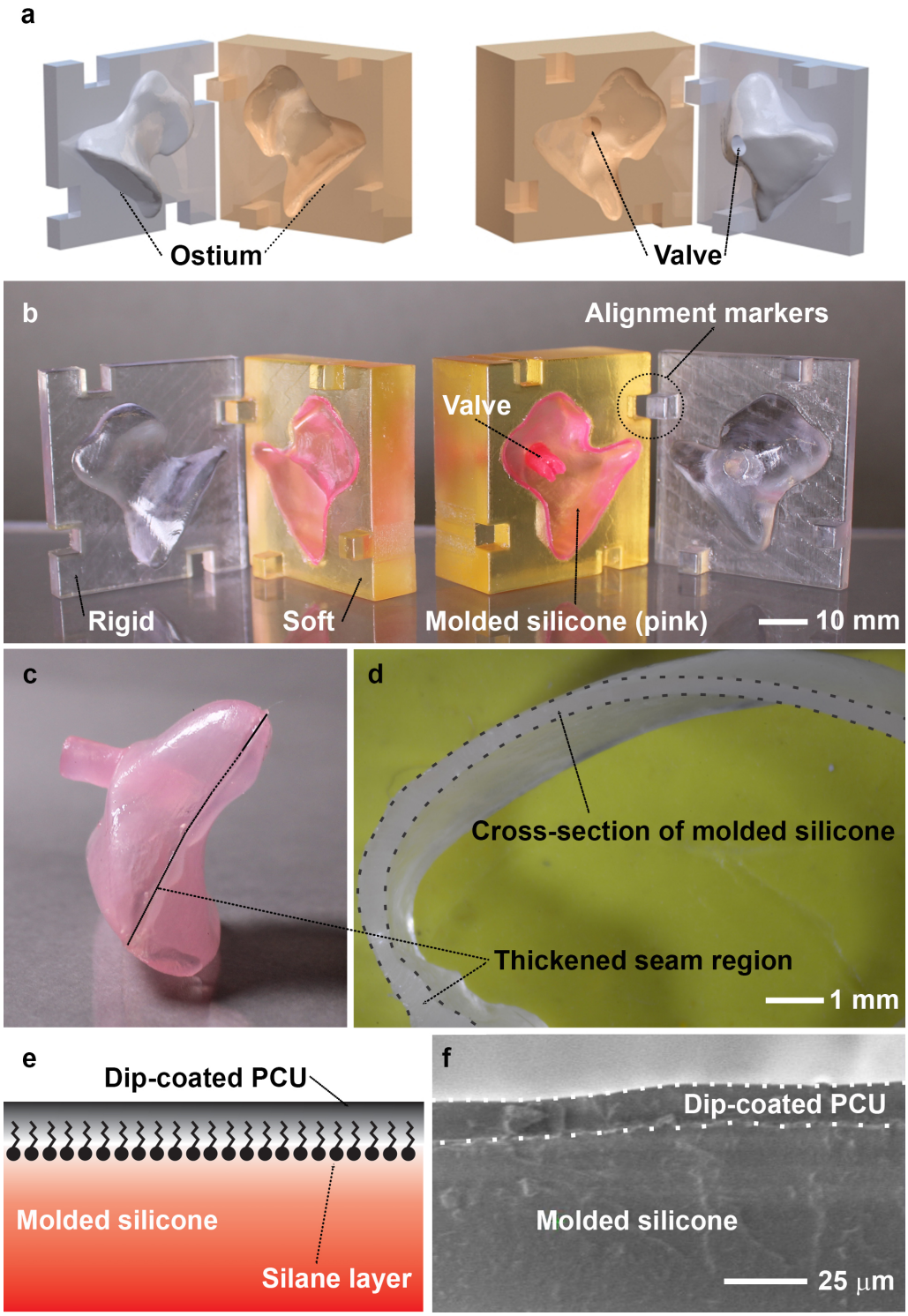

Figure 2.2 | Manufacturing patient-specific occluders. (**a**) SolidWorks® renderings of molds for a human's Cauliflower (CF) occluder. (**b**) Photo of 3D printed molds of CF occluder with the molded silicone shown in pink. We printed convex molds in a

rigid material (VeroClear) and concave molds in a soft material (Tango+) on an Objet260 Connex™. Convex parts form the inner wall of the occluder, while concave parts form the outer wall. We monolithically integrated the valve in the molding process. (**c**) Photo of side view of molded CF occluder with seam traced with black dashed line. (**d**) Optical microscope image of a cross-sectional cut of molded silicone occluder, due to the molding process, the region around seam is slightly thicker. (**e**) Schematic illustrating layers of occluder. Silicone occluders are molded, treated with Silane, and then dip-coated with poly-carbonate urethane (PCU). (**f**) SEM image of the dip-coated PCU layer on the molded silicone layer.

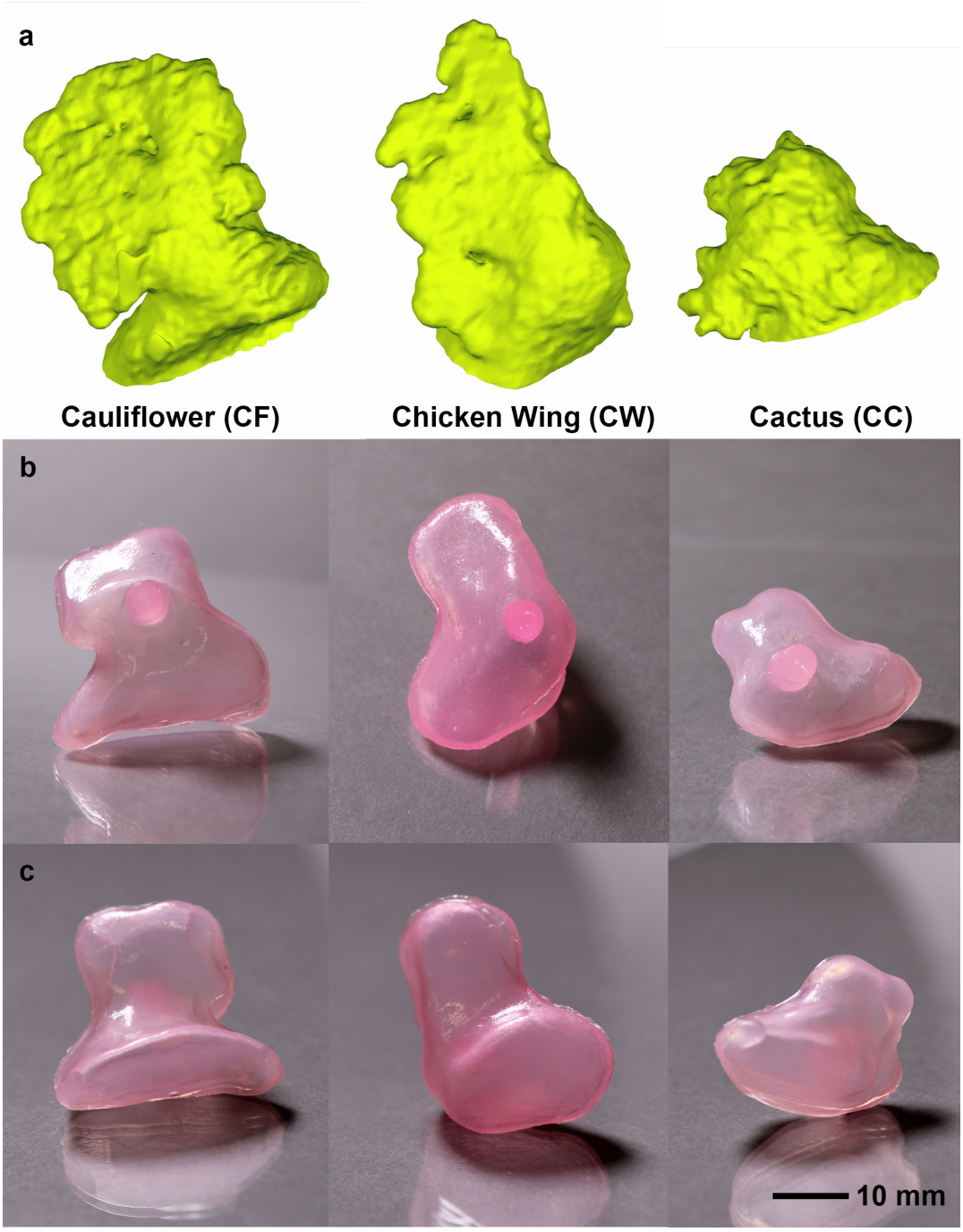

Figure 2.3 | Highly variable LAA morphologies and fabricated patient-specific balloons. (**a**) Topside view of Geomagic Wrap® renderings of segmented blood volume of three LAA morphologies from left to the right: Cauliflower (CF), Chicken Wing (CW), and Cactus (CC). Photos of patient-specific LAA occluders designed and fabricated for these morphologies, (**b**) topside view and (**c**) underside view.

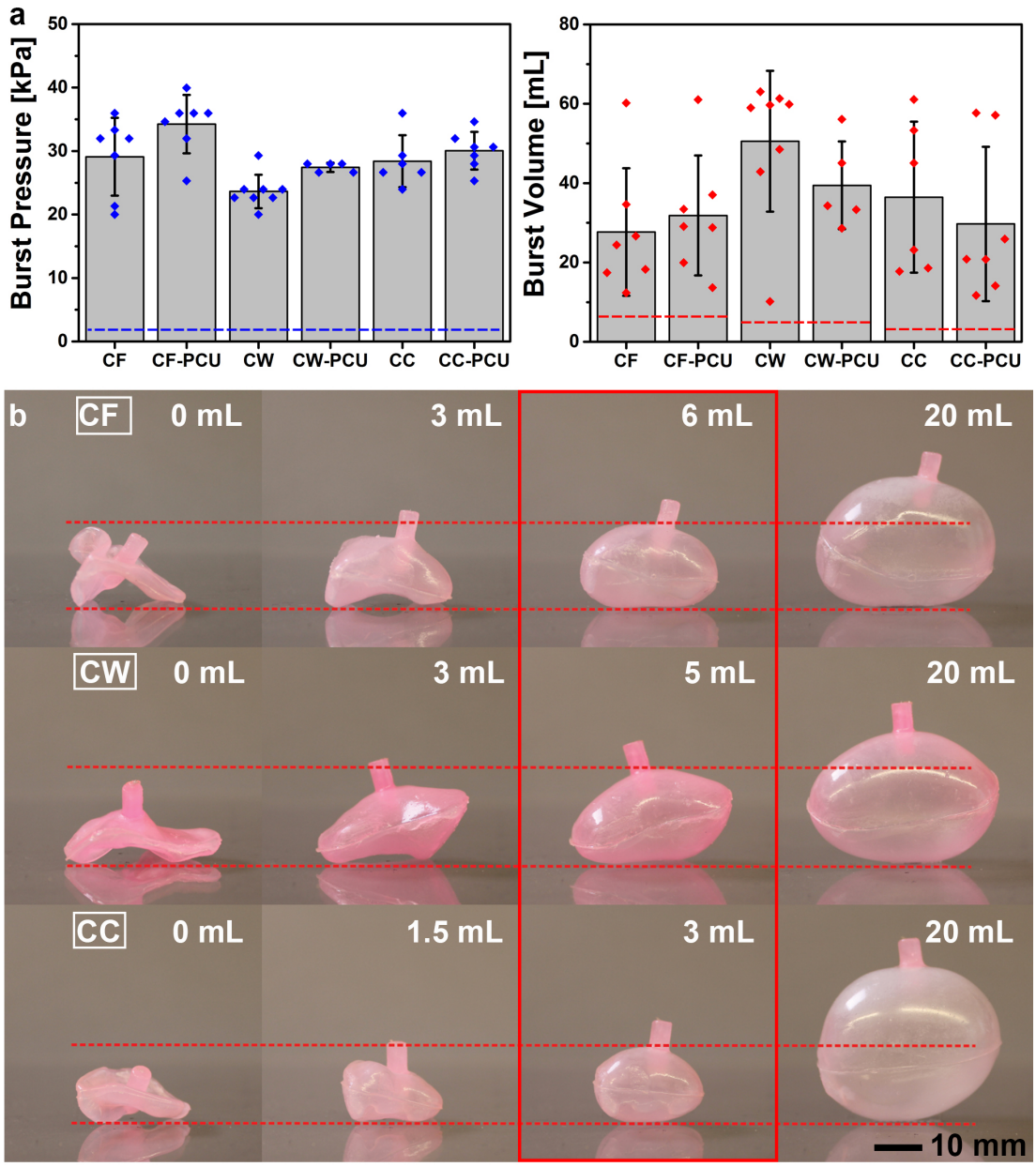

Figure 2.4 | Performance of inflated occluders. (**a**) (left) Burst pressures of occluders of varying morphologies, with typical left atrium (LA) pressure marked by blue dashed line. (right) Burst volumes of occluders with varying morphologies, with the target volume needed to occlude LAA marked by red dashed lines. ($n \geq 5$, error bars, mean ± s.d., data points displayed) (**b**) Cauliflower (CF), Chicken Wing (CW), and Cactus (CC) occluders inflated to various volumes. We placed red dashed lines above and below the target volume needed to occlude LAA, which we also boxed in red.

2.6 Performance of Valve

We chose to monolithically integrate a valve into the occluder during the silicone molding process mentioned above since that would allow us to inflate the occluder to high pressures without delamination of the valve from its walls. We added wings to the internal side of the valve to protect the opposing wall of the occluder from getting pierced accidentally during deployment (Fig. 2.1b). We extended the top of the valve outside of the occluder to have a portion of it protruding from the distal tip of the LAA during the deployment procedure (Fig. 2.1b-c). This extension allows the surgeon to maintain physical contact with the occluder throughout the entire procedure. Also, this extension of the occluder acted as a secondary anchoring site after the surgeon sutured it directly to the LAA tissue (Fig. 2.6c, right).

To test the performance of the valve, we integrated it into rigid spherical balloons (Fig. S2.7). In addition to the valve under test (which was the same size as the occluders), these balloons have a second larger valve used to attach them to a nozzle. These balloons were fabricated using the same methods as above for the LAA occluders, except instead of a PCU coating, we used a rigid epoxy (5Minute®Epoxy, Devcon) to dip-coat the silicone balloons. Before coating these balloons in epoxy, we inserted a nozzle through the larger valve. We then encased the balloon and part of the nozzle in epoxy, while leaving the test valve uncoated. Using a 0.45 mm needle, we pierced a hole into the valve under test, and then attached the fixed nozzle to the syringe pump (Fig. S2.6). We incrementally added water to these balloons at a rate of 0.25 mL/min while measuring the pressure (Fig. S2.7). We found the experimental setup failed between ~160-670 kPa, either the epoxy surrounding the balloon cracked, or there was a leak where we connected the tubing to the pressure sensor (we did not observe any leaks from the valve under test). Since the minimum pressure (i.e., 160 kPa) at which we observed failure in the setup was ~310% higher than the maximum pressure that the occluders can sustain before bursting (Fig. 2.4a, left), we don't expect to see any leakage from the valves during their normal function.

2.7 In-vitro Occlusion of LAA

We performed *in vitro* tests that mimic the environment and anatomy of the LAA using a custom-built flow system that provides a pulsatile fluid flow (Fig. 2.5a, left). Using the segmented LAA blood volume and CAD, we designed, and 3D printed molds to fabricate a silicone model of the human LAA CF morphology (Fig. S2.8, see SI for details). We then attached this model to our flow system that consists of an idealized left atrium connected to two centrifugal fluid pumps that mimic blood flow. A microcontroller (Arduino Uno™) acted as an alternating switch to regulate the flow produced by the two pumps. This alternation between the two pumps allows water to flow in and out of the LAA model in a pulsatile fashion.

We implanted the CF LAA model with either a patient-specific CF LAA occluder (Fig. 2.3a-c, left most images) or a spherical occluder (16 mm diameter; Fig. 2.5b). The size of the spherical occluder was chosen based on the average of multiple measurements taken using Geomagic Wrap's analysis tool across the LAA body just below where the valve would extend from the LAA. After implanting the occluder into the CF LAA, we added green dye (Food Coloring, Shurfine™) to the atrium of the set-up (Fig. 2.5b). We then waited to see if the green dye could flow past the ostium into the distal end of the silicone LAA. For each test, we increased the volume of the occluder by filling them with water dyed red (Food Coloring, Shurfine™) using a syringe. At smaller occluder volumes, the green dye quickly (< 1 min) leaked past the ostium and into the distal tip of the CF LAA. However, as the volume inside the occluder neared the occlusion amount (~4mL for spherical and ~5.5mL for patient-specific), we waited longer times (~2 hours) to ensure no green food coloring leaked past the ostium.

To determine the pressure inside occluder while it was in the silicone CF LAA model, we attached the previously describe syringe pump and pressure sensor and then added water to the occluder at a rate of 2.5 mL/min (Fig. 2.5A, right). The patient-specific occluder was designed to match the elliptical geometry of the CF LAA ostium. To

demonstrate this, we heated wax (Paraffin Wax, WaxWel) to 80 °C so that it was in its liquid state and then poured it into the silicone LAA up to the ostium, while the occluder was implanted and filled to the previously determined occlusion volume. We allowed this wax to solidify within the CF LAA (Fig. 2.5c, middle). We then peeled back the silicone CF LAA and removed the occluder with the wax still adhered to it (Fig. 2.5c, right). We found that there was approximately 210% larger volume of wax adhered to the spherical occluder versus the patient-specific occluder. Due to its size, the spherical occluder is seated further back from the ostium than the P-S occluder. If we had fabricated a larger diameter sphere, then it possibly could have protruded out to, or even past the ostium. However, a larger sphere could have also pushed on the walls of the LAA and probably the surrounding anatomy.

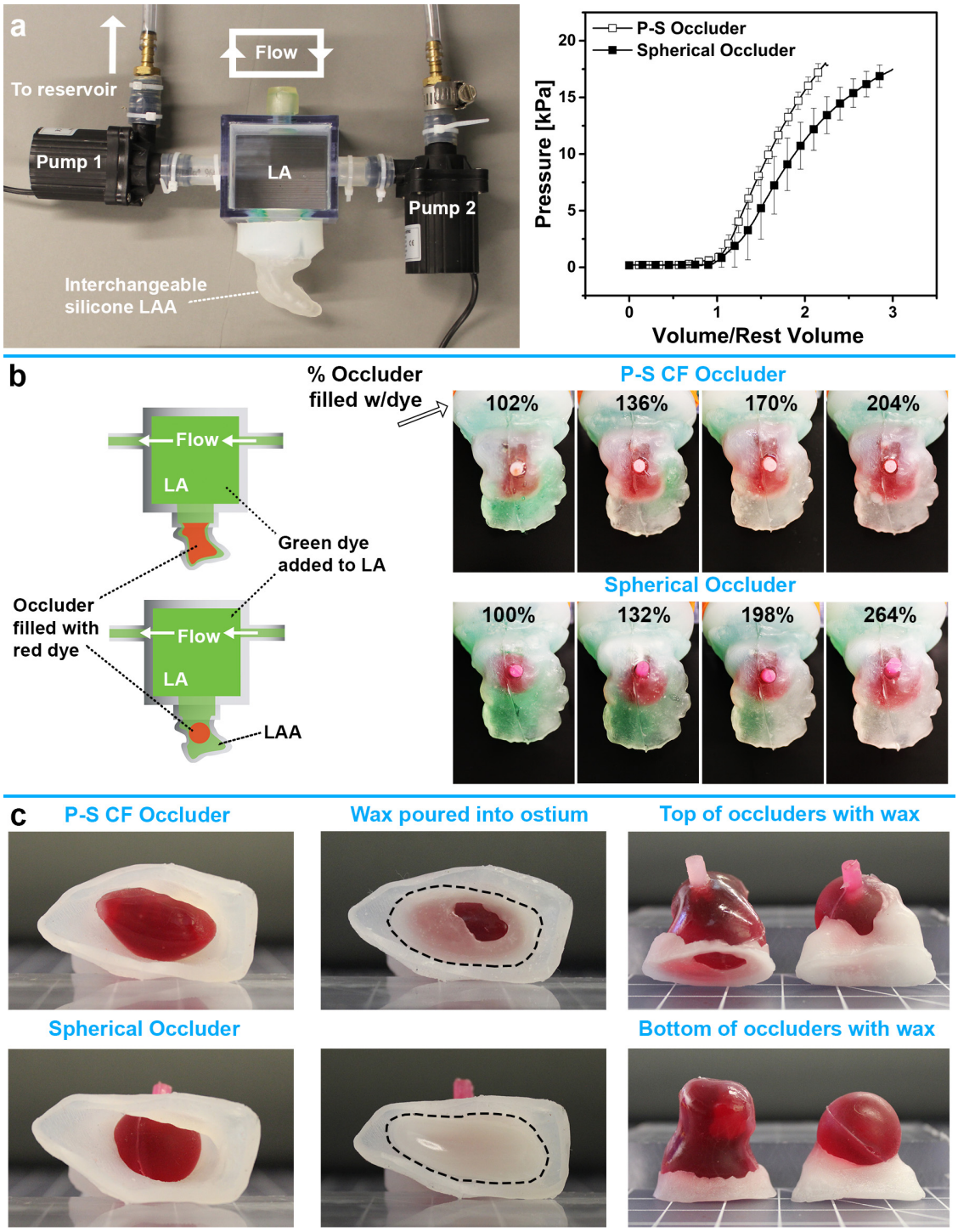

Figure 2.5 | Occlusion performance of patient-specific design. (**a**) Left, photo of *in-vitro* flow loop to test LAA occlusion. Right, the pressure-volume behavior of occluder while implanted in silicone LAA. ($n \geq 4$, mean ± s.d.) (**b**) The schematic on the left represents the left atrium (LA) and CF LAA with either a patient-specific (P-S) or

spherical occluder in position. As we increased the volume inside the occluder, we started to block the green dye from the distal portion of the LAA, as seen in the photos on the right. We adjusted the contrast of these images in Photoshop® for better visualization of the green dye. (**c**) Left, photos of frontal view of the ostium of the silicone LAA with either P-S or spherical occluder implanted. The occluders have been filled with red dye. Middle, liquid wax was added to the ostium and allowed to solidify in place, ostium traced by black dotted line. Right, we removed the occluder with the attached wax from the silicone LAA (P-S is on the left of both top and bottom images).

2.8 Delivery System

We designed this soft occluder and, more specifically, the valve added at its distal tip for a surgical-based delivery and deployment. The delivery system consisted of polyimide lumen to transport the biocompatible epoxy (Epo-Tek® 301, Epoxy Technology) into the occluder (Fig. 2.1b, 2.6a). Using a rotational shear rheometer, we determined the cure time of this epoxy to be ~115 min at body temperature (37°C; Figure S9). This lumen was coupled to a sheath and a catheter, which were used to house the occluder and provide a hemostatic valve, respectively (Fig. 2.6a). Also, we threaded a nylon suture through the valve for retrieval and recovery in the chance of an embolized occluder (Fig. 2.1b, 2.6a). We attached the patient-specific occluder to the delivery system by inserting the lumen (1 mm outer diameter, OD; Medical Tubing, Vention) all the way through the valve. We did this by first puncturing the valve with a 0.45 mm needle, and then stretching the elastomeric material around a blunt, 1.8 mm OD metal tube. We then passed the lumen through this metal tube to the inside of the occluder, and we slid the metal tube out of the valve, in this way the elastomeric material of the valve sealed around the outer wall of the lumen. We attached a 3-way stopcock to this lumen and two syringes of different sizes (one 20 mL and the other 60 mL). We used the larger syringe to vacate air from the occluder, and the smaller syringe to fill the occluder with the biocompatible epoxy. We vacated and inserted the occluder into a 5 mm inner diameter, transparent polyethylene terephthalate sheath (Medical Tubing,

Vention), which had two slits on its distal end. We then pulled this transparent sheath, containing the occluder, backward into the distal end of a 6 mm OD catheter (18 F, Check-Flo Performer Introducer, Cook Medical).

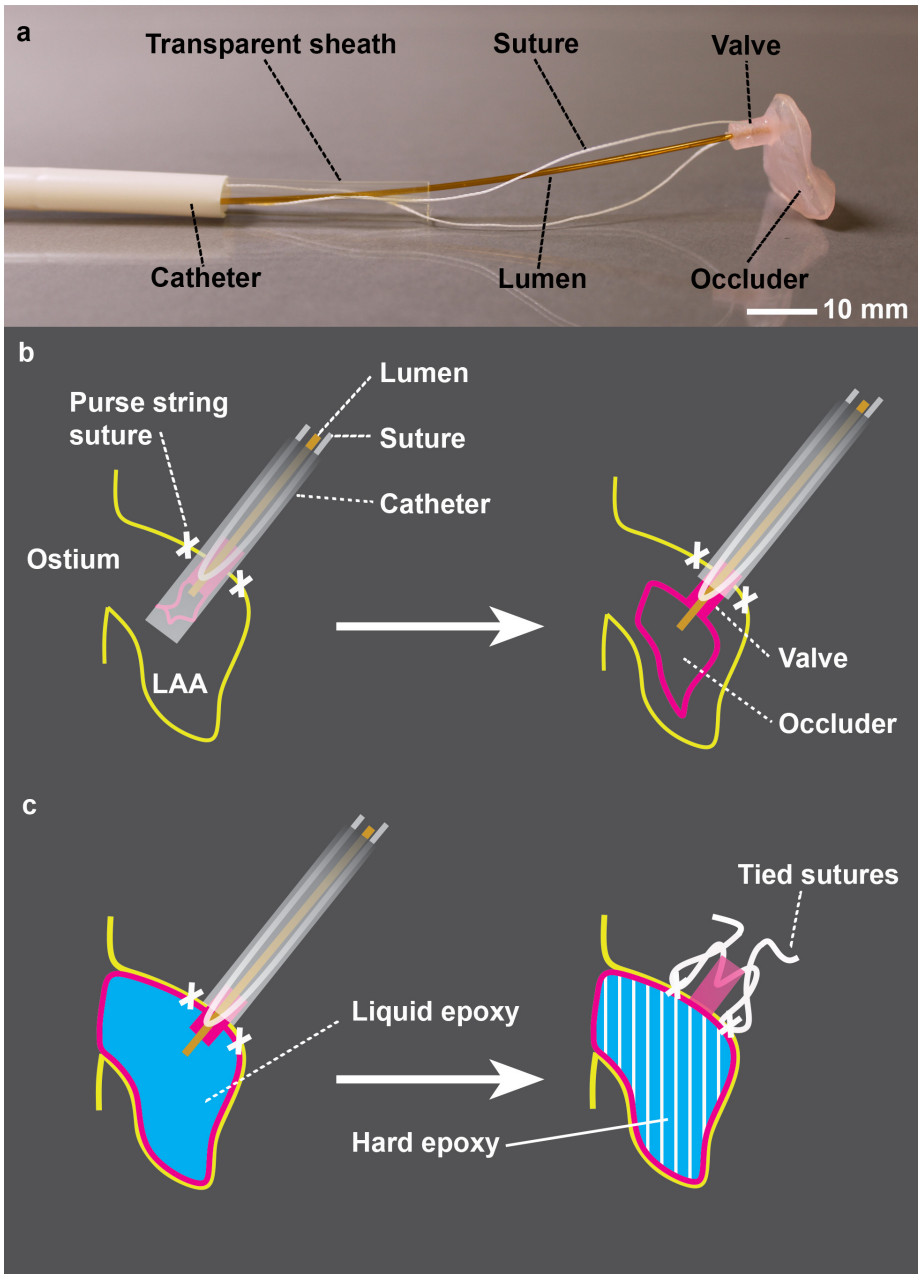

Figure 2.6 | Delivery system and deployment method used in this study. (**a**) Photo of delivery system attached to occluder. Starting at outer-most layer and working inward toward the LAA: 18 Fr catheter cut to approximately four inches in length, transparent

semi-flexible polyethylene terephthalate sheath with two slits cut at its end, polyimide inner lumen extends into the occluder, nylon suture through valve of occluder. (**b**) Schematic of deployment method. Placement of purse-string sutures and insertion of the delivery system (left); deployment of soft, patient-specific occluder (right). (**c**) Orientation and inflation of occluder with epoxy (left). We tied the suture that is inside the valve to purse-string sutures. After approximately one hour, the epoxy starts to gel fixing it in place. After 24 hours, the epoxy is fully cured in place (right).

2.9 Implantation of Soft Occluder in a Canine Model

We demonstrated device functionality (delivery, deployment, anchoring stability, and occlusion) in the beating heart of a healthy, mongrel canine. The study was in accordance with the Guide for Care and Use of Laboratory Animals and was approved by the Institutional Animal Care and Use Committee of American Preclinical Services (Minneapolis, MN). The canine model was appropriate for this study due to the similarity to human cardiovascular systems, particularly the size and general morphology of the LAA.

Two weeks prior to the surgical procedure the veterinary team obtained the canine's cardiac CT scans using Siemens' SOMATOM Definition (Fig. 2.1a, left; 2.7a, left). We used these scans and the methods described above to design and fabricate a soft, patient-specific occluder (Fig. 2.7b). To reduce the risk of thrombotic events during the procedure, the veterinarian team placed the animal on antiplatelet (Aspirin, 81mg and Clopidogrel 75mg) one day prior to surgery. The day of the procedure, the veterinarians delivered general endotracheal anesthesia to the canine. The veterinary surgeons performed a thoracotomy and pericardial incision to access the LAA. They placed a purse string suture in a pre-determined location on the distal end of the LAA (Fig. 2.6b, left). The surgeon then made an incision in the center of the sutures and guided the delivery system into the atrial space; pulling the purse-string sutures tight to prevent blood loss through the space surrounding the catheter (Fig. 2.6b, left). They retracted

the catheter to expose the transparent sheath, which contained the occluder. The slits in the sheath allowed the occluder to be released easily into the LAA (Fig. 2.6b, right). The surgeons then pulled the delivery system back, along with the occluder, until the top end of the valve of the occluder came through the distal tip of the LAA (Fig. 2.6c, left). Next, they cinched the purse string sutures around the elastomeric valve, preventing any bleeding through the LAA before they filled the occluder. They properly oriented the occluder under the guidance of fluoroscopy (Siemens Avantic) and 3D transesophageal echocardiography (TEE; Siemens Cypress II; Fig. 2.7c, left; S2.10-2.11). Once oriented, we filled the occluder with the biocompatible epoxy until full occlusion of the LAA was achieved, as assessed through TEE and fluoroscopy. We then removed the lumen from the valve, and the surgeons used the sutures from the purse string and tied them to the nylon suture looped inside of the valve for additional anchoring. The veterinarians took cardiac CT scans immediately following the procedure (Fig. 2.7a-b, right). At that time, we viewed a bubble of air approximately 170 μL in volume trapped inside of the occluder, possibly due to incomplete evacuation of air before infusion of the epoxy (Fig. 2.7b, right; Fig. S2.10). After 24 hours, the veterinarians performed a necropsy; the epoxy inside the occluder was fully cured, and the occluder was anchored in the correct orientation inside the LAA (Fig. 2.7c, right).

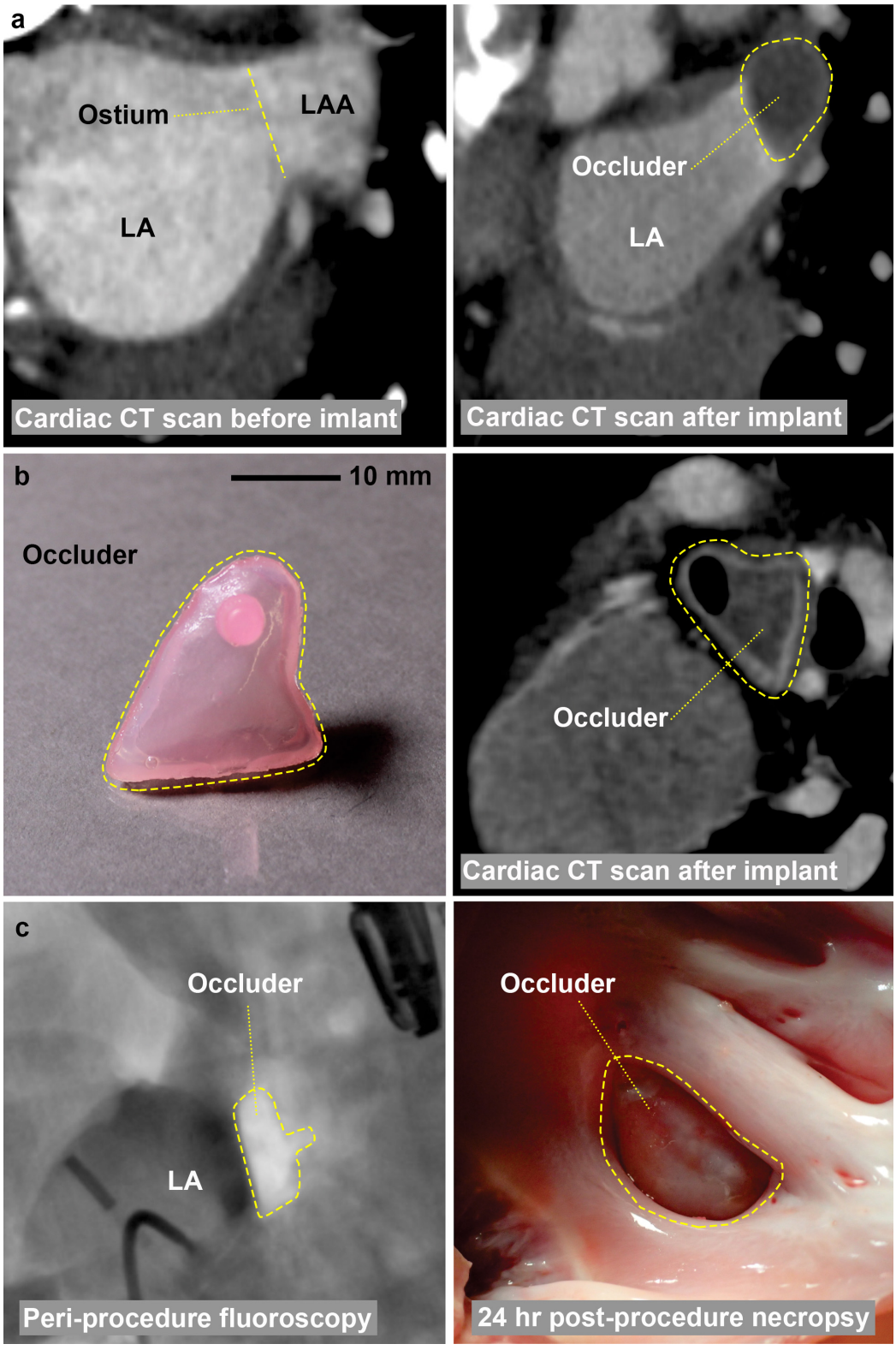

Figure 2.7 | Large animal in vivo study. (**a**) Coronal view of cardiac CT scan obtained two weeks before procedure, coronal view of cardiac CT scan immediately following

surgery (occluder outlined by yellow dotted line). (**b**) Soft, patient-specific occluder fabricated for this canine study, and sagittal view of the occluder (traced by yellow dotted line) within LAA in post-operative cardiac CT scan. In this image, the air bubble that became trapped within the occluder is visible. (**c**) Peri-procedure fluoroscopy image after inflation of occluder within LAA, and a photo of occluder anchored in place 24 hours post-procedure necropsy.

2.10 Conclusion

We developed workflows for the design, fabrication, and deployment of a soft, patient-specific left atrial appendage occluder to prevent stroke in patients with atrial fibrillation. This device demonstrates a novel approach for fabrication of personalized cardiovascular implants, which are durable and hemocompatible. Furthermore, the approach or similar incarnations can be applied more broadly to treat a variety of cardiovascular diseases, where the size and shape of conventional implants and/or complex patient anatomy exclude patients from treatment, or result in decreased device efficacy.

We achieved patient-specificity by using CT imaging to dictate the initial geometry of the occluder, and by fabricating the occluder as an inflatable balloon that can conform to the irregular shape of the LAA using an elastomeric composite of Dragon Skin®20, Sylgard®184, and ChronoFlex AR®. While medical balloons with custom geometries are commercially available, we demonstrate a process utilizing 3D printing for rapid fabrication of patient-specific LAA occluders that feature: i) a monolithic valve for one-way filling of the occluder, ii) a method for anchoring to the LAA after deployment, and iii) development of composite elastomer layers and chemical treatments to bond those layers to ensure hemocompatibility and proper mechanics. Furthermore, we showed the advantage of patient-specificity over a less custom design (e.g., spherical balloons) through *in vitro* occlusion tests using our custom bench-top flow loop. We found that the personalized occluder prevents residual flow at much lower strains than

the spherical design. This improved performance will ensure safer operation of the occluder and decrease the risk of putting additional strain on the LAA and/or surrounding cardiac tissue. Additionally, the patient-specific design yielded smoother interfaces at the ostium of the atrium with smaller crevices than the spherical design; the smaller crevices suggest the patient-specific design will less likely be a nidus for thrombus formation.

Although this work is a proof-of-concept, we demonstrated the feasibility of the workflow, functionality, and performance of our device by implanting it into a large animal model two weeks after cardiac CT scans were received. This timeline could be reduced to a few days and could easily be scaled up by printing multiple molds at a time. In this way, the cardiac surgeon could have several backup devices for a single procedure. We included a multifunctional valve in the design to enable the surgical deployment, filling, and anchoring of the occluder. We applied up to approximately 670 kPa of pressure to these valves, demonstrating their ability to prevent any leakage. For the *in vivo* implantation, we used a biocompatible epoxy to fill the occluder. We obtained anchoring of the occluder through applying sufficient pressure to the walls of the LAA, conforming to the internal anatomy of the LAA, and suturing the valve to the distal end of the LAA. It should be noted that the valve material extending out of the LAA can be removed after suturing in order to reduce the profile of the occluder, since it is not the functional part of the valve, but simply used as a grasping region of the occluder for the surgeon. The patient-specificity and excellent orientation of the device is clearly demonstrated in the post-procedure cardiac CT scan and necropsy image.

Other surgical techniques for exclusion (suture, stapling, etc.) have technical limitations that can result in incomplete closure, a remnant cul-de-sac, or even tears in the LAA[18,19,22]. We have performed a comparison of our patient-specific occluder to the AtriClip™, as a demonstration (Fig. S2.12). Current percutaneous devices for LAA closure are composed of metallic wire mesh, are round, and do not take into consideration the elliptical shape of the LAA ostium. Currently, cardiologists tend to

implant oversized closure device in order to enhance anchoring and to reduce the crevices around the ostium of the LAA (due to placing a round device in an elliptical structure). However, this runs the risk of applying too much pressure to the thin LAA walls and surrounding anatomical features, such as the mitral valve, and the circumflex artery[10]. This method of oversizing could lead to perforation of the heart wall by the metal barbs used for anchoring or, in the rare case, embolism of a device that substantially oversized[14].

Future studies should include a comparison of rigid and soft filling materials, hemodynamic flow analysis of the atrial-facing geometry of the occluder, and methods to decrease the overall form factor of the occluder. Saline solution or contrast dye are possible alternatives to using the biocompatible epoxy. They're safe, and can also double as a contrast agent to aid in occluder orientation via fluoroscopy during deployment. However, since these liquids do not harden in place; it is important to assess of the mechanical deformability of the occluder within the LAA. Although the patient-specific geometry used in this study was an improvement over the spherical design, computational fluid dynamic studies could lead to optimized architectures. In its current form, the wall thickness of this occluder is too large, but by decreasing the form factor, we could fit it into a smaller catheter to deliver it percutaneously. Smaller occluders could be produced using alternate methods of fabrication, such as dip-coating PCU around a dissolvable template. Instead of the current valve design, flap valves would decrease the occluder's overall size. Tissue glue could be used to adhere the distal portion of the occluder to the LAA, instead of the sutures applied in this study. Future research should also include longer duration *in vivo* studies, which would assess endothelialization of the occluder at the ostium of the LAA, long-term stability of the device, clot formation when anti-coagulants are not administered, and any remodeling of the LAA. In addition, implants into additional animals should be performed to ensure the generalizability of this novel approach, beyond the *in vitro* experiments presented in this work.

Medical 3D printing has been used extensively for education, surgical planning, and diagnostic assistance[3,4,31-34]. This technology enables personalized, cardiovascular implants and prostheses to be designed and rapidly fabricated. Furthermore, 3D bioprinting of cardiovascular tissue, while still in its infancy, could potentially revolutionize the field of interventional cardiology[5,35-38]. Currently, with the exception of personalized, rigid mitral rings[39], no other rapidly prototyped endocardial devices exist[3]. This work demonstrates the first patient-specific LAA occluder. This occluder could offer a non-pharmacological alternative to current surgical excision or exclusion methods, particularly in cases where the morphology causes occlusion to be challenging using the available devices. Additionally, the design process and manufacturing methods presented here could be used in any application where patient-specificity and soft materials are necessary.

2.11 Methods

2.11.1 Statistical analyses

Sample size, mean, and standard deviation are reported for all data sets. No statistical methods were used to pre-determine the sample-sizes for the characterization of the performance of the occluders. All statistical analyses were performed in Origin® (Academic Version, 2016) and Microsoft Excel (Excel for Mac, Version 15.32, 2017).

2.11.2 Code availability

The LabVIEW™ and Arduino Uno™ codes that were used in this study can be made available upon request to the corresponding author.

2.11.3 Data availability

The authors declare that all data supporting the findings of this study are available within the paper and its Supplementary Information.

2.11.4 Image acquisition

All photographs in the manuscript were taken with a Canon (EOS Rebel T3i), with the exception of Fig. 2.7c which was taken by the veterinary service performing the necropsy with an unknown digital camera.

2.10.5 Image processing

Except where explicitly stated (i.e. where we state that we changed the contrast), photographs were only cropped and positioned in figures using Adobe® Illustrator® (CS6, Version 16.0.3) and Adobe® Photoshop® (CS6, Version 12.0). SolidWorks® (Education Edition, 2016) renderings were performed using PhotoView 360® Add-In feature. Geomagic Wrap® (Version 2015) renderings were taken using the Snapshot feature. Pre-implantation CT images were obtained using Materialise Mimics® (Version 18). Post-implantation CT and fluoroscopy images were obtained using the Export Image feature of RadiAnt DICOM Viewer. Schematics were created using CorelDRAW® (Version 2017) or Adobe® Illustrator®. All arrows/dotted lines/text were added to images in Adobe® Photoshop® or CorelDRAW®. All plots were created in Origin® (Academic Version, 2016).

2.12 Supplemental Information

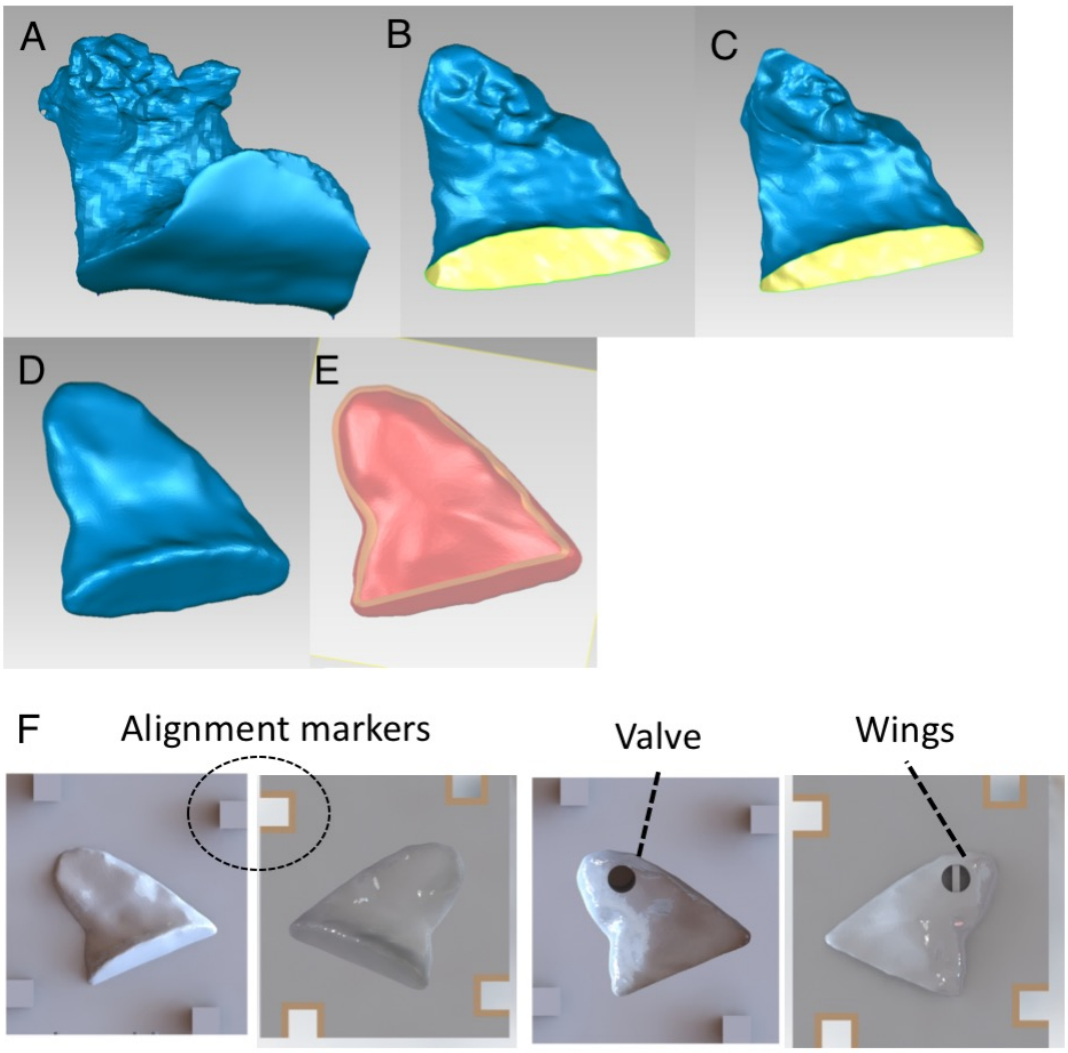

Figure S2.1| Geomagic Wrap® renderings of post processing steps of segmented LAA blood volume. (**a**) Segmented LAA blood volume. (**b**) Non-moldable features removed. (**c**) Surface profile offset uniformly inward by 1 mm (**d**) Surface features smoothed to meet the resolution of the 3D printer. (**e**) Cross section of design to display 0.5 mm inward shell. (**f**) CAD renderings of molds made in SolidWorks®.

2.12.1 CAD steps for occluder design

We designed molds in SolidWorks® by first importing the STL file of the shelled occluder. We then chose a region on the superior, distal surface of the occluder to place a valve. We created a reference plane parallel to the chosen surface, and then extruded a cylindrical valve, 4 mm in diameter and 13 mm in length. Part of this extrusion (6 mm) was on the outside of the occluder, and the remaining 7 mm was toward the inside of the occluder. We then added the wings of the valve by creating a small cutout at the inside end of this cylinder. This cut out was centered in the middle of the cylinder, it was 1 mm in width, and 2 mm in depth. Next, we created a reference plane which bisected the entire occluder. We chose a plane that would result in the least number of overhangs in the 3D printed mold. We extruded a box around the occluder, bisected it using this plane, and then removed the occluder using SolidWorks® combination-subtraction feature. This resulted in four parts: (1) the internal bottom surface of the occluder, (2) the external bottom surface of the occluder, (3) the external top surface of the occluder, that also contained the external half of the valve (4) and the internal top surface of the occluder, that also contained the internal half of the valve, (Fig. S2.1F, respectively). Once these four parts were created, we added alignment markers so that they would all fit together properly.

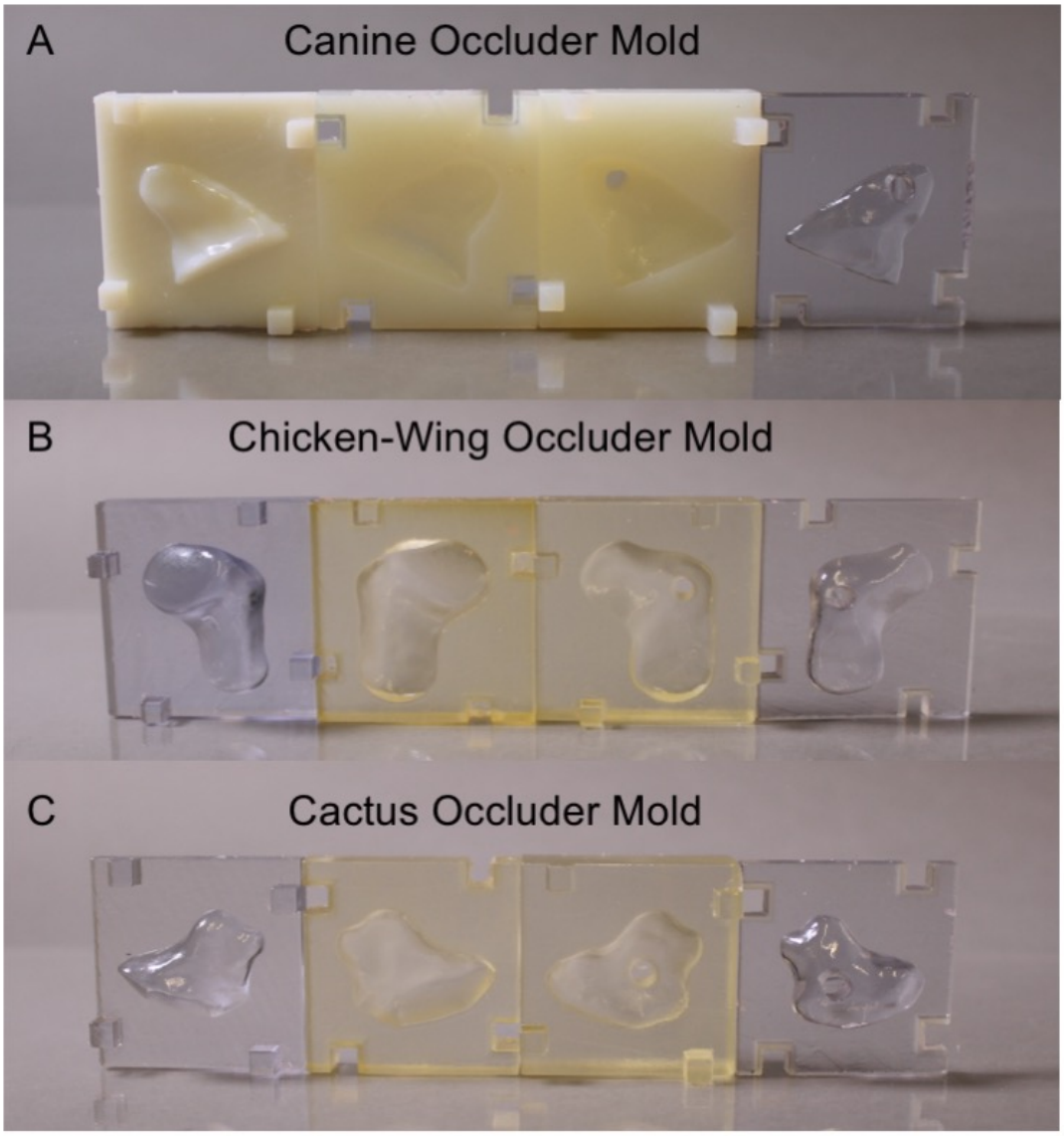

Figure S2.2| Photos of 3D printed molds for three LAA occluder morphologies (**a**) canine model used in the animal study. (The opaque, rigid mold on the far left was printed using VeroWhite. The opaque, soft molds in the middle were printed using Tango+. The transparent, rigid mold on the far right was printed using VeroClear.) (**b**) human chicken-wing, and (**c**) human cactus.

2.12.2 3D printing mold

Once the molds were designed in SolidWorks®, we printed them on our Objet260 Connex™ (Stratasys) high-resolution printer. We printed the internal molds using VeroClear, and the external molds using Tango+ (shore hardness of 85). To get a very smooth molding surface, we used the glossy setting and oriented the molding surface facing upward in the printer. Do to the irregular shapes of the LAAs, there were some regions where overhangs occurred, the printer is programed to lay down support material in these regions.

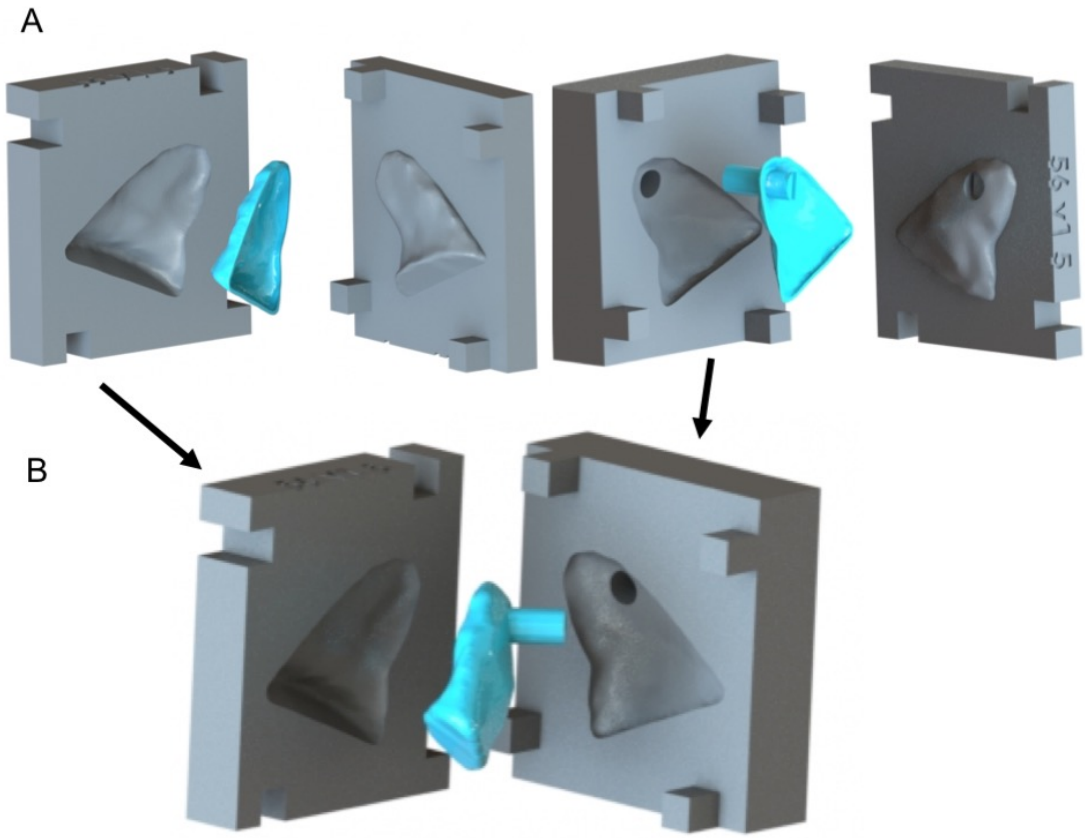

Figure S2.3| Silicone occluder molding process. (**a**) Molding two halves of the occluder, silicone is blue. (**b**) Bonding those two halves together using the same molds from the first step ensuring proper alignment. SolidWorks® renderings.

2.12.3 Fabricating occluders

After the parts were printed on our high-resolution printer (Objet260 Connex™, Stratasys), we cleaned them by scraping and power-washing away any support material from the print process. We then submerged them in regular tap water, and placed this into a 100°C overnight. Post-baking these printed parts is necessary to avoid mold inhibition. After baking overnight, we dried the molds, cleaned them again with an isopropanol (IPA, Sigma-Aldrich) soaked cotton swab, and then spray them with a thin coat of release agent (Polytetrafluoroethylene Film Release Agent, LPS). We let the release agent dry completely and then wiped away any excess residue with a cotton swab. Next, we mixed and degassed a pre-polymer solution of 69wt% Dragon Skin®20 (DS20; Smooth-On, Inc.), 10.3wt% Silicone Thinner® (Smooth-On, Inc.), 20.7wt% Sylgard®184 (Dow Corning; Fig. 2.2b), and two drops of Smooth-On Ignite® Fluorescent Pink Color Pigment (Smooth-On, Inc.). We put a small amount of this into a syringe with a long, blunt tip (1.5 mm inner diameter). This syringe was used to inject pre-polymer material into the cavity that would mold the valves. We filled each mold with pre-polymer, and placed all the molds under vacuum to remove air bubbles. We then slowly pushed together the matching molds, placed glass plates (3”x2”) on either side of the mold and secured them with large binder clamps. We placed these molds into the oven at 100˚C for 35 minutes. We bonded the two halves of the occluder as described above. We post-baked these occluders overnight at 100˚C. We rinsed the balloons in IPA and then air-plasma treated (PE-25, Plasma Etch) them on all both sides. We then quickly transferred them into a sealed container of 12% by volume 3-glycidoxypropyltrimethoxysilane in anhydrous ethanol (Silane, Sigma-Aldrich) for one hour. Since the occluders were full of air – and therefore buoyant - we placed the sealed container onto a benchtop shaker, the constant movement ensured all sides of the occluders were exposed to the Silane solution. We used forceps to remove the occluder by the distal end of the valve, we then sprayed them with IPA to remove excess ethanol. We sprayed them with nitrogen gas to remove the isopropanol and put them on a clean piece of foil into the 60°C oven for approximately five minutes to dry off any remaining

solvent. Next, we dip-coated the occluder in PCU. We diluted the received PCU 1:1 with dimethylacetamide (Sigma-Aldrich). We cured the PCU coating in the oven at 70˚C for 2 hours and then dipped the occluder a second time into the PCU solution. We did a final cure overnight at 70˚C.

2.12.4 Occluder wall thickness

The uniformity, of the total thickness of balloons was studied by slicing two occluders in different regions and imaging of the cross-sectional areas using an optical microscope. After studying 7 cross sectional areas, the variation of total thickness, excluding the seam area, was found to be less than 25%. The seams were found to be up to 100% thicker than the other areas.

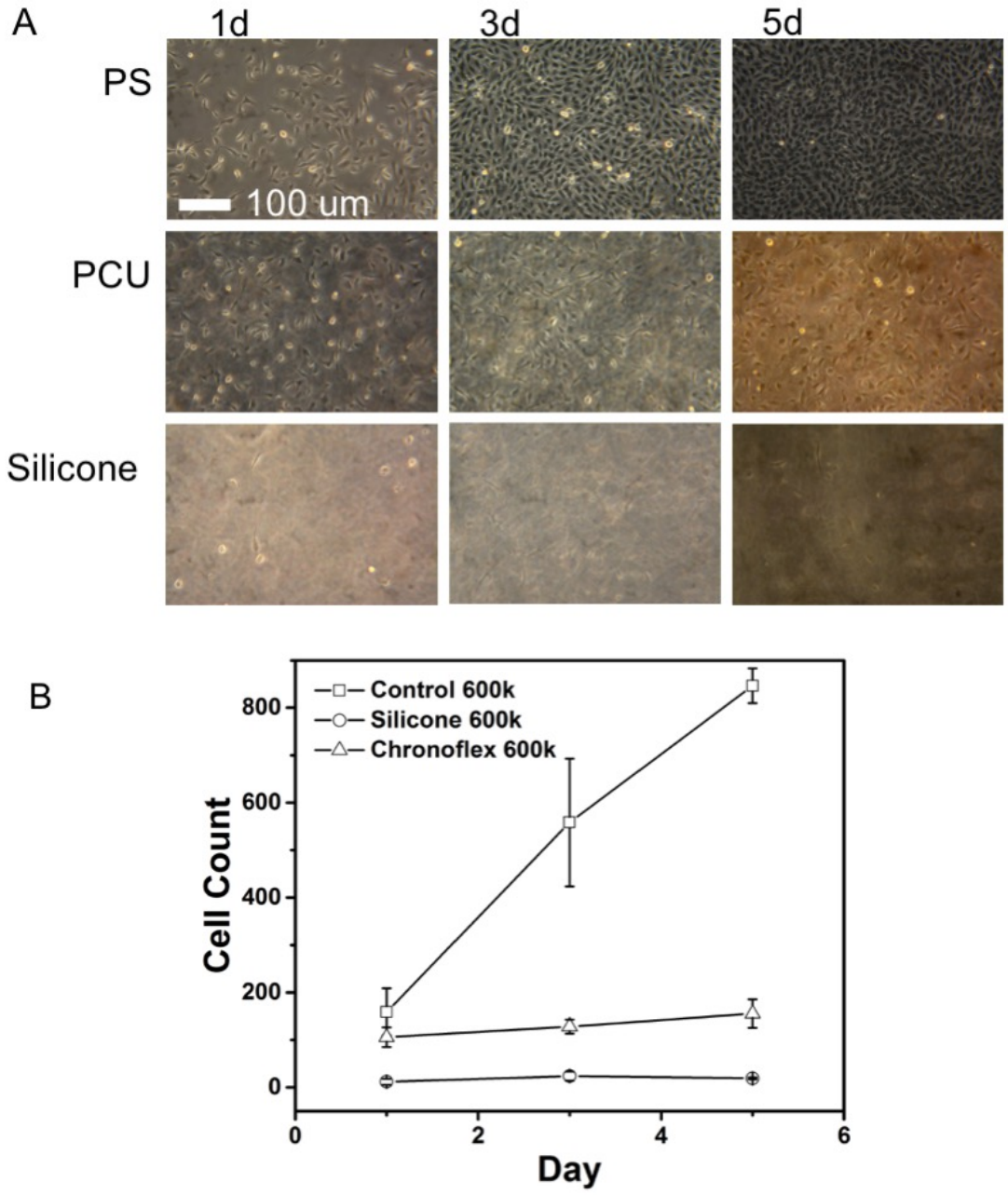

Figure S2.4| Endothelialization experiments. (**a**) Optical microscopy imaging of endothelialization of polystyrene (PS), polycarbonate urethane (PCU) and silicone blend after 1, 3, and five days. We adjusted the contrast of images using ImageJ for better visualization. (**b**) Cell count of endothelial cells on the materials used to fabricated occluder, plus the control of PS. (n = 5, mean ± s.d.)

2.12.5 Endothelialization of polymer materials

We cultured EA.hy926 human endothelial cells in a Dulbecco's Modified Eagle's Medium (DMEM), which was the base of the media containing essential amino acids and vitamins, along with 10% Fetal Bovine Serum, and 1% Penicillin and Streptomycin. We cultured the cells and waited until we observed confluence. After we observed confluence of the cells, we passaged the cells into a different flask to a 1:5 dilution cells to media ratio to keep them alive to run biocompatibility tests. Endothelial cells are adhering cells; therefore, the following protocol was used to suspend the cells into the media. Once we observed confluence, we removed the media via aspiration, and we performed a wash with Phosphate Buffered Saline (PBS), then aspirated the PBS and incubated the flask is for 5 minutes in a solution of 0.25% Trypsin-EDTA to suspend the cells. Once cells are suspended, we added media to stop Trypsin toxicity to the cells, and re-suspend the cells. After that, we extracted the volume necessary for a 1:5 dilutions and incubated the cells until we observed confluence. We fabricated samples by spin-coating the silicone blend onto the surface of a 1x4 inch cover slip. We set aside half of the glass cover slips and UV sterilized them for cell culture, the other half we treated with 12% by volume 3-glycidoxypropyltrimethoxysilane in ethanol to apply a PCU coating, using the same procedure as the occluders mentioned above. Once the PCU was fully cured, we sterilized the samples using UV. We used 600,000 cells in 15 mL of media to culture these two samples, along with a control sample of polystyrene (PS). After culture, we took digital images of 5 different points on the samples using a camera attached to the microscope at different times; one day, three days, and five days. The day after culture, we washed the plate with PBS and added new media, to remove any debris. We analyzed the images and averaged the cell counts to see the trend of confluence in the samples and control (Fig. S2.4). To facilitate better visualization of the cells in ImageJ the images of the cells were first Inverted, and then the Contrast was adjusted. Cells were manually counted using the Cell Counter tool in ImageJ. Counts were recorded in Excel. Data was analyzed in Origin®.

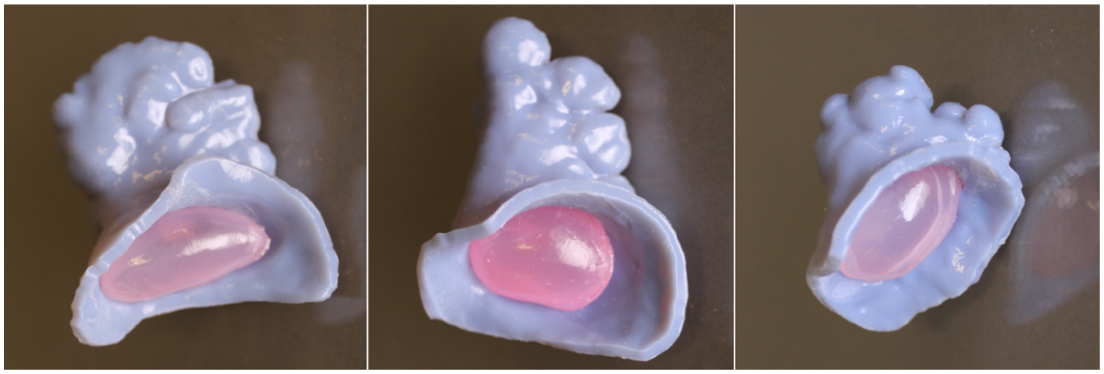

Figure S2.5| 3D printed LAAs containing patient-specific occluders of various morphologies. From left to right, Cauliflower, Chicken Wing, and Cactus morphologies are demonstrated. We printed these LAAs on a high-resolution 3D printer (VeroBlue RGD 840, Objet24; Stratasys.) and cleaned away the support material manually. We then implanted the patient-specific occluders and inflated them within the LAA.

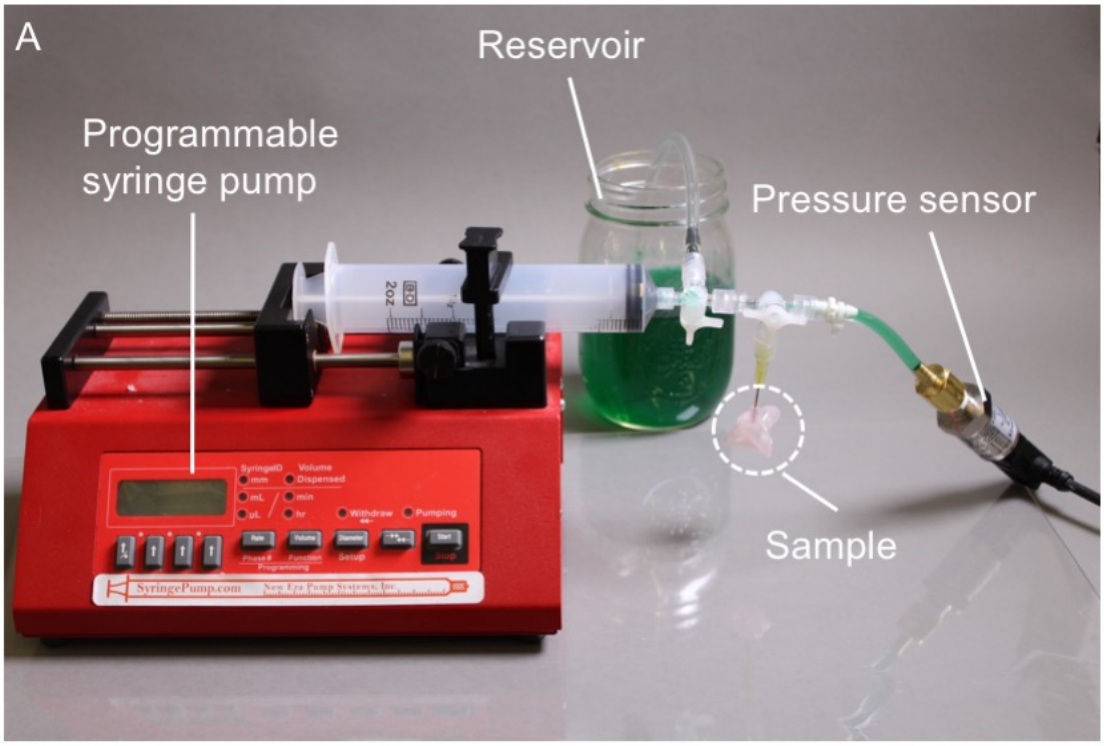

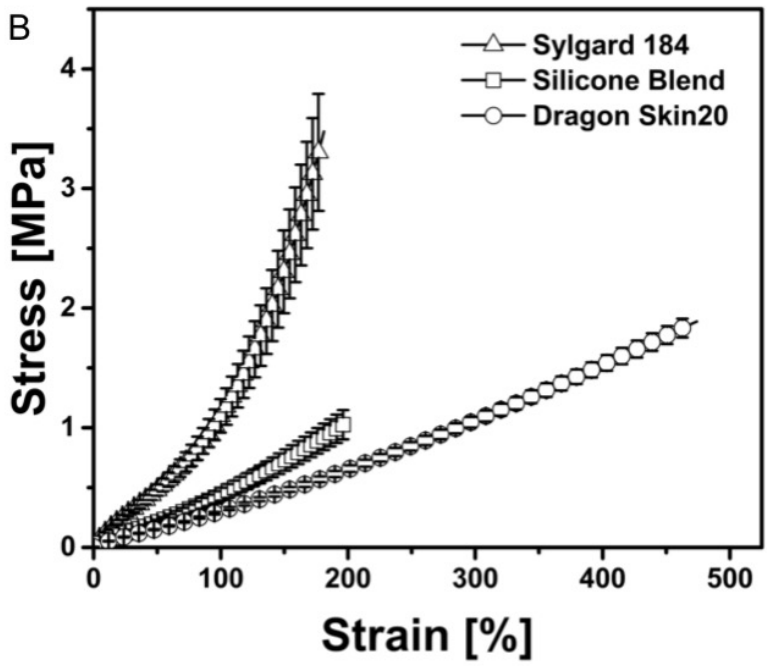

Figure S2.6| Pressure-volume set-up and tensile tests. (**a**) Photo of pressure-volume test set-up. (**b**) The uniaxial tensile behavior of Sylgard® 184, Dragon Skin®20, and the silicone blend of the two used in this study. ($n \geq 8$, mean ± s.d.)

2.12.6 Pressure-Volume Tests

All Pressure-Volume data in this manuscript was collected using custom LabVIEW™ code. The code controlled the input volume through a programmable syringe pump (NE-1000, New Era Pump Systems Inc.) and accepted the output pressure data from a pressure transducer. For the burst pressure and volume tests of the occluders we used a 0-15 PSI pressure transducer (PX26-015DV, Omega). If occluders were found to have holes/leaks at the beginning of the test, then they were discarded. We tested at least five distinct samples of each PCU coated and uncoated occluders.

2.12.7 Uniaxial tensile test

We performed tensile tests according to ASTM D412 on a Zwick Roell z010 instrument. All tests were conducted at room temperatures using a 10 kN load cell and a strain rate of 35 mm/min^{-1}. We fabricated samples by mixing and degassing each of the pre-polymer materials, and then pouring them into dumbbell molds. We then degassed these molds a second time and cured the material at room temperature. We tested at least 8 distinct samples of each silicone variety. The data were averaged across common X range and plotted with standard deviation. We chose to skip every 25 points to make data more visible

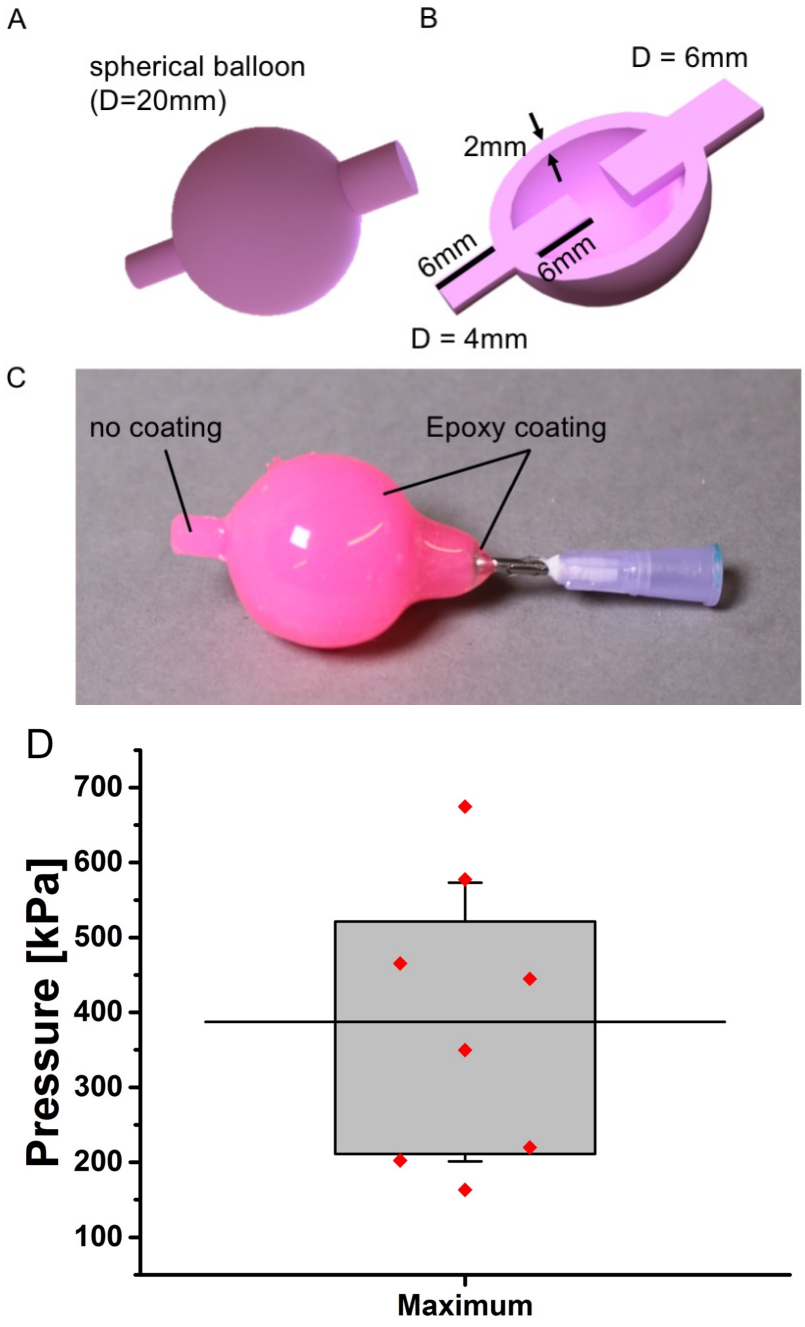

Figure S2.7| Valve performance. (**a**) SolidWorks® renderings of 20mm diameter spherical balloon with a wall thickness of 2mm. (**b**) Cross-section of CAD of the spherical balloon showing dimensions. The valve under test is the same dimensions as the fabricated occluders. (**c**) A needle was integrated into the balloon through the larger valve, and the entire sample was then coated with a layer of epoxy ~1mm thick,

excluding the valve under test. (**d**) Maximum pressure values from valve test. (n = 8, box determined by 25th and 75th percentile, black bar is mean, whiskers are s.d., data points displayed in red.)

2.12.8 Valve Tests

The pressure-volume data of the valves was collected in the manner as the burst volume/pressure of the occluders. However, the valves could go to much higher pressures, so we used a pressure transducer that could go up to 100 PSI (TDH30-CG-0100-03-D004, Transducers direct). We used 8 distinct samples when testing the valve performance. Samples that were tested inconsistently due to user error were discarded (i.e. testing the same sample twice, not adequately filling balloon before start of test).

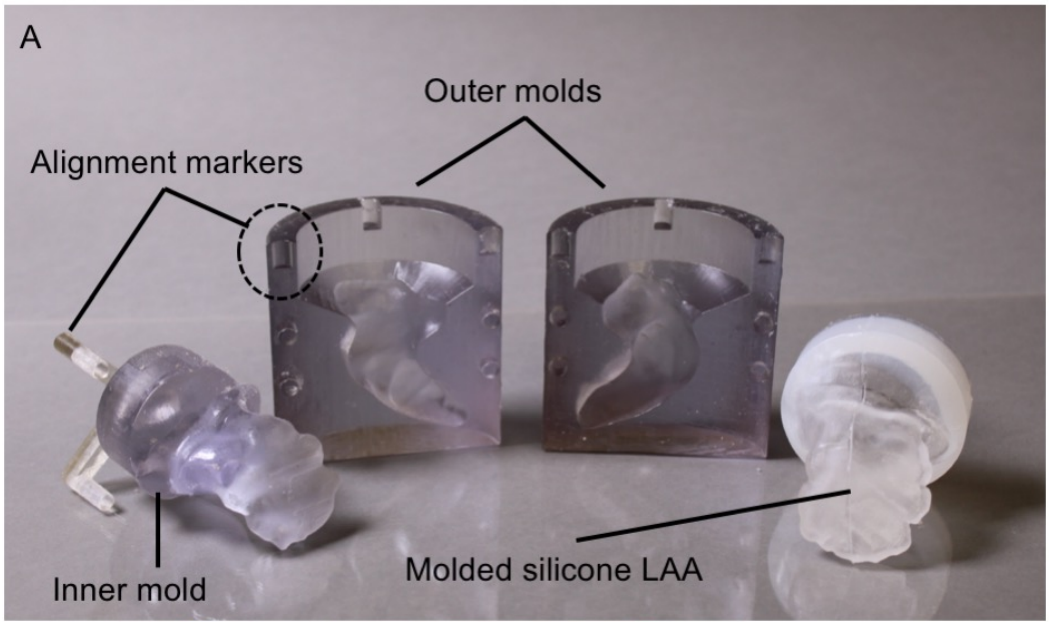

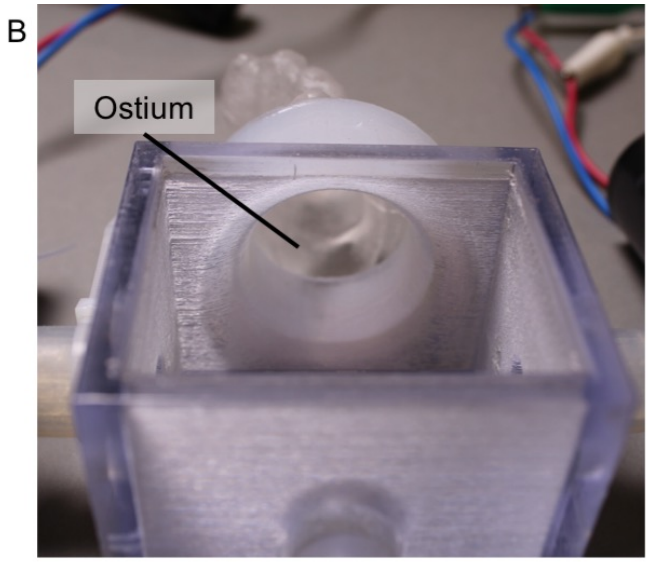

Figure S2.8| 3D printed parts for benchtop flow test. (**a**) 3D printed (VeroClear, Objet260 Connex™) three-part mold and silicone (Sylgard® bottom, Ecoflex® 0030 (Smooth-On, Inc.) upper) molded part of human LAA cauliflower morphology. (**b**) 3D printed bench top flow system zoomed in and angled to show ostium. Looking from the atrium into LAA.

2.12.9 Occlusion test

Each volume aliquot was tested three times for each occluder geometry. The same occluder (either patient-specific or spherical) was used throughout the test. Between each test the entire flow set up was cleaned and clear tap water was added to the system. Occluder filled with pre-determined volume was implanted into silicone LAA model. Flow was initiated by powering pumps (ZKWP03A, FORT-RIC). Dye was added to atrium. We waited for the dye to diffuse to the distal end of LAA. We photographed the occluder after the dye diffused to distal tip, or after approximately two hours (whichever came first). If the dye did not diffuse to distal end of LAA after 2 hours we called that occlusion.

2.12.10 Inflation of occluder within silicone LAA

For the pressure-volume data of the occluder implanted in the silicone LAA, we used LabVIEW™ to control an automated syringe pump to inflate the occluder and record data from a 0-15 PSI transducer (TDH30-CG-0015-03-D004, Transducers direct). The same occluder (either patient-specific or spherical) was used multiple times for this test. Data was imported into Excel® and converted into SI units. Data was then imported into Origin® where it was analyzed. Only tests that were run on the same day were used, four tests of patient-specific and six tests of spherical occluders. Data was averaged across X range and plotted with standard deviation. We chose to skip every 50 points to make data more visible.

Table S2.1. Descriptive data for a variety of occluder morphologies (mean ± s.d.).

	Cauliflower	Chicken Wing	Cactus
Occlusion Volume (mL)	6	5	3
Burst Pressure (kPa)	34.2 ± 4.6	27.4 ± 0.7	30.0 ± 2.9
Burst Volume (mL)	31.8 ± 15.1	39.4 ± 11.0	29.7 ± 19.5
Molded Thickness (μm)	500, 25% variation		
PCU Thickness (μm)	11-16, 18% variation		
Valve Pressure (kPa)	387.3 ± 185.92		

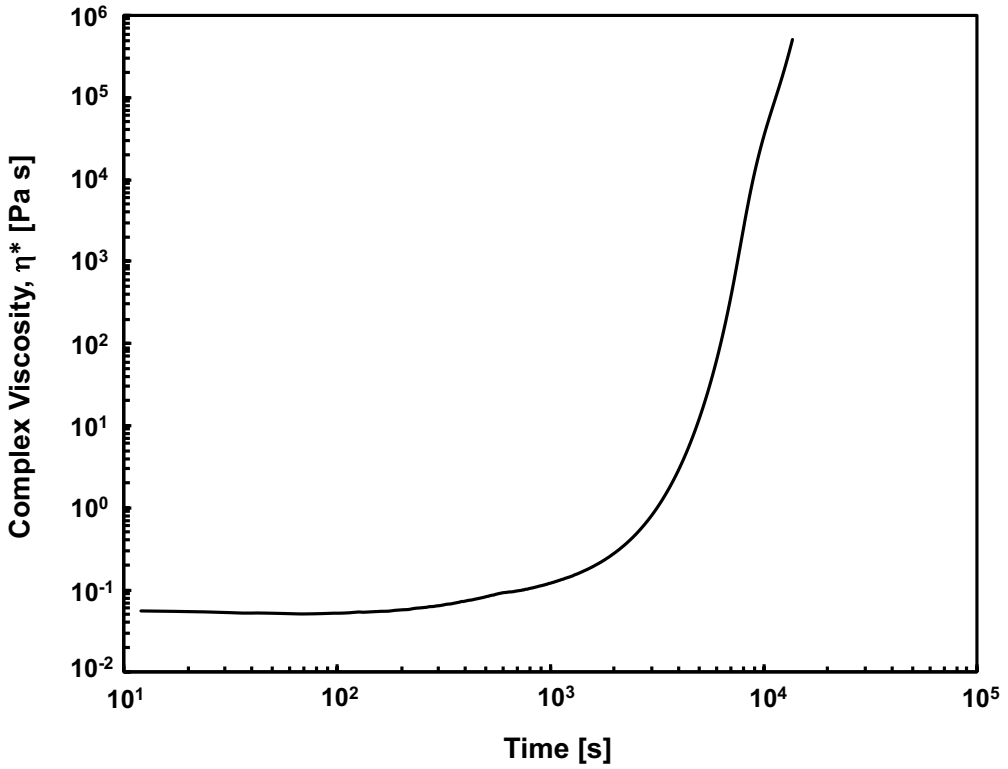

Figure S2.9| Complex viscosity over time of biocompatible epoxy (EPO-Tek® 301) at 37C.

2.12.12 Isothermal curing of EPO-Tek® 301

We performed isothermal (37°C) oscillatory rheology on the biocompatible epoxy using a cone (25 mm, 2°) and plate geometry at a frequency of 1.7 Hz, and a magnitude of oscillation of 1°. Data was collected using <0.5 mL of material on a rotational shear rheometer (Discovery Hybrid HR-3 Rheometer; TA Instruments). Only a single sample was tested. We plotted the complex viscosity as a function of time for this epoxy. The viscosity diverges toward infinity at the gelation point of the epoxy, this is the approximate time at which the surgeons can expect that the epoxy is no longer flowing inside of the occluder. We found this time to be approximately 115 minutes.

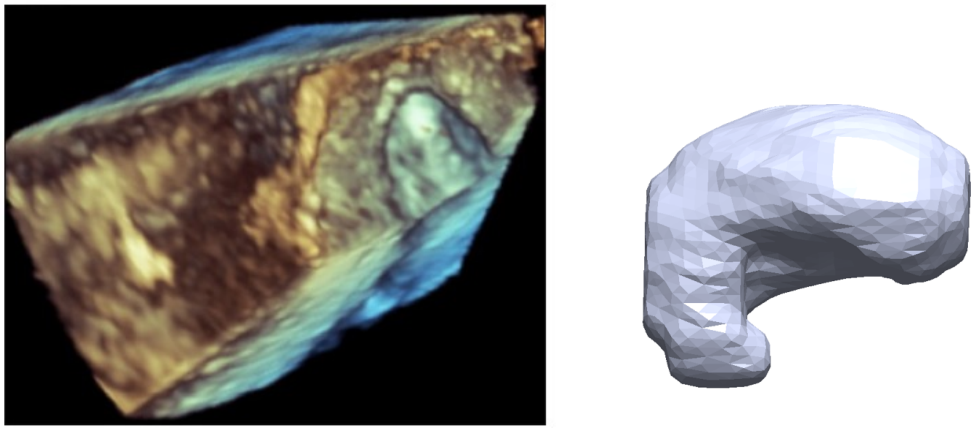

Figure S2.10| Post-procedure 3D Echo. SolidWorks® rendering of segmented air bubble from post-implantation CT scan of canine heart (bottom).

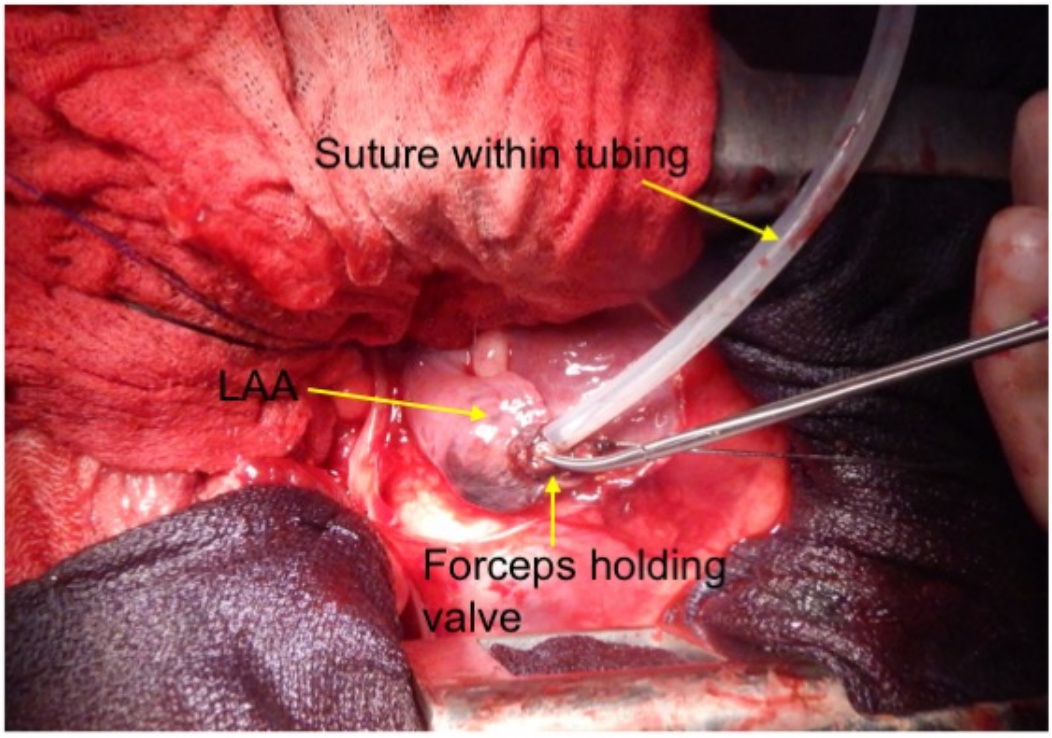

Figure S2.11| In-vivo, surgical deployment of patient-specific LAA occluder in the beating heart of a canine model. Surgeon maintains contact with the occluder during deployment: (1) nylon suture is looped through the external portion of the occluder's valve (this nylon string is kept out of the way by keeping it within a tube), and (2) forceps can also be used to clamp to the protruding tip of this valve as shown in this image.

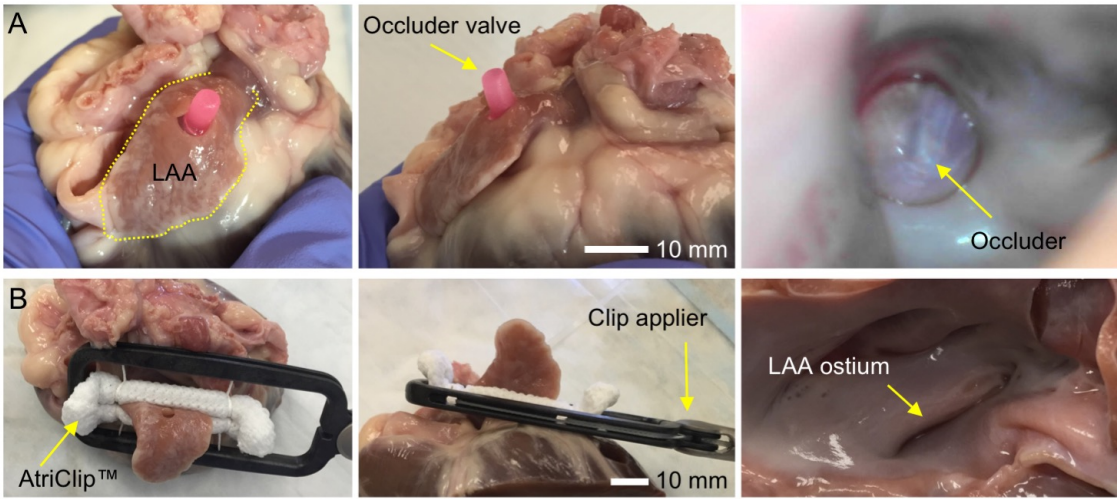

Figure S2.12| Comparison of patient-specific occluder and AtriClip™ LAA Exclusion System in an explanted canine heart. (**a**) Patient-specific, elastomeric occluder positioned within the LAA of canine heart, top and side views show soft protruding tip of occluder valve. The external portion of this valve can be removed with scissors after deployment of occluder. Right most image is of the ostium region of the occluder as seen from within the left atrium. (**b**) AtriClip™ LAA Exclusion System, with white AtriClip™ clamped around the LAA of explanted canine heart. Clip applier is still attached to the AtriClip™ to display the overall size of the delivery system. The clip size used here was 35 mm, the smallest size available. Right most image shows what the ostium of the LAA looks like after the AtriClip™ has been clamped down on the LAA.

2.12.13 Obtaining patient-specific scan of explanted canine heart

We thawed frozen canine hearts (Sierra for Medical Science; Whittier, CA) in lukewarm water for four hours. We then used a scalpel to remove unneeded tissues, including the majority of the left ventricle, taking care not to cut any portion of the left atrium or left atrial appendage. We used a cyanoacrylate gel (Loctite 454) to block the pulmonary veins, and finally a zip-tie to ensure a complete seal. We then suspended the heart upside down and poured silicone pre-polymer (Ecoflex 00-30; Smooth-On, Inc.) down the open left ventricle into the left atrium, taking care to fill the left atrial appendage. We let this

cure at room temperature for four hours. At this point the cured silicone mold was removed and the canine heart was stored in the refrigerator at 4°C. We spray painted the silicone using a matte silver color (Acryli-quik™; Krylon Industrial™) to allow for better visibility of the part during 3D scanning. Finally, we used a 3D scanner (Matter and Form; Toronto, CA) to obtain an STL model of the silicone mold.

2.12.14 Human CT Scans used in study

The IRB had determined that as only de-identified CT scans are being used for purposes of writing this manuscripts and other publications, this did not meet the definition of research with human subjects in accordance with the human research regulations at 45 CFR 46 and no separate IRB approval is needed

REFERENCES

[1] D. Mozaffarian, E. J. Benjamin, A. S. Go, D. K. Arnett, M. Blaha, M. Cushman, S. de Ferranti, J.-P. Després, H. Fullerton, V. Howard, M. Huffman, S. Judd, B. Kissela, D. Lackland, J. Lichtman, L. Lisabeth, S. Liu, R. Mackey, D. B. Matchar, D. K. McGuire, E. Mohler III, C. Moy, P. Muntner, M. Mussolino, K. Nasir, R. Neumar, G. Nichol, L. Palaniappan, D. Pandey, M. Reeves, C. Rodriguez, P. Sorlie, J. Stein, A. Towfighi, T. Turan, S. Virani, J. Willey, D. Woo, R. Yeh, M. Turner, *Circulation* **2015**.

[2] P. A. Wolf MD, R. D. Abbott, W. B. Kannel MD, *Stroke* **1991**, *22*, 983.

[3] J. L. Blackshear MD, J. A. Odell FRCS(Ed), *Ann Thorac Surg* **1996**, *61*, 755.

[4] L. Di Biase MD, P. Santangeli MD, M. Anselmino MD, P. Mohanty, I. Salvetti MD, S. Gili MD, R. Horton MD, J. E. Sanchez MD, R. Bai MD, S. Mohanty MD, A. Pump MD, M. Cereceda Brantes MD, G. J. Gallinghouse MD, J. D. Burkhardt MD, F. Cesarani MD, M. Scaglione MD, A. Natale MD, F. Gaita MD, *JACC* **2012**, *60*, 531.

[5] N. M. Al-Saady, O. A. Obel, A. J. Camm, *Heart* **1999**, *82*, 547.

[6] M. F. Stoddard MD, P. R. Dawkins MD, C. R. Prince MD, N. M. Ammash MD, *JACC* **1995**, *25*, 452.

[7] C.-M. Yu, A. A. Khattab, S. C. Bertog, A. P. W. Lee, J. S. W. Kwong, H. Sievert, B. Meier, *Nat Rev Cardiol* **2013**, *10*, 707.

[8] B. Kong, Y. Liu, H. Huang, H. Jiang, C. Huang, *J Thorac Dis* **2015**, *7*, 199.

[9] A. S. Kanderian, A. M. Gillinov, G. B. Pettersson, E. Blackstone, A. L. Klein, *JACC* **2008**, *52*, 924.

[10] E. S. Katz, T. Tsiamtsiouris, R. M. Applebaum, A. Schwartzbard, P. A. Tunick, I. Kronzon, *JACC* **2000**, *36*, 468.

[11] G. Ailawadi MD, M. W. Gerdisch MD, R. L. Harvey MD, R. L. Hooker MD, R. J. Damiano MD, T. Salamon MD, M. J. Mack MD, *J Thorac Cardiovasc Surg* **2011**, *142*, 1002.

[12] J. Snyder, A. M. Engel, K. C. White, N. Budiansky, J. M. Smith, *SS* **2012**, *03*,

28.

[13] N. C. Wunderlich, R. Beigel, M. J. Swaans, S. Y. Ho, R. J. Siegel, *JACC: Cardiovascular Imaging* **2015**, *8*, 472.

[14] S. Toumanides MD, E. B. Sideris MD, T. Agricola MD, S. Moulopoulos MD, *JACC* **2011**, *58*, 2236.

[15] J. D. Moss, *Curr Cardiol Rep* **2014**, *16*, 448.

[16] A. Aryana, S. K. Singh, S. M. Singh, P. G. O'Neill, M. R. Bowers, S. L. Allen, S. L. Lewandowski, E. C. Vierra, A. d'Avila, *Heart Rhythm* **2015**, *12*, 1431.

[17] V. Badhwar MD, J. S. Rankin MD, R. J. Damiano MD, A. M. Gillinov MD, F. G. Bakaeen MD, J. R. Edgerton MD, J. M. Philpott MD, P. M. McCarthy MD, S. F. Bolling MD, H. G. Roberts MD, V. H. Thourani MD, R. M. Suri MD, R. J. S. MD, S. Firestone MS, N. Ad MD, *Ann Thorac Surg* **2017**, *103*, 329.

[18] P. Su, K. P. McCarthy, S. Y. Ho, *Heart* **2008**, *94*, 1166.

[19] J. M. Lee, J. Shim, J.-S. Uhm, Y.-J. Kim, H.-J. Lee, H.-N. P. MD, M.-H. Lee, B. Joung, *The American Journal of Cardiology* **2014**, *113*, 963.

[20] J. F. Viles-Gonzalez MD, S. Kar MD, P. Douglas MD, S. Dukkipati MD, T. Feldman MD, R. Horton MD, D. Holmes MD, V. Y. Reddy MD, *JACC* **2012**, *59*, 923.

[21] S. A. Luis, D. Roper, A. Incani, K. Poon, H. Haqqani, D. L. Walters, *Cardiology Research and Practice* **2012**, *2012*, 1.

[22] J. O'Brien, D. Al-hassan, J. Ng, M. Joshi, C. Hague, S. Chakrabarti, J. Leipsic, *Int J Cardiovasc Imaging* **2014**, *30*, 819.

[23] A. M. Reed, J. Potter, M. Szycher, *Journal of Biomaterials Applications* **1994**, *8*, 210.

[24] M. C. Bélanger, Y. Marois, R. Roy, Y. Mehri, E. Wagner, Z. Zhang, M. W. King, M. Yang, C. Hahn, R. Guidoin, *Artif Organs* **2000**, *24*, 879.

[25] E. Braunwald MD, E. C. Brockenbrough MD, C. J. Frahm MD, J. Ross MD, *Circulation* **1961**, *24*, 267.

[26] M. Vukicevic, B. Mosadegh, J. K. Min MD, S. H. Little MD, *JACC: Cadiovascular Imaging* **2017**, *10*, 171.

[27] L. Lao, S. S. Robinson, B. Peele, H. Zhao, B. C. Mac Murray, J. K. Min, B. Mosadegh, S. Dunham, R. F. Shepherd, *Adv. Eng. Mater.* **2016**, *19*, 1600591.

[28] A. A. Giannopoulos MD, D. Mitsouras, S.-J. Yoo, P. P. Liu, Y. S. Chatzizisis, F. J. Rybicki, *Nat Rev Cardiol* **2016**, *13*, 701.

[29] A. A. Giannopoulos MD, L. Chepelev, A. Sheikh, A. Wang, W. Dang, E. Akyuz, C. Hong, N. Wake, T. Pietila, P. B. Dydynski, D. Mitsouras, F. J. Rybicki, *3D Printing in Medicine* **2015**, *1*, 1.

[30] S. Anwar MD, G. K. Singh MD, J. Varughese, H. Nguyen MD, J. J. Billadello MD, E. F. Sheybani MD, P. K. Woodard MD, P. Manning MD, P. Eghtesady MD, *JACC: Cardiovascular Imaging* **2016**, 1.

[31] F. Mahmood MD, K. Owais MD, C. Taylor, M. Montealegre-Gallegos MD, W. Manning MD, R. Matyal MD, K. R. Khabbaz MD, *JACC: Cardiovascular Imaging* **2015**, *8*, 226.

[32] D. B. Kolesky, K. A. Homan, **2016**.

[33] B. Mosadegh, G. Xiong, S. Dunham, J. K. Min, *Biomed Mater* **2015**, *10*, 034002.

[34] D. Y. Cheung, B. Duan, J. T. Butcher, *Expert Opin Biol Ther* **2015**, *15*, 1155.

[35] S. V. Murphy, A. Atala, *Nature Biotechnology* **2014**, *32*, 773.

[36] B. Derby, *Science* **2012**, *338*, 921.

[37] S. H. Sündermann, M. Gessat, N. Cesarovic, T. Frauenfelder, P. Biaggi, D. Bettex, V. Falk, S. Jacobs, *Interactive CardioVascular and Thoracic Surgery* **2013**, *16*, 417.

CHAPTER 3

STEREOLITHOGRAPHY FOR PERSONALIZED LEFT ATRIAL APPENDAGE OCCLUDER

Sanlin S. Robinson, Cameron Aubin, T. J. Wallin, Saleh Gharaie, Patricia A. Xu, Simon Dunham, Bobak Mosadegh, Robert F. Shepherd, *in submission*, **(2017)**

3.1 Introduction

Mass-produced medical implants typically come in several standard geometries and sizes which often fail to address the various patient morphologies encountered, particularly when a patient's anatomy is in a diseased state. With the advancements in high resolution imaging modalities, segmentation software, and rapid prototyping[1-4], the development of patient-specific implants has become more accessible to the medical community. To date, personalized implants have been fabricated for a variety of medical applications, such as airway disorders[5], mitral valve insufficiencies[6,7], craniomaxillofacial defects[8,9], and orthopedic replacements[10-12]. Due to manufacturing and chemistry limitations, most of these custom implants require fabrication from high elastic modulus ($E > 1$ GPa) materials that are mechanically dissimilar to the soft, elastomeric tissues of the human body ($E < 1$ MPa) [13]. Such rigid devices fail to conform to surrounding tissues, concentrate stress, and can perforate tissues[14]. Here we present a fast (~3 cm hr^{-1} draw-rate), low-cost (\$0.25 mL^{-1} of material), and scalable workflow for fabricating patient-specific medical implants via direct 3D printing of elastomeric polyurethane (EPU). To demonstrate this workflow, we have fabricated patient-specific left atrial appendage (LAA) occluders (Fig. 3.1a) for those at high risk of clot formation due to atrial fibrillation (AF).

Patients with AF have nearly a five times greater risk of stroke due to cardiac emboli[15], where 91% of these emboli originate in the LAA, possibly due to the low flow velocities of blood within this convoluted structure[16]. Blood-thinners are currently the first line of therapy to prevent stroke in high-risk patients, however, these drugs are effective in a narrow therapeutic window, require frequent and ongoing monitoring, increase the risk of internal bleeding, and can negatively interact with the individual's physiology or other drugs[17]. Therefore, occlusion of the LAA is recommended as an alternative for stroke prophylaxis[18-20]. Conventional surgical resection of the appendage not only hinders the contractile function of the remaining left atrial tissue[21] but also often results in incomplete closure (~36% of cases) which *increases* the risk of stroke[22,23]. The associated risks leads many practitioners to avoid recommending surgical interventions for occlusion. As an alternative, some mechanical LAA occlusion devices use a self-expanding metal alloy (nitinol) cage, available only in a set number of sizes, that deploy into a round dome to cap the ostium of the appendage[18-20]. Implantation of such rigid devices requires physically anchoring it using hooks that concentrate mechanical stress and can cause tears in the LAA and neighboring tissues, which presents significant challenges to safe delivery, proper deployment, and long-term health. Additionally, due to the high variability of LAA morphology – standardized occluder geometries often fail to completely block the ostium from residual blood flow. [14,24,25].

Recently our labs have shown the efficacy of patient-specific, soft, hollow LAA occluders [Robinson et al., *Nat. Biomed. Eng.* 2017] implanted in a canine model to address the issues of incomplete occlusion, perforation of LAA tissue, and device anchoring. Construction with elastomers is key to this advancement—the highly compliant endovascular devices are selectively inflated to fully conform to the complex LAA morphology at low volumes, which minimizes stress and damage to the surrounding tissues. Though fabricated via rapid prototyping (i.e., replica molding, lamination, and dip-coating), the workflow for constructing personalized occluders remains laborious and time-consuming; we required at least three days to fabricate the

patient-specific designs. Additionally, this strategy of manufacturing is incompatible with potentially un-moldable morphologies and requires a lamination step that introduces a seam that creates non-uniform wall thicknesses and compromises the mechanical integrity of the device. Herein, we demonstrate a rapid approach where we perform segmentation of the LAA from cardiac computed tomography (CT) scans, create a computer aided design (CAD), and 3D print the custom geometry to realize a monolithic, thin-walled elastomeric LAA occluder (Fig. 3.1). This process requires only ~12 hours.

Though various 3D printing technologies (e.g., Direct Ink Writing, Fused Deposition Modeling, Selective Laser Sintering)[7,26-28] have been used in medicine, we chose to use stereolithography (SLA) as it is especially promising in the fabrication of implanted devices. Based on layer-by-layer solidification of a liquid resin in response to photopatterned light (Fig. S3.1) SLA enables direct fabrication of complex, hollow elastomeric architectures with feature sizes on the order of 100 μm[2,29,30]. Additionally, by projecting multiple images onto the same build stage, we can rapidly (t_{print} ~1.5 hr) manufacture in a *single print* (*i*) multiple design variations for the *same* patient (i.e. iterate design complexity; Fig. S3.2a), (*ii*) multiple occluders for *different* patients (Fig. S3.2b, S3.3), and (*iii*) multiple copies of one design for one patient (i.e. scale up manufacturing; Fig. 3.1c).

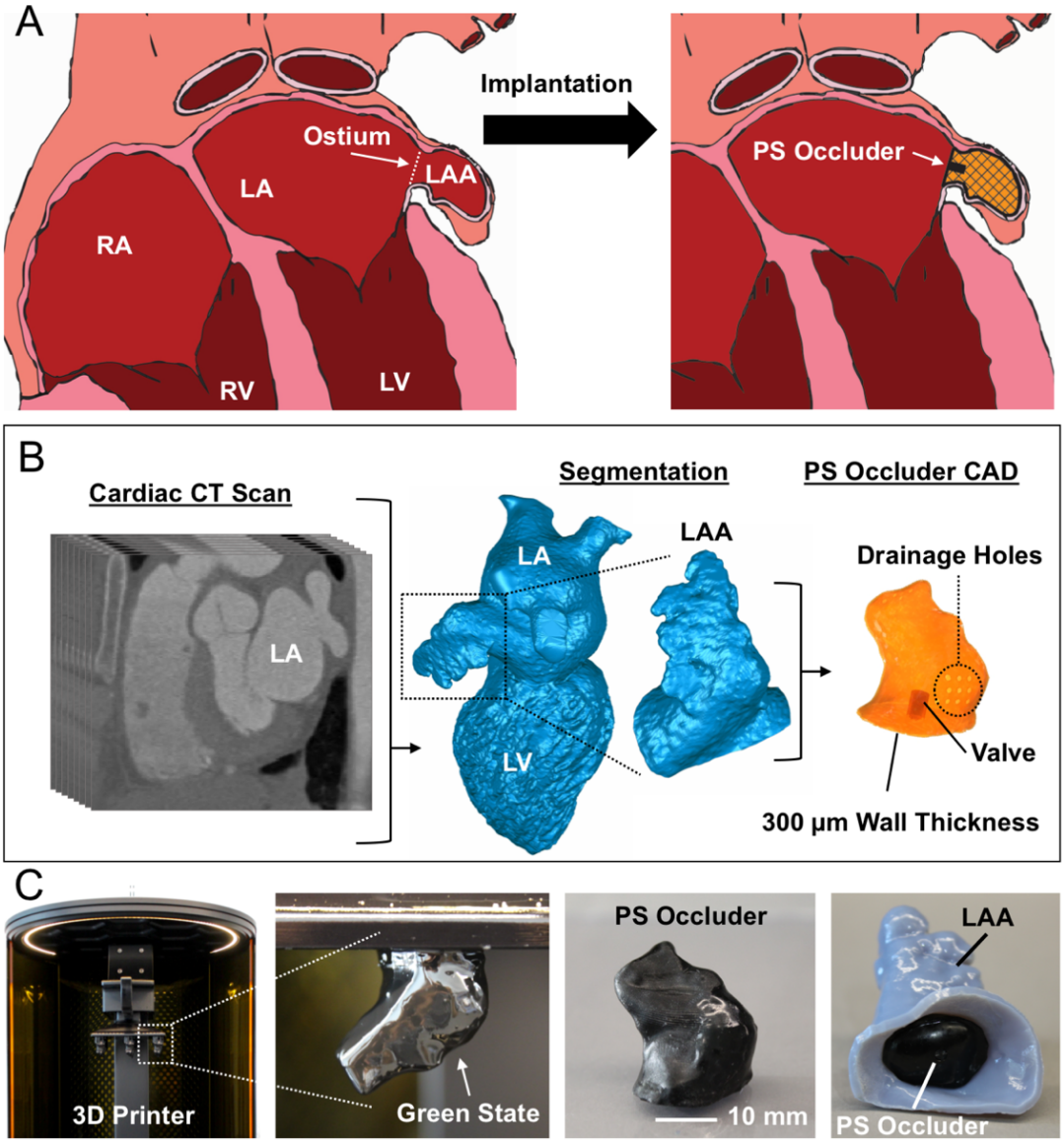

Figure 3.1| Direct 3D printing of patient-specific (PS) left atrial appendage (LAA) occluder. (a) Schematic of heart with right atrium (RA), right ventricle (RV), left atrium (LA), and left ventricle (LV) labeled. The ostium is the opening between the LA and LAA. PS occluder is implanted into the LAA and conforms to the surrounding tissue. (b) CT Segmentation of left heart blood volume, isolation of LAA, CAD design of PS hollow occluder with 300 µm wall thickness, 3 mm diameter valve, and drainage holes for venting during printing. (c) 3D printing of PS occluder. Freshly printed part is in delicate *green state*. Final printed PS occluder after cleaning and full cure. PS occluder implanted into 3D printed LAA.

3.2 Design of patient-specific occluders for 3D printing

We used non-invasive, human cardiac CT scans to guide the design of patient-specific (PS) occluders, a method thoroughly described previously by Robinson et al. [Robinson et al., *Nat. Biomed. Eng.* 2017] (Fig. 3.1b). Briefly, we used open-source software (ITK-Snap, University of Pennsylvania) to perform semi-automatic image segmentation on the left heart blood volume from human CT scans. We used additional image processing software (Geomagic Wrap, 3D Systems) to isolate the LAA, then smoothed the surface and shelled the object for 3D printing a hollow structure with a wall thickness of 300 μm. To prepare the design for direct printing, we used SOLIDWORKS (Dassault Systems) to (i) add a valve to the ostial surface of the occluder, and (ii) insert drainage holes to reduce vacuum forces that occur during SLA printing of hollow structures (Fig. 3.1b).

3.3 Fabrication of patient-specific occluders

We used a high-resolution SLA printer (M1, Carbon, Inc.) and a commercial elastomeric polyurethane (EPU, Carbon) resin to directly print custom LAA occluder designs (Fig. 3.1c). Using our 141 mm x 79 mm build stage, 10 - 15 occluders can be printed at once, greatly increasing the fabrication speed over previous methods. After photopolymerization, the "*green bodies*" are fragile and covered in liquid resin (Fig. 3.1c). We used isopropyl alcohol to gently clean resin off both the external and internal surfaces. The drainage holes that allowed for venting of the hollow prints aid in the removal of encapsulated, unreacted resin inside the occluders. Applying a thin layer of fresh resin over these holes, followed by exposure under a UV light source (ECE 5000, Dymax Inc.) sealed the green body. A post-processing thermal treatment (120°C for 8 hr) fully cured the EPU material to obtain the full elastomeric properties (Fig. 3.1c, 3.2a). Lastly, we injected silicone pre-polymer (Ecoflex 00-30, Smooth-On) into the

cavity of the valve where it interlocks and cures with printed crossbars to create a self-sealing valve (Fig. 3.2a). By iterating this design-fabrication process with patient-specific (PS; i.e. Chicken Wing) and spherical morphologies, we empirically determined the minimum wall thickness (t = 318.6 ± 49 μm) compatible with our printing process (Fig. 3.2b). Replica molding pathways for similar elastomeric occlusion devices could only achieve thickness with large dimensional variance, t = 500 ± 125 μm. The final printed PS occluder, when compressed, fits into an 18 Fr Catheter (d = 6 mm) for surgical intervention (Fig. 3.2c).

Our material choice also imparts important mechanical performance to the printed devices. Compared to other available SLA materials, EPU is an excellent candidate owing to its large elastic strain regime ($\gamma_{elastic}$ > 300%; Fig. 3.2a) and high tear strength (Γ_{tear} = 23 ± 3 kN m^{-1}). Combined, these properties lead to a robust, highly deformable device even when dimensions are miniaturized. Despite having a 40% thinner wall, these devices operate safely at pressures and volumes (ΔP > 60 kPa, ΔV > 50 mL; Fig. 3.2c, S3.4) that exceed the corresponding failure regimes of their replica molded silicone counterparts (ΔP_{burst} ~ 30 kPa, ΔV_{burst} ~ 40 mL) [Robinson et al., *Nat. Biomed. Eng.* 2017].

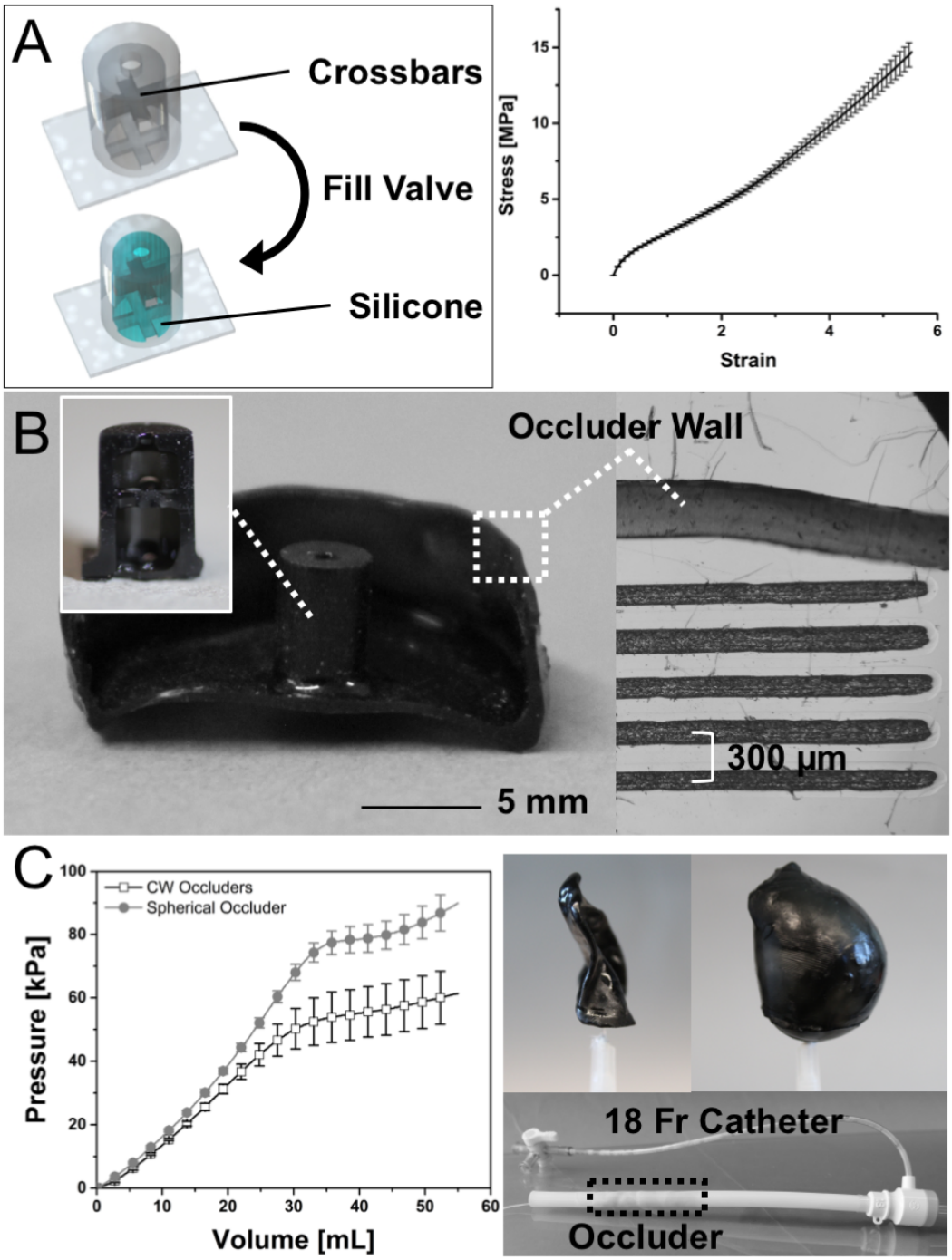

Figure 3.2| Features of 3D printed, patient-specific occluders. (a) Schematic of printed valve before and after filling with silicone. The printed crossbars (black) lock the added silicone (blue) in position so no covalent bonding is necessary (left). The uniaxial tensile behavior of elastomeric polyurethane (EPU; n = 11, mean ± s.d.). (b) Cross-section of occluder with cross-section of valve inset. Right, optical microscope

image of cross section of occluder wall next to reticle for measuring wall thickness, $t \sim 318.6 \pm 49$ μm ($n = 9$, mean ± s.d. from 3 occluders). (c) Comparison of PS and spherical occluders pressure-volume behavior (left, $n = 7$, mean ± s.d.). Right top, image of PS occluder evacuated and inflated to very large volumes using air ($\Delta P > 50$ kPa) Right bottom, potential delivery method, PS occluder within an 18 Fr catheter (outlined by dotted line).

3.4 Stable anchoring and resistance to embolism

Another concern with implanted occluders is the possibility of device embolization into the left atrium. To probe the long-term viability of our printed geometries, we conducted *in vitro* pull-out tests at different device inflation volumes, $V_{inflation} = (V_{injected}/V_{rest})*100$ (Fig. 3.3a). We 3D printed a custom attachment for the bottom grip of our tensile tester (Zwick & Roell, z010) that replicates the Chicken Wing LAA anatomy (Fig. 3.3b, S3.5). We implanted either a patient-specific (PS) or spherical occluder (r_{rest} = 8.75 mm) into the LAA. After implantation, we pulled on the ostial surface of the occluder until it popped out of the simulated appendage (Fig. 3.3b, S3.5). We report the maximum force during separation as a function of inflation volume (Fig. 3.3a, Table 3.1). These forces dramatically exceed those required to dislodge the Watchman and Amulet occlusion devices ($F_{pull\text{-}out} \sim 3.5$ N), which make use of nitinol hooks to pierce the tissue for anchoring. For the PS morphology, we estimated a minimum occlusion volume of $V_{inflation} \sim 200\%$ (see supplemental information for details) which corresponds to a pull-out force of approximately $F_{pull\text{-}out} \sim 14.9 \pm 1.47$ N. Increasing the volume of both the PS and spherical occluders logically increases the pull-out forces, but likely impinges upon the adjacent anatomy. In particular, the spherical samples with large inflation volumes ($V_{inflation} > 150\%$) visibly deformed the simulated LAA, which is consistent with our observations that non-PS geometries have the potential to strain and damage LAA and neighboring tissues while attempting to fully occlude the ostium.

Whereas the pull-out measurements were made on a static appendage, the *in vivo* atrial environment is dynamic. The oscillating pressures within the heart, coupled with the expansion and contraction of the atria may contribute to device embolism at forces below the above measured thresholds. Here, we simulated the LAA anatomy using a silicone phantom attached to an idealized left atrium flow loop (Fig. 3.3c, S3.6). After implanting our printed device, we controlled the operation of two pumps at pulsatile flow ($f \sim 1$ Hz) and pressure regimes ($\Delta P \sim 15$ kPA) that approximated the systolic and diastolic behavior of the left heart ($\Delta P \sim 16$ kPA; Fig. 3.3c). Table 1 notes any embolism event or damage to the LAA phantom during subsequent continuous operation for 48 hours. We found that both PS and spherical occluders embolized when they were underinflated, $V_{inflation} \sim 50\%$ (Fig. S3.7). We also observed that over-inflation ($V_{inflation} > 200\%$) of spherical occluders tore the silicone LAA within the first 24 hours (Fig. S3.8).

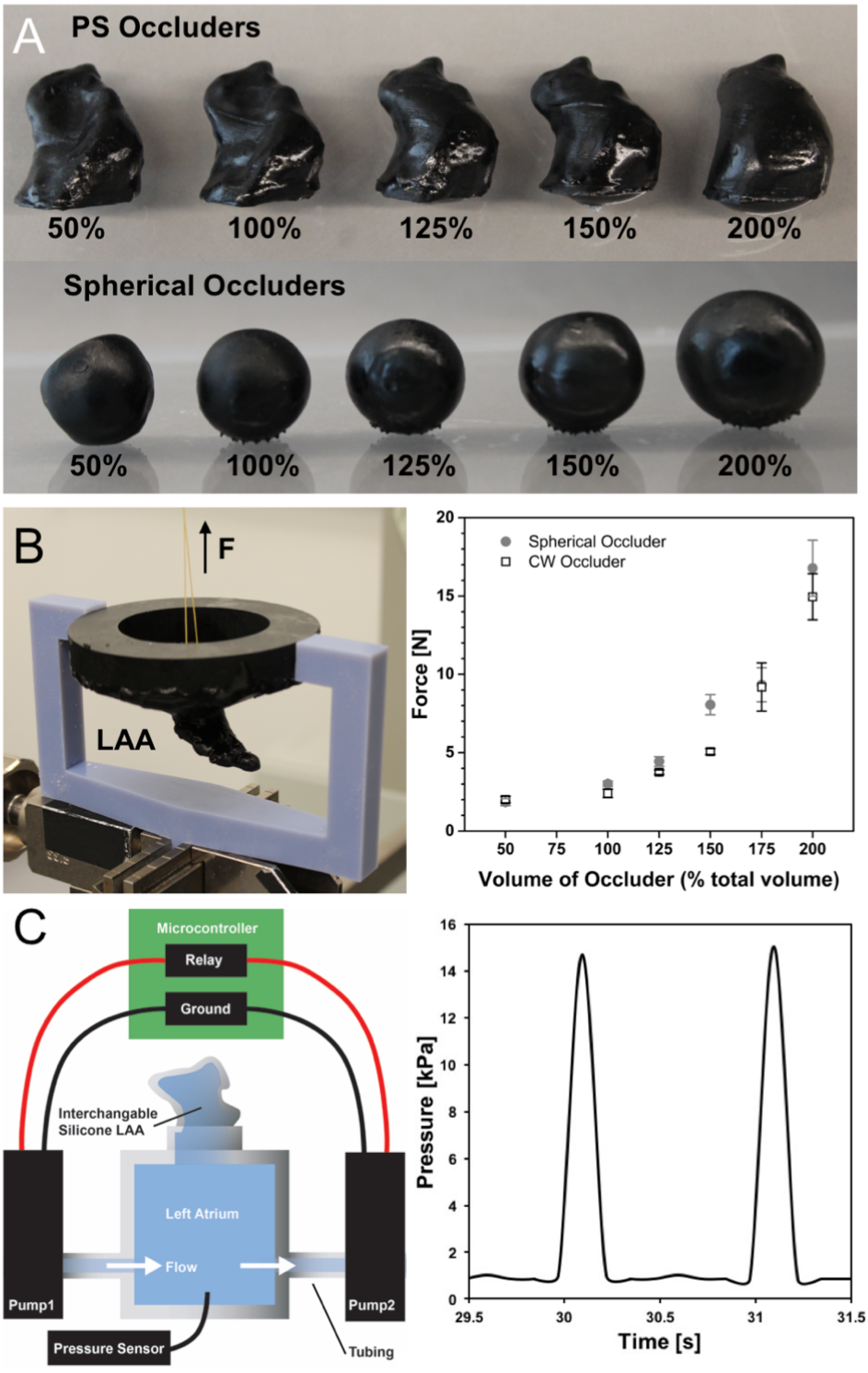

Figure 3.3| Pull-out and embolism performance of patient-specific (PS) vs spherical occluders. (a) PS and spherical occluders filled with Ecoflex 00-30 up to $V_{inflation}$ ~ 200%. (b) 3D printed pull-out test jig attached to Zwick tensile tester (left). Force

needed to pull occluder out of LAA when inflated by increasing amounts (n = 5, mean ± s.d.). (c) Schematic of embolism test set-up. PS or spherical occluder was implanted into the silicone LAA for 48 hours to see if occluder would embolize (left). Physiological pressure drops $\Delta P \sim 15$ kPa and frequencies ($f \sim 1$ Hz) were maintained throughout the 48 hours.

Table 3.1| Embolism and pull-out test results for occluders of various inflation volumes. (n = 5, mean ± s.d.)

$V_{inflation}$	***50%***	***100%***	***125%***	***150%***	***200%***
Embolism Test Results					
PS	Embolized	Stable	Stable	Stable	Stable
Spherical	Embolized	Stable	Stable	Stable	Tore LAA
Pull-out Test Results [N]					
PS	2.0±0.22	2.4±0.27	3.8±0.14	5.0±0.19	14.9±1.47
Spherical	1.9±0.22	3.0±0.17	4.4±0.30	8.0±0.64	16.8±1.78

3.5 Hemodynamic flow analysis of atrial-facing geometry

Current mechanical closure devices available are round in shape, while the ostium of most LAAs is elliptical. This mismatch in geometry causes large crevices to form on either side of implanted occluders, this can lead to residual flow of blood into the LAA and to clots forming on or around the device. To ensure stable anchoring and to mitigate this residual flow, these round devices are typically oversized by 8-20%[31]. While this practice helps eliminate blood flowing into the appendage, it does not diminish – and may worsen – the severity of the crevices between the occluder and the atrial wall. The ability of our printed LAA to change volume in a "balloon-like" manner is a key differentiator compared to existing LAA occluders, and allows them to conform to the LAA anatomy. The atrial-facing geometry of our occluders was designed from the CT scans to exactly match the existing anatomy.

We used computational flow dynamics (CFD) to analyze the atrial-facing geometry of patient-specific and spherical occluders (Fig. 3.4). We used SolidWorks™ to assemble either a PS or spherical occluder into the appendage of a Chicken Wing LAA morphology. After creating a solid body and mesh we then performed the flow analysis. We overlaid the heatmap results from the wall shear stress of both the PS and spherical geometries over their left heart models (Fig. 3.4b-c). We observed that the regions along the edges of the spherical occluder had very low wall shear stress regimes (Fig. 3.4c). Previous studies have correlated low wall shear stress regimes with clot formation. These areas of low wall shear stress were not as pronounced in the PS design (Fig. 3.4b). We believe this is because the PS design is better matching the internal atrial wall.

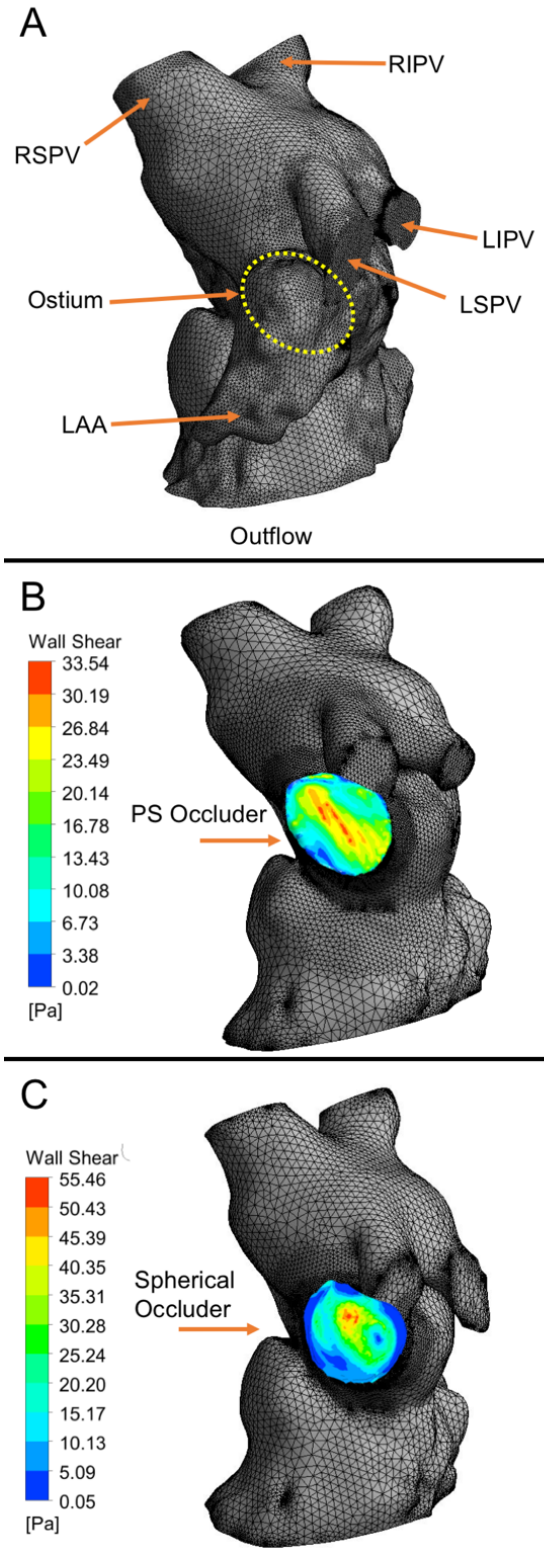

Figure 3.4| Computational hemodynamics of the atrium facing wall of a PS or spherical occluder. (a) Fluid domains discretization with 441,162 tetrahedron

elements. Right superior pulmonary vein (RSPV), right inferior pulmonary vein (RIPV), left superior pulmonary vein (LSPV), and left inferior pulmonary vein (LIPV) are the inflow regions. The ostium is not visible from this surface view, but its position on the interior surface has been outlined using a yellow dotted line. The Chicken Wing morphology LAA has also been highlighted. The outflow region is the left ventricle, it has been cropped out. (b) Model of left heart with patient-specific (PS) occluder within the LAA, it has 472,741 tetrahedron elements. The wall shear stress heatmap of the atrial wall of the occluder has been overlaid on the model. (c) Model of left heart with spherical occluder within the LAA, it has 408,667 tetrahedron elements. The wall shear stress heatmap of the atrial wall of the occluder has been overlaid on the model. Note the areas of dark blue on the outer edges. These are located where crevices have formed between the occluder and the atrial wall.

3.6 Conclusion

We developed a strategy for quickly and accurately producing patient-specific left atrial appendage occluders for patients with atrial fibrillation who have a high risk of stroke. These occluders are directly printed using elastomeric polyurethane and function as inflatable balloons that can conform to the patients' anatomy at inflation volumes $V_{inflation}$ ~ 200%. While previous manufacturing strategies are too laborious for practical implementation [Robinson et al., *Nat. Biomed. Eng.* 2017], we can fabricate 10-15 patient-specific devices in under 12 hours for under $3.00 per device by using stereolithographic 3D printing. Our hollow devices simultaneously possess thin walls (t ~ 318.6 ± 49 μm) that enable surgical implantation and robust mechanical properties (ΔP_{burst} > 60 kPa, ΔV_{burst} > 50 mL). Our work demonstrates a facile method for quick and scalable production of personalized cardiovascular implants. Additionally, our methods could be more broadly applied to other areas of medicine, where soft materials and patient-specificity are needed.

Using CT segmentation and methods described in our previous publication [Robinson et al., *Nat. Biomed. Eng.* 2017] we achieved patient-specific designs that met the resolution and capabilities of our 3D printer. We added a silicone valve to enable rapid inflation and deflation of these thin walled elastomeric balloons. We demonstrate the stable anchoring of these occluders within a simulated appendage by measuring the pull-out force, and testing the long-term implantation of the occluder. We found that the pull-out force needed to dislodge a fully inflated PS occluder was $F_{pull\text{-}out} \sim 14.9 \pm 1.47$ N, and that only underinflated occluders ($V_{inflation} \sim 50\%$) were not stable over long periods of time in our bench-top flow loop. We used CFD to investigate the wall shear stress of the atrial surface of a spherical vs a patient-specific occluder. We found that the spherical occluder tended to have regions of very low wall shear stress around the edges of the device where crevices formed between the device and the atrial wall. These low shear regions could be areas where clots start to form around the spherical device, this was not observed in the PS device. We did not investigate hemocompatibility of our base EPU material. Previous work, however, demonstrates a straightforward process to sterilize and impart hemocompatibility onto complex polymeric 3D surfaces without drastically affecting final shape or wall thickness [Robinson et al., *Nat. Biomed. Eng.* 2017].

In its current form this occluder can fit into a d = 6mm catheter (18 Fr), this is too large for a percutaneous delivery and therefore would need to be delivered surgically. Future work should address decreasing its form factor in order to fit it into a d = 4 mm catheter (12 Fr). A potential route to achieve this goal, while maintaining the current limitation of minimum $t \sim 300$ μm wall thickness, would be to introduce pleating. These pleats would enable us to more easily compress the device into small catheters. Additionally, by re-designing the valve into a flap we could also decrease the evacuated size. We noticed that the regions of high curvature tended to collect extra resin after the device was printed, by smoothing these occluders in the design process we could mitigate the resin collection in these regions and have more uniform wall thicknesses. Future work should also include hemocompatibility, and long term

durability testing in order to assess how well these occluders would perform *in vivo* where biological interactions can be unpredictable.

As the resolution, capabilities, and library of materials increases for 3D printers, they are becoming increasingly useful to the medical community. Currently, medical printing is used mostly for education and surgical planning[28,32-34], there are a few examples of using it to fabricate patient-specific devices. We are not aware of any previous work that uses 3D printing to directly fabricate a soft, patient-specific endocardial device. Previous work by our groups demonstrated a design and manufacturing process for soft, patient-specific LAA occluders, however these were manually fabricated and took at least 3 days to create an occluder for a single patient. Here we demonstrated improvement over our previous process by fabricating thin walled personalized endocardial implants in under 12 hours using fast, scalable SLA printing.

3.7 Experimental

3.7.1 Uniaxial tensile tests

We performed tensile tests according to ISO 37 on a Zwick Roell z010 instrument. All tests were conducted at room temperatures using a 10 kN load cell and a strain rate of 200 mm min^{-1}. The data were averaged across common strain range and plotted with standard deviation (n = 11). We chose to skip every 25 points to make data more visible.

3.7.2 Thickness variation

We took three specimens from three different occluders, for a total of nine samples. We used a razor blade to slice portions of the printed occluder in a variety of areas. We then used an optical microscope (Zeiss) to image these samples against a reticle of known dimensions (Fig. 3.2b, right). This reticle was fabricated by etching lines with set dimensions into acrylic using a laser cutter (Epilog Zing 50W, Epilog Laser). The

images were processed using ImageJ by measuring each specimen in three positions. We calculated the mean and standard deviation using Microsoft Excel (Excel for Mac, Version 15.32, 2017).

3.7.3 Pressure – volume tests

All Pressure-Volume data in this manuscript was collected using custom LabVIEW™ code (Code can be made available upon request, National Instruments). The code controlled the input volume through a programmable syringe pump (NE-1000, New Era Pump Systems Inc.) and recorded the output pressure data from a pressure transducer (0-100 PSI, TDH30-CG-0100-03-D004, Transducers direct). These tests were performed on fourteen occluders (7 patient-specific, 7 spherical geometries). Each sample was inflated and deflated five times. To avoid non-linear effects in the stress-strain behavior of the base polymer, we only used the fifth recording to determine the mean and standard deviation between the samples (Fig. 3.2c).

3.7.4 Pull-Out Tests

To characterize the pull-out force required to remove our devices from the LAA, we designed and 3D-printed a custom testing set-up which could be attached to a Zwick Roell z010 tensile tester (Fig. 3.3b). We used elastomeric polyurethane (M1 Carbon, EPU) to fabricate an anatomically correct LAA and secure this to one end of a rigid adapter (Objet30 Scholar Stratasys, Veroblue) which connects to the load cell of the tensile tester. We then inflated six PS occluders (with a Chicken Wing morphology that corresponded to the LAA in the testing rig) and six spherical occluders to six different volumes ($V_{inflation}$ ~ 50% to 200%). We backfilled the occluders with an RTV-silicone pre-polymer (Ecoflex 00-30, Smooth-on) blended with 10 wt% silicone thinner (Smooth-on) which allowed for easier injection. After the silicone fully cured, we threaded a loop of Kevlar through the ostial surface of the occluder (Fig. S3.5). We properly positioned and oriented the occluder within the simulated LAA and secured the Kevlar string to the moving head of tensile tester. Next, we pulled the occluder back

out of the LAA at a rate of 25 mm min^{-1} while recording the tensile force (n = 5). We report the maximum tensile force applied to the occluder during this pull-out test.

3.7.5 Embolism Tests

A custom benchtop flow-loop determined if the PS or spherical occluders would embolize during the first 48 hours of implantation (Fig. 3.3c, S3.6). This setup was modified from one described in our previous publication [Robinson et al., *Nat. Biomed. Eng.* 2017]. Briefly, we attached a sealed, 3D printed idealized left atrium to two pumps (ZKWP03A, FORTRIC), a patient-specific silicone LAA, and a pressure transducer (0-15 PSI, TDH30-CG-0015-03-D004, Transducers direct; Fig. S3.6). A relay switch alternatively operates these pumps at physiological rates (f ~ 1 Hz). An external reservoir feeds and collects water from these pumps. By placing this reservoir at a height ~15 inches below the flow loop, we produce a pressure of ΔP ~ 15 kPa inside of the chamber. We then implanted our occluder into the simulated LAA and took pressure readings at 0, 24, and 48 hours to ensure we maintained the desired physiological pressure range.

3.7.6 Statistical analyses

Sample size, mean, and standard deviation are reported for all data sets. No statistical methods were used to pre-determine the sample-sizes for the characterization of the performance of the occluders. All statistical analyses were performed in Origin® (Academic Version, 2016) and Microsoft Excel (Excel for Mac, Version 15.32, 2017).

3.7.7 Code availability

The LabVIEW™ and Arduino Uno™ codes that were used in this study can be made available upon request to the corresponding author.

3.7.8 Data availability

The authors declare that all data supporting the findings of this study are available within the paper and its Supplementary Information.

3.7.9 Image acquisition

All photographs in the manuscript were taken with a Canon (EOS Rebel T3i).

3.7.10 Image processing

Except where explicitly stated (i.e. where we state that we changed the contrast), photographs were only cropped and positioned in figures using Adobe® Illustrator® (CS6, Version 16.0.3), Adobe® Photoshop® (CS6, Version 12.0), and PowerPoint (Microsoft Office). SolidWorks® (Education Edition, 2016) renderings were performed using PhotoView 360® Add-In feature. Geomagic Wrap® (Version 2015) renderings were taken using the Snapshot feature. Schematics were created using Adobe® Illustrator®. All arrows, dotted lines, and text were added to images in Adobe® Photoshop® or PowerPoint. All plots were created in Origin® (Academic Version, 2016).

3.7.11 Acknowledgements

This work made use of the Cornell Center for Materials Research Facilities supported by the National Science Foundation under Award Number DMR-1120296. This work was supported by Weill Cornell Medical College Clinical & Translational Science Center (grant no. TL1-TR-002386), the Army Research Office (grant no. W911F-16-1-0095), and the Office of Naval Research (grant no. N00014-17-1-2837).

3.8 Supplementary Information

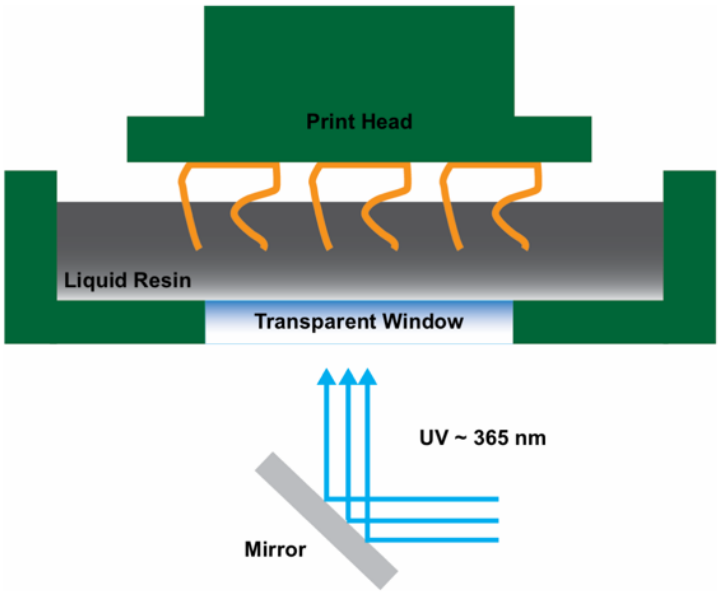

Figure S3.1| Schematic of stereolithography printing process. Printed parts are cured layer by layer after exposure to UV light. Printed parts are pulled out of the liquid resin.

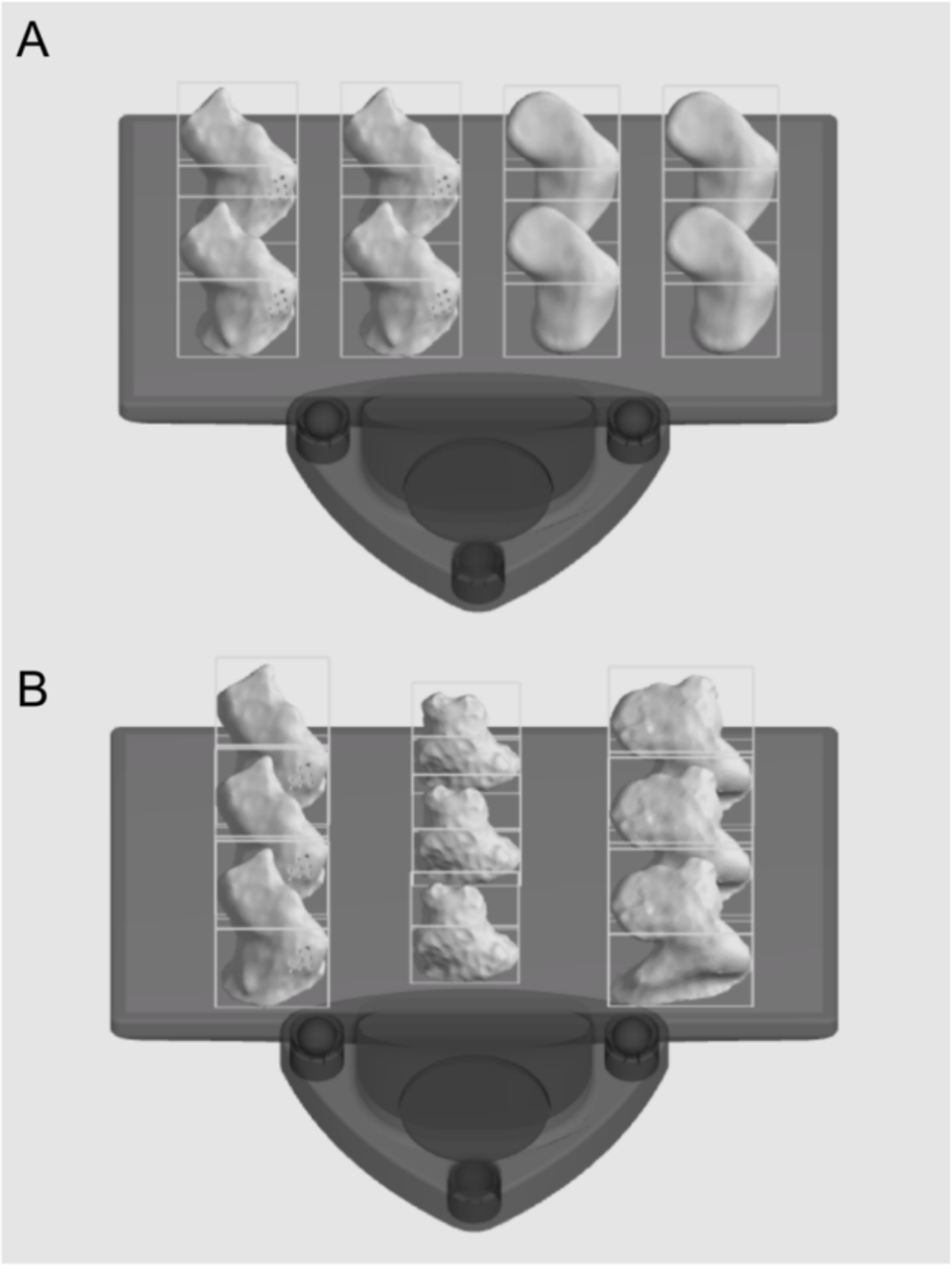

Figure S3.2| Schematic of LAA occluders on print head. (a) Complex features, or smooth parts for the same patient can be printed on a single print. (b) LAA occluders for 3+ different patients can be fabricated on a single print.

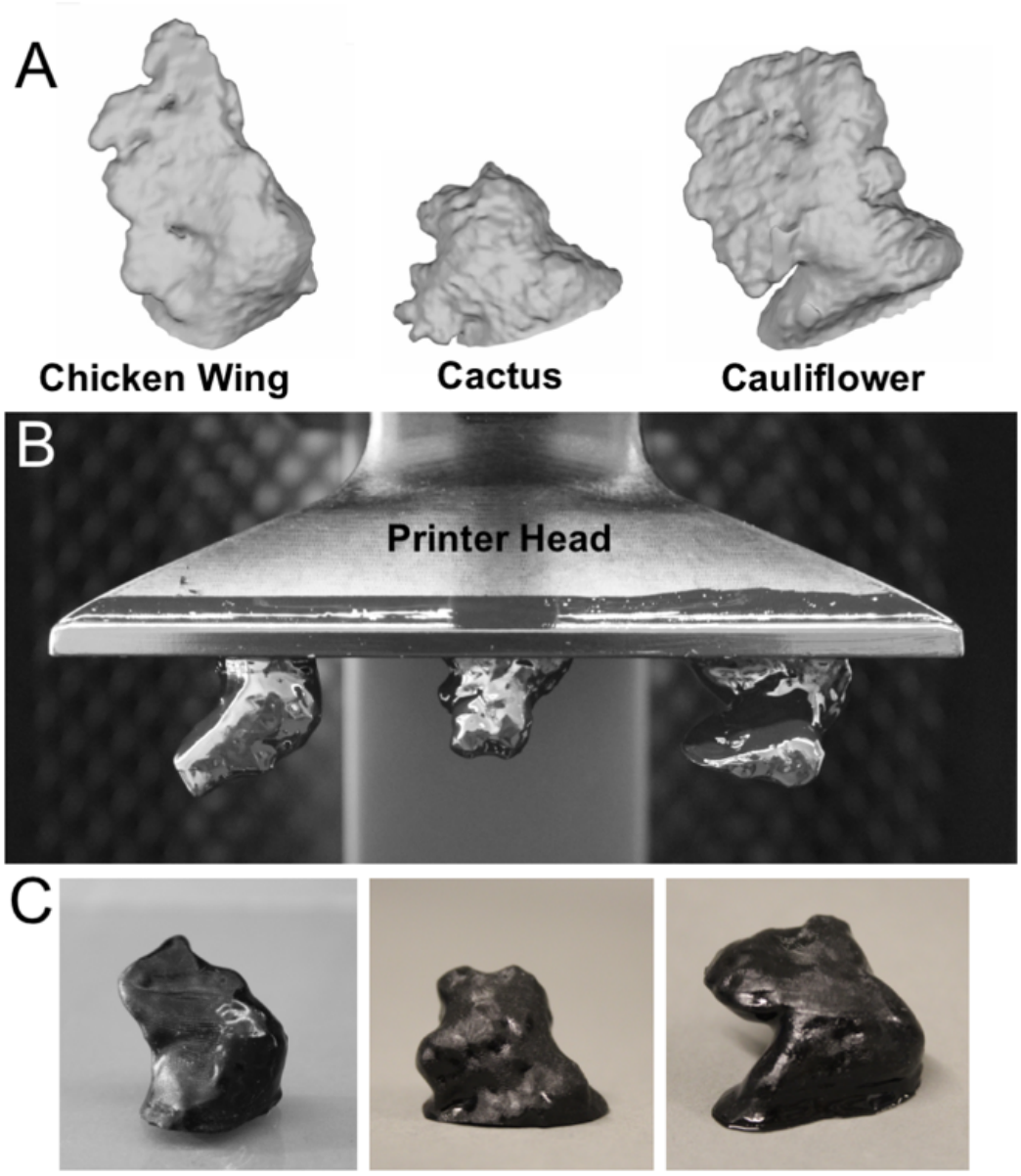

Figure S3.3| Multiple patient-specific occluders can be printed simultaneously. (a) CAD renderings of CT segmented LAA for three typically encountered LAA morphologies, Chicken Wing (CW), Cactus, and Cauliflower. (b) 3D printed morphologies inthe *green state*. (c) Fully cured LAA occluders for three patient morphologies.

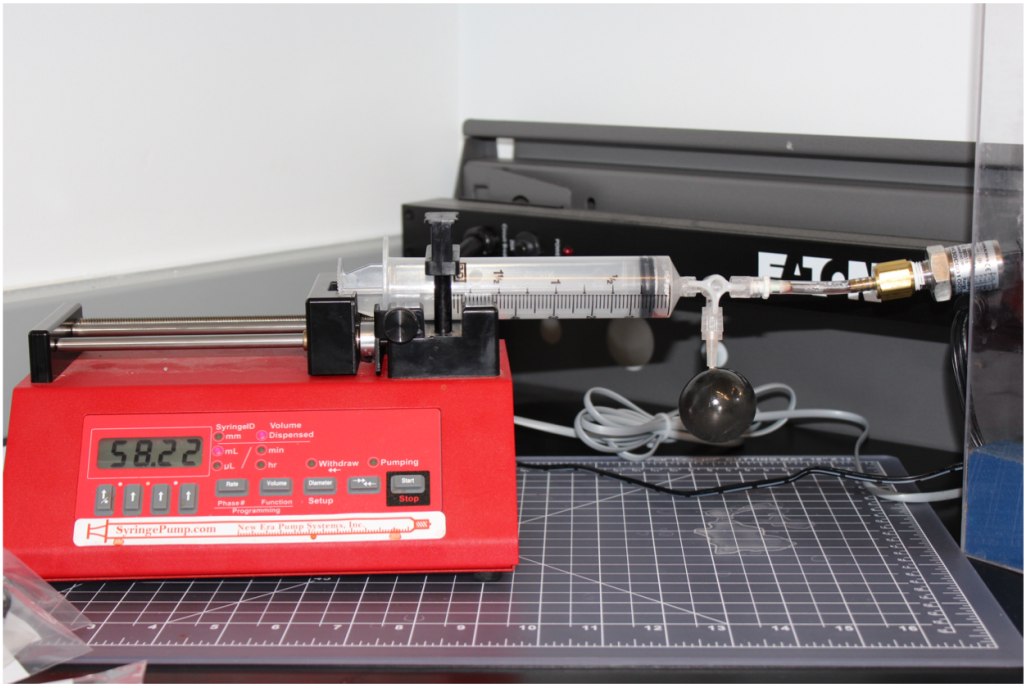

Figure S3.4| Pressure – volume test set-up. Occluders were attached through their plug onto the tip of a 30 gauge needle. They were then inflated with air up to 60 mL (size of syringe) while the volume input and pressure output was being recorded in labview VI. Each sample ($n = 6$) was tested five times and the 5th recording was used to determine the mean pressure and standard deviation of the samples.

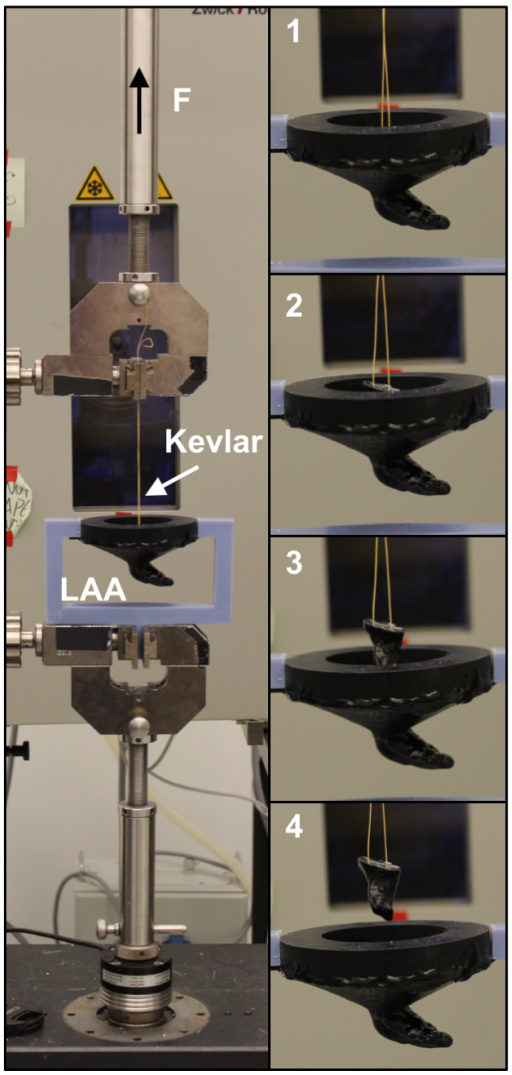

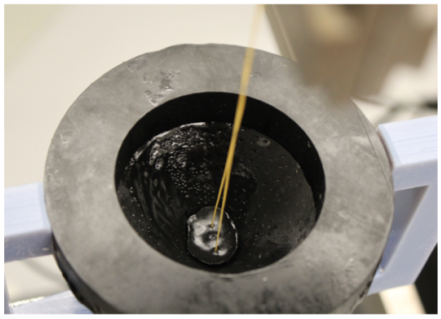

Figure S3.5| Pull-out test. Kevlar thread (yellow) was looped through the ostial surface of the occluders and then attached to the upper crosshead of the tensile tester. The 3D printed LAA test-jig was attached to the bottom grip of the tensile tester. Occluders (which were prefilled with Ecoflex 00-30) were inserted into the LAA and then pulled out. (1-4) Images of the various stages of the test.

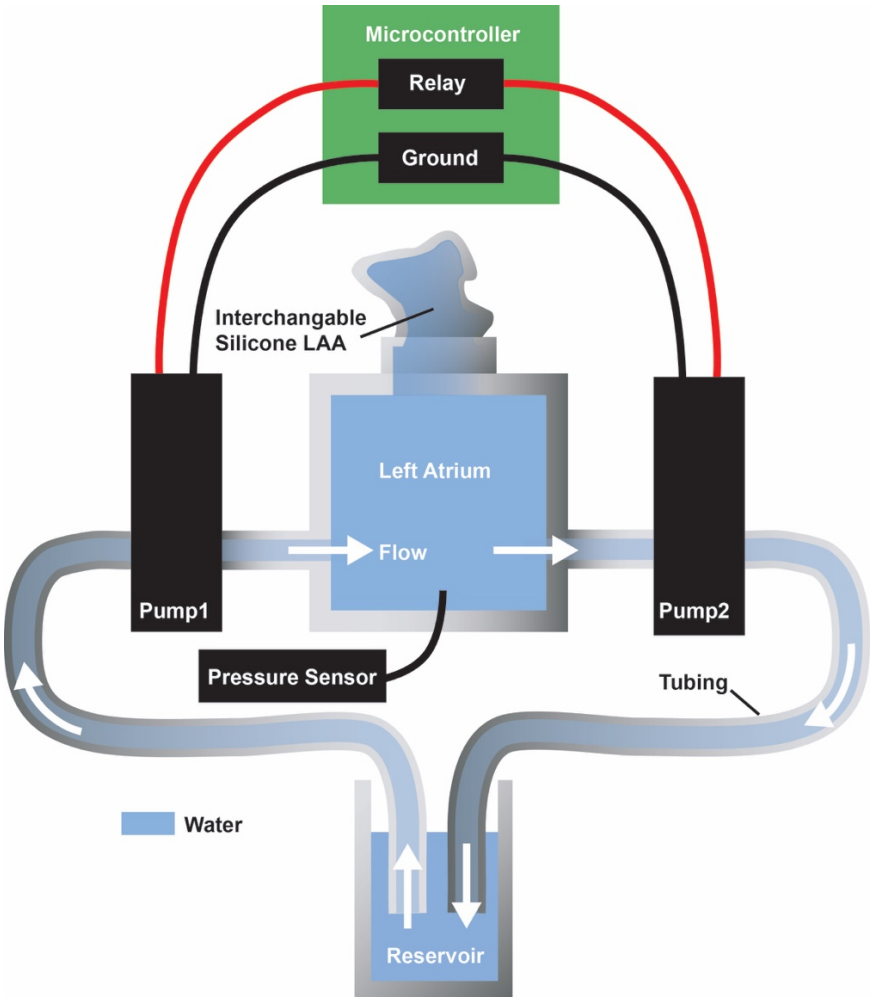

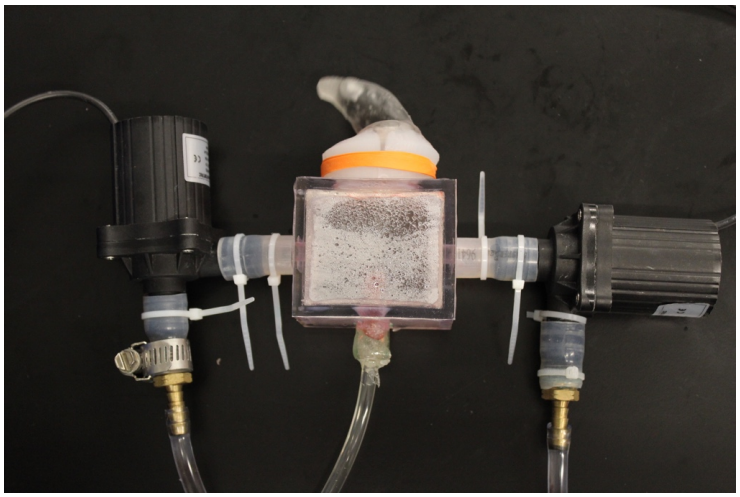

Figure S3.6| Embolism test set-up. Pumping water at physiological frequencies f = 1Hz. Measuring pressure within the idealized left atrium. Reservoir sits ~ 15" below left atrium chamber.

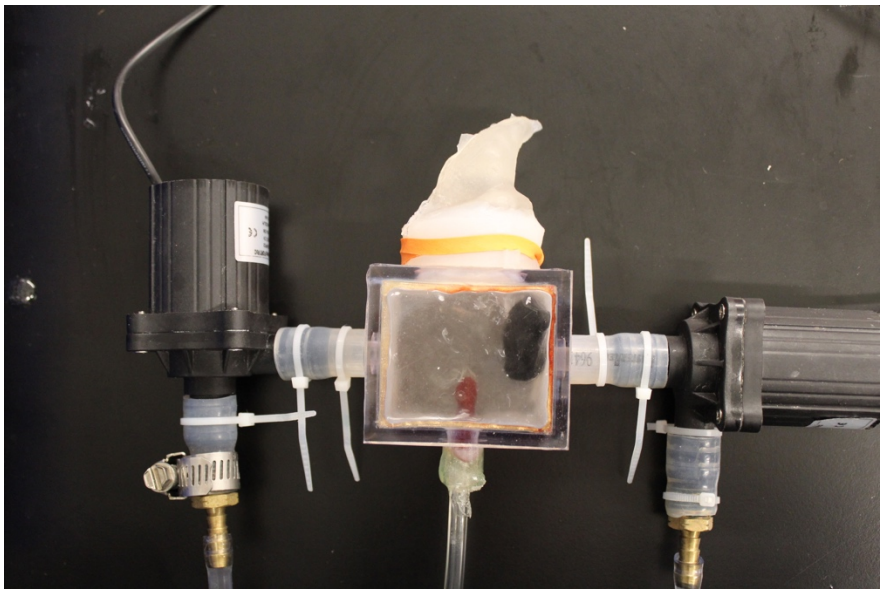

Figure S3.7| PS and spherical occluders embolized when they were underinflated, $V_{inflation}$ ~ 50%. In this image, the PS occluder is visible within the idealized left atrium of the flow set up. This demonstrates embolism of a device.

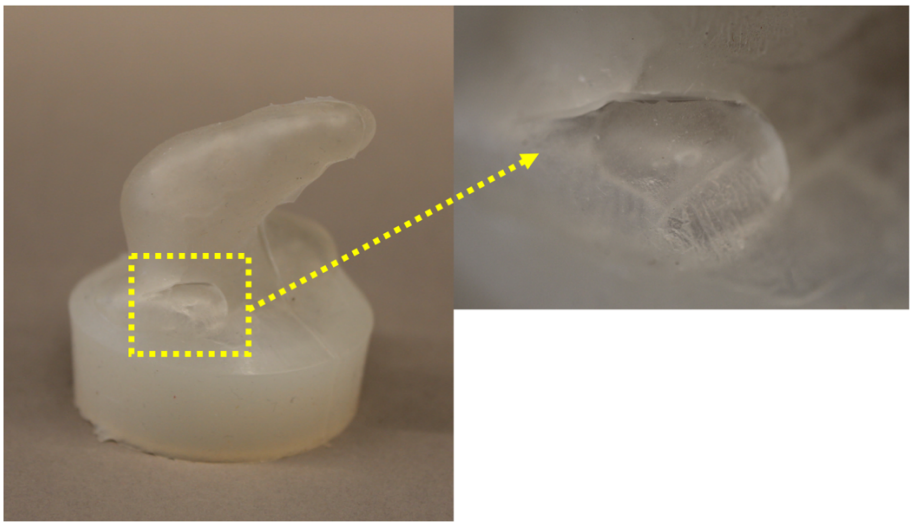

Figure S3.8| Image of hole that was torn in the silicone phantom LAA by the $V_{inflation}$ ~ *200%* spherical occluder during the first 24 hours of testing.

REFERENCES

[1] H. Zhao, Y. Li, A. Elsamadisi, R. Shepherd, *Extreme Mechanics Letters* **2015**, *3*, 89.

[2] T. J. Wallin, J. H. Pikul, S. Bodkhe, B. N. Peele, B. C. Mac Murray, D. Therriault, B. W. McEnerney, R. P. Dillon, E. P. Giannelis, R. F. Shepherd, *J. Mater. Chem. B* **2017**, *5*, 6249.

[3] S. S. Robinson, K. W. O'Brien, H. Zhao, B. N. Peele, C. M. Larson, B. C. Mac Murray, I. M. van Meerbeek, S. N. Dunham, R. F. Shepherd, *Extreme Mechanics Letters* **2015**, *5*, 47.

[4] B. C. Mac Murray, X. An, S. S. Robinson, I. M. van Meerbeek, K. W. O'Brien, H. Zhao, R. F. Shepherd, *Advanced Materials* **2015**, *27*, 6334.

[5] R. J. Morrison, S. J. Hollister, M. F. Niedner, M. G. Mahani, A. H. Park, D. K. Mehta, R. G. Ohye, G. E. Green, *Sci. Transl. Med.* **2015**, *7*, DOI 10.1126/scitranslmed.3010825.

[6] A. Díaz Lantada, R. Del Valle-Fernández, P. Lafont Morgado, J. Muñoz-García, J. L. Muños Sans, J. M. Munoz-Guijosa, J. Echávarri Otero, *Ann Biomed Eng* **2009**, *38*, 280.

[7] S. H. Sündermann, M. Gessat, N. Cesarovic, T. Frauenfelder, P. Biaggi, D. Bettex, V. Falk, S. Jacobs, *Interactive CardioVascular and Thoracic Surgery* **2013**, *16*, 417.

[8] P. S. D'Urso, D. J. Effeney, W. J. Earwaker, T. M. Barker, M. J. Redmond, R. G. Thompson, F. H. Tomlinson, *British Journal of Plastic Surgery* **2000**, *53*, 200.

[9] J. Brie, T. Chartier, C. Chaput, C. Delage, B. Pradeau, F. Caire, M.-P. Boncoeur, J.-J. Moreau, *Journal of Cranio-Maxillofacial Surgery* **2013**, *41*, 403.

[10] N. Xu, F. Wei, X. Liu, L. Jiang, H. Cai, Z. Li, M. Yu, F. Wu, Z. Liu, *SPINE* **2016**, *41*, E50.

[11] R. Schwarzkopf, M. Brodsky, G. A. Garcia, A. H. Gomoll, *Orthopaedic*

Journal of Sports Medicine **2015**, *3*, 232596711559037.

[12] Y. Mao, C. Xu, J. Xu, H. Li, F. Liu, D. Yu, Z. Zhu, *International Orthopaedics (SICOT)* **2015**, *39*, 2023.

[13] R. Akhtar, M. J. Sherratt, J. K. Cruickshank, B. Derby, *Materials Today* **2011**, *14*, 96.

[14] P. Su, K. P. McCarthy, S. Y. Ho, *Heart* **2008**, *94*, 1166.

[15] P. A. Wolf MD, R. D. Abbott, W. B. Kannel MD, *Stroke* **1991**, *22*, 983.

[16] J. L. Blackshear MD, J. A. Odell FRCS(Ed), *Ann Thorac Surg* **1996**, *61*, 755.

[17] S. C. Landefeld MD, R. J. Beyth MD, *The American Journal of Medicine* **1993**, *95*, 315.

[18] C.-M. Yu, A. A. Khattab, S. C. Bertog, A. P. W. Lee, J. S. W. Kwong, H. Sievert, B. Meier, *Nat Rev Cardiol* **2013**, *10*, 707.

[19] J. D. Moss, *Curr Cardiol Rep* **2014**, *16*, 448.

[20] B. Kong, Y. Liu, H. Huang, H. Jiang, C. Huang, *J Thorac Dis* **2015**, *7*, 199.

[21] C.-H. L. MD, J. B. K. M. PhD, S.-H. J. M. PhD, S. J. C. M. PhD, C. H. C. M. PhD, J. W. L. M. PhD, *Ann Thorac Surg* **2014**, *97*, 124.

[22] E. S. Katz, T. Tsiamtsiouris, R. M. Applebaum, A. Schwartzbard, P. A. Tunick, I. Kronzon, *JACC* **2000**, *36*, 468.

[23] A. S. Kanderian, A. M. Gillinov, G. B. Pettersson, E. Blackstone, A. L. Klein, *JACC* **2008**, *52*, 924.

[24] J. O'Brien, D. Al-hassan, J. Ng, M. Joshi, C. Hague, S. Chakrabarti, J. Leipsic, *Int J Cardiovasc Imaging* **2014**, *30*, 819.

[25] J. F. Viles-Gonzalez MD, S. Kar MD, P. Douglas MD, S. Dukkipati MD, T. Feldman MD, R. Horton MD, D. Holmes MD, V. Y. Reddy MD, *JACC* **2012**, *59*, 923.

[26] D. B. Kolesky, K. A. Homan, **2016**.

[27] B. Mosadegh, G. Xiong, S. Dunham, J. K. Min, *Biomed Mater* **2015**, *10*, 034002.

[28] S. Anwar MD, G. K. Singh MD, J. Varughese, H. Nguyen MD, J. J. Billadello MD, E. F. Sheybani MD, P. K. Woodard MD, P. Manning MD, P. Eghtesady

MD, *JACC: Cardiovascular Imaging* **2016**, 1.

[29] J. Odent, T. J. Wallin, W. Pan, K. Kruemplestaedter, R. F. Shepherd, E. P. Giannelis, *Advanced Functional Materials* **2017**, *27*, 1701807.

[30] D. K. Patel, A. H. Sakhaei, M. Layani, B. Zhang, Q. Ge, S. Magdassi, *Advanced Materials* **2017**, *29*, 1606000.

[31] A. Akinapelli, O. Bansal, J. P. Chen, A. Pflugfelder, N. Gordon, K. Stein, B. Huibregtse, D. Hou, *Current Cardiology Reviews* **2015**, *11*, 334.

[32] M. Vukicevic, B. Mosadegh, J. K. Min MD, S. H. Little MD, *JACC: Cadiovascular Imaging* **2017**, *10*, 171.

[33] L. Lao, S. S. Robinson, B. Peele, H. Zhao, B. C. Mac Murray, J. K. Min, B. Mosadegh, S. Dunham, R. F. Shepherd, *Adv. Eng. Mater.* **2016**, *19*, 1600591.

[34] A. A. Giannopoulos MD, D. Mitsouras, S.-J. Yoo, P. P. Liu, Y. S. Chatzizisis, F. J. Rybicki, *Nat Rev Cardiol* **2016**, *13*, 701.

CHAPTER 4

INTEGRATED SOFT SENSORS AND ELASTOMERIC ACTUATORS FOR TACTILE MACHINES WITH KINESTHETIC SENSE

Sanlin S. Robinson, Kevin W. O'Brien, Huichan Zhao, Bryan N. Peele, Chris M. Larson, Benjamin C. Mac Murray, Ilse M. van Meerbeek, Simon N. Dunham, Robert F. Shepherd, *Extreme Mechanics Letters*, 5, 47-53. **(2015)**

Cover Art

4.2 Introduction

Human development, intelligence, and survival are intimately linked to tactile (i.e. touch and pressure) and kinesthetic (i.e. position and movement) feedback we receive from millions of mechanoreceptors embedded in our skin.[1,2] These highly specialized receptors are capable of transmitting signals through ionically conducting nerve fibers at rates of up to 70 m s^{-1}.[2] When these sensors are deformed mechanically—perhaps by compression of the skin or contraction of a muscle—an action potential is transmitted along afferent pathways then processed in the central nervous system.[2] An appropriate response to the input stimulus is then returned along efferent neuronal pathways.[2] This sensory-motor coupling allows us to effortlessly perceive and interact with our environment, enabling the performance of complex tasks such as avoiding furniture in the dark or playing the piano. Due to skin's significant role in learning, tool manipulation, and gross motor coordination, the development of a synthetic analogue will enable new methods of feedback control in robotics, medical monitoring, and human-machine interfaces. Wearable[3] and implantable electronics[4] have been developed to integrate with human tissue, which is soft, three-dimensional, and mechanically dynamic.

Along with the development of stretchable electronics, the field of soft robotics has been gaining traction as a result of their ability to (i) interact gently with biological organisms,[5,6] (ii) easily conform to their surroundings,[7-9] and (iii) achieve complex motions using simple modes of actuation.[10-13] These robots are typically composed of hyperelastic materials (e.g. silicones) with large ultimate strains, Υ_{ult} ~400-700%, that have embedded networks of pneumatic channels (PneuNets). These pneumatic actuators are powered through inflation, similar to a balloon. A critical limitation of soft robots is the availability of compliant and extensible sensors[14] that can (i) reliably detect external stimuli and internal actuation, (ii) be easily integrated with current manufacturing processes, (iii) function at the high strains encountered throughout actuation, and (iv) tolerate many actuation cycles without delamination.

To address these sensing deficiencies many groups have developed flexible and stretchable sensors that use changes in resistance,[15-17] capacitance,[18,19] light,[20] or resonant frequency[21,22] to detect deformation. Specifically, for soft robots that undergo large deformations, shape sensing is a critical need for feedback control (communicating with a central computer to ensure a machine task is being completed accurately). Therefore, we focus on sensing techniques using stretchable capacitors due to their high precision and sensitivity over large ranges of strain and pressure.[23,24]

Here we present a highly extensible sensing skin that we integrated with soft, pneumatic actuators via a 3D printing technique called direct ink writing (DIW; Fig. 4.1). This skin enables soft machines to sense external stimuli as well as their own shape, thus creating a device that has both tactile and kinesthetic sense. Central to our approach is the development of two viscoelastic fluids—one that is ionically conductive (hydrogel elastomer precursor) and another that is electrically insulating (silicone elastomer precursor). We directly patterned these inks by extruding them in alternating layers through micronozzles of two different diameters, d_{hydr}=330 μm and d_{sil}=250 μm, on our custom dual-head 3D printer. The two inks are yield-stress fluids that flow through our print heads at high shear rates and retain their shape after exiting the nozzles due to their viscoelastic properties. After extrusion, we used in-situ photopolymerization of the inks to chemically crosslink them into conductive hydrogels and insulating silicones with large ultimate strains, γ_{sil}^{ult} > 350% and γ_{hydr}^{ult} > 300% (Fig. 4.2, S4.2). When patterned into alternating conductive and dielectric layers, these composite skins behave as stretchable capacitors, capable of transducing low mechanical stresses and large strains into electrical signals. We printed these stretchable capacitors onto soft, Pneumatically-powered Haptic Displays (PHD; Fig. 4.1, S4.1) to provide sensory feedback control. We characterized the ability of the PHD to (i) detect touch (tactile sense), (ii) detect its own actuation (kinesthetic sense), and (iii) integrate these two senses for sensory-motor coupling.

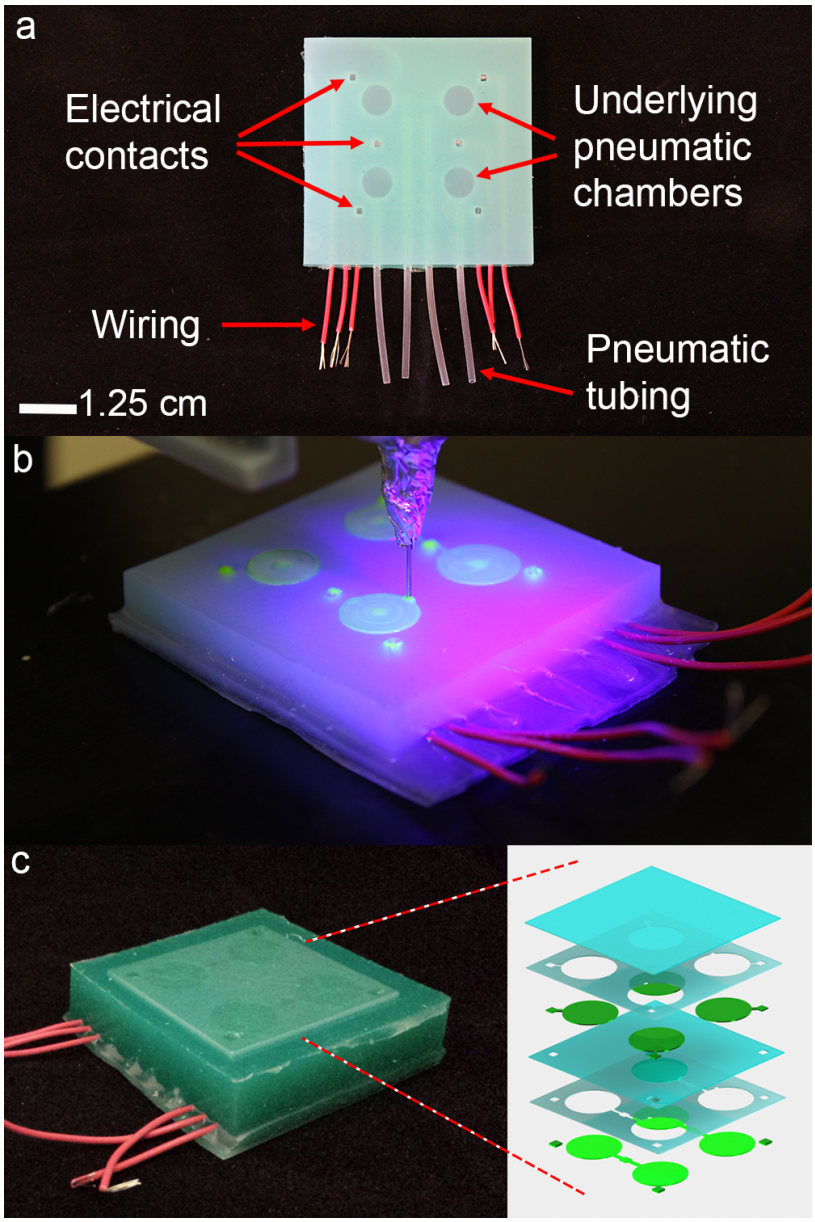

Figure 4.1| Overall device schematic. (a) Image of pneumatic haptic display with wells where electrical contacts will be formed, underlying pneumatic chambers, tubing and electrical wiring. **(b)** Image of printing stretchable sensors onto pneumatic haptic display. **(c)** Fully printed sensor on surface of pneumatic haptic display; **(inset)** Schematic of printed layers of conductive polyacrylamide (green) and insulating silicone (blue).

4.3 Ink Preparation

We chose to use DIW because it offers material flexibility, rapid design iteration, low cost,[25-27] and facile integration with previously established soft robot fabrication methods (i.e. replica molding[8] and rotational casting[9]). In addition, the rheological properties of many polymeric inks can be modified to enable this printing technique.[28-30] Specifically, both the shear thinning and yield stress properties of these complex fluids can be adjusted so the inks flow smoothly out of micronozzles and retain their shape after being printed. The shear thinning exponent (n), storage (G') and loss (G'') moduli are primarily controlled by the high molecular weight polymer constituents.[30] To tailor the rheology of the silicone elastomer precursor, we prepared blends of high and low molecular weight silicones (60 wt% Nuvasil® Loctite 5039, 40 wt% Wacker ® Semicosil 912) together into a homogenous melt (details in supplemental information, SI). In this system, the high molecular weight polymer serves to adjust the yield stress, while the low molecular weight one polymerizes into a resilient matrix. We chose silicones because they have very high electrical resistivity (on the order of 10^{13} Ω·m), low leakage currents,[31] high strain to failure, and high resilience.[18,32]

We chose hydrogels because they can be made highly conductive, transparent, biocompatible, and stretchable.[18,33] We formulated the hydrogel elastomer precursor analogously to the silicone by combining high molecular weight polyacrylamide (PAAM 5-6 million M_w; 92560, Sigma Aldrich) and acrylamide monomer (AAM; Sigma Aldrich) in deionized water and ethylene glycol (EG; Sigma Aldrich). We also used N,N'-methylenebisacrylamide (MBA; Sigma Aldrich) as the crosslinking agent and Darocur® 1173 (BASF) as the photoinitiator, ionic liquid (IL; 1-decyl-3-methylimidazolium chloride, Sigma Aldrich) served as the conductive medium. As the hydrogel is optically transparent, we used fluorescently labeled monomer (FOA; Fluorescein O-acrylate, Sigma Aldrich) for visualization of the ink during printing. We found that using 14 wt% AAM, 5.6 wt% PAAM, 0.22 wt% MBA, 0.14 wt% Darocur® 1173, 3.4 wt% IL, 0.1 wt% FOA, 56.2 wt% EG, and 20.3 wt% DI water resulted in the desired rheological and mechanical properties.

4.4 PHD Fabrication

We fabricated silicone actuators using soft lithography as this process is simple and allows for rapid design iteration (details in SI). We then printed stretchable capacitors onto these pneumatic actuators as the skin of our PHD (Fig. 4.1, S4.1). First, we placed and leveled the prefabricated actuators on the bed of the 3D printer, then loaded the silicone and hydrogel inks into two separate syringes. By alternating layers of polyacrylamide and silicone inks we created planar arrays of capacitive sensors. The inks were exposed to high intensity UV radiation throughout the printing process. Once the capacitive skin was fully printed, no post exposure to UV light was necessary. We chose to overlay these sensors onto the actuators as an intuitive user interface to physically program the PHD; in addition, they enable us to detect the degree of actuation of individual chambers. Alternatively, if kinesthetic sensing is not needed, we can print the sensors anywhere, not necessarily on top of the actuators.

4.5 Materials Characterization

To be compatible with our pressure inputs (ΔP_{sil} ~ 270 kPa and ΔP_{hydr} ~ 70 kPa) we tuned our materials to have viscosities less than 50 Pa·s at the shear rates for which we were printing (Fig. 4.2a). Both inks displayed pronounced shear thinning above a critical shear rate of ~0.1 s^{-1}. This behavior indicates that above these shear rates, the entangled, long-chained polymers are aligning under the applied shear stress and will start to flow smoothly through micronozzles. Using Equation 4.1, we estimated the shear rate experienced by the ink at the nozzle walls during extrusion[34]:

$$\dot{\gamma}_{wall} = \left(\frac{3+b}{4}\right)\frac{4Q}{\pi R^3} \tag{4.1}$$

where b is the inverse of the shear thinning exponent, $Q = \boldsymbol{v\pi R^2}$ is the volumetric flow rate, $v \sim 4$ mm·s^{-1} is the print speed, and R is the nozzle radius. We determined the shear thinning exponent from our measured viscometry data to be $\boldsymbol{n_{hydr}} = 0.287$ and $\boldsymbol{n_{sil}} = 0.496$. We calculated the shear rate experienced by these fluids at the nozzle to be $\dot{\boldsymbol{\gamma}}_{\boldsymbol{wall}}^{\boldsymbol{hydr}} \sim 157$ s^{-1} and $\dot{\boldsymbol{\gamma}}_{\boldsymbol{wall}}^{\boldsymbol{sil}} \sim 160$ s^{-1}. At these shear rates, the ink viscosities are $\boldsymbol{\eta_{hydr}} \sim 7$ Pa·s and $\boldsymbol{\eta_{sil}} \sim 17$ Pa·s. Ink elasticity is an important rheological parameter that can indicate whether ink will retain its printed shape before crosslinking. To determine the elasticity of these inks, we measured the shear elastic modulus (G′) and viscous modulus (G″) at a frequency of 1Hz (Fig. 4.2b). The polyacrylamide ink has a plateau elastic modulus of $\boldsymbol{G_{hydr}^0} \sim 350$ Pa and a yield stress of $\boldsymbol{\sigma_y^{hydr}} \sim 539$ Pa, while the silicone ink has $\boldsymbol{G_{sil}^0} \sim 2250$ Pa and a $\boldsymbol{\sigma_y^{sil}} \sim 22$ Pa. We found that both inks display a solid-like response (G′ > G″) at low shear stresses, which enables shape retention after extrusion and before being cured under UV illumination.

The skin of the PHD must withstand large strains, yet deform at low stresses. As the mechanical properties of the skin are dominated by the silicone, we measured its tensile properties (Fig. 4.2c; details in SI). We also compared our printed material's mechanical properties to that of cast silicone (Fig. 4.2c). At 100% strain, the printed and cast silicones have elastic moduli of $\boldsymbol{E_{print}} \sim 73$ kPa and $\boldsymbol{E_{cast}} \sim 109$ kPa, respectively. The lower elastic modulus of the printed silicone may indicate that the high molecular weight polymer remains in a prestretched state due to shear alignment from extrusion.

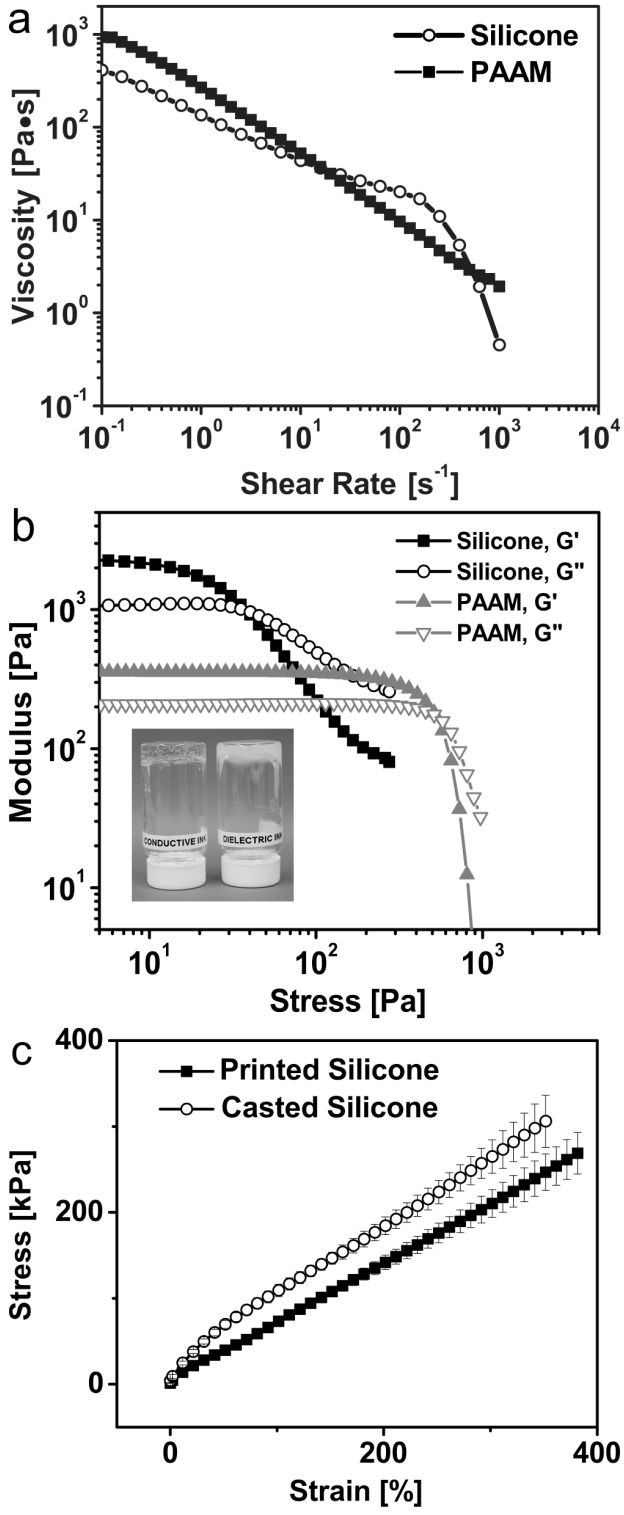

Figure 4.2| Material characterization. (a) Viscometry and **(b)** oscillatory rheology data for insulating silicone and conducting polyacrylamide (PAAM) inks; **(inset)**

upturned vials of each ink demonstrate their elasticity. **(c)** Tensile data of 3D printed and cast silicone samples.

4.6 Sensor Characterization

Upon internal pressurization, the PHD's chambers expand in area causing the surface to dome; commensurately, the sensor area overlaying the chamber also increases while its thickness decreases, resulting in a change in capacitance, ΔC. We recorded the ΔC using an LCR meter (Agilent 4284) while actuating a single chamber (Fig. 4.3a, left) using a fixed volume syringe pump in series with a pressure gauge. Here we show that this behavior is consistent with that of a continuously deforming circular parallel plate capacitor (i.e., $C \sim Ad^{-1}$, where A and d represent the electrode area and dielectric thickness, respectively). We first model the relationship between internal chamber pressure and the strain state of the sensor, and then reconcile that result with the expected change in capacitance as the sensor is stretched C(λ).

To model P(λ), we employ three assumptions: (i) the membrane behaves linear elastically (Fig. 4.2c) with an elastic modulus, E, (ii) the undeformed sensor is a circle and upon actuation deforms into a spherical cap with a radius of curvature r, and deflection h, and (iii) the elastomeric membrane is incompressible giving rise to principle stretches of $\lambda_1 = \lambda_2 = \lambda$, $\lambda_3 = \lambda^{-2}$, and principal stresses of $\sigma_1 = \sigma_2 = \sigma, \sigma_3 = 0$. We first balance the forces from the internal pressure (P) acting on the membrane with the induced reaction forces within it.

$$P \cdot (\pi {r_0}^2) = T \cdot sin\theta \tag{4.2}$$

$$T = \sigma \cdot (2\pi r_0) \cdot t$$

$$sin\theta = \frac{r_0}{r}$$

Where r_0 is the radius of the undeformed sensor, T is the stretching force, t is the nominal thickness of the membrane (see Fig. S4.6). The pressure can therefore be expressed as follows:

$$P = \frac{2\sigma \cdot t}{r} \tag{4.3}$$

Given assumptions 4.2 & 4.3 we can relate λ to r, t, and t_0 as follows:

$$\frac{A}{A_0} = \frac{2\pi rh}{\pi r_0^2} = \lambda^2 \qquad and \qquad \frac{t}{t_0} = \lambda^{-2} \tag{4.4}$$

We now invoke a geometrical argument that relates r to r_0 and h, both of which are measurable quantities.

$$r^2 = {r_0}^2 + (r - h)^2 \tag{4.5}$$

Combining Equations (4.2)-(4.5) with Hooke's law, $\sigma = E(\lambda - 1)$, yields the following relation:

$$P(\lambda) = \frac{4t_0 E(\lambda - 1)(\lambda^2 - 1)^{1/2}}{r_0 \lambda^4} \tag{4.6}$$

The circular capacitive sensor is designed such that the in the fully actuated state (i.e., a hemisphere), it covers the underlying chamber completely. The nominal radius of the sensor, r_{C0}, is thus larger than r_0. To model the change in capacitance as accurately as possible, therefore, we bifurcate the capacitance equation into two parts – the first models the outer region that is bounded by r_{C0} and r_0 (C_0), and the center portion bounded by r_0 (C_1). Our equation for capacitance is:

$$C = C_0 + C_1 \tag{4.7}$$

$$where \quad C_0 = \varepsilon_r \varepsilon_0 \frac{\pi({r_{C0}}^2 - {r_0}^2)}{t_{C0}} \tag{4.8}$$

$$and \quad C_1 = \varepsilon_r \varepsilon_0 \frac{2\pi r h}{t_C} = \varepsilon_r \varepsilon_0 \pi \frac{{r_0}^2}{t_{C0}} \lambda^4 \tag{4.9}$$

Combining relations in Equation 4.7 yields the relationship between λ and C:

$$\lambda = \left(\frac{C - C_0}{\varepsilon_r \varepsilon_0 \pi \frac{{r_0}^2}{t_{C0}}} \right)^{1/4} \tag{4.10}$$

Finally, we substitute $\lambda(C)$ in Equation 4.10 into Equation 4.6 to derive C(*P*). We solve for C(*P*) numerically in MATLAB to obtain the plot shown in Fig. 4.3a, left. Table 4.1 lists the parameters used in the model. We observe that the predicted relationship between C and *P* is in general agreement with the measured values, confirming that our deformable capacitor follow C ~ A/d behavior. The slight deviation between the predicted and measured values at pressures > 25 kPa indicates that our bifurcation scheme could be further refined.

Table 4.1. Model Parameters

P	λ	σ	r	t	h	r_0	t_0	E
Internal pressure	Stretch	Stress	Radius	Thickness	Height	Chamber radius	Initial thickness	Young's modulus

C	r_{C0}	t_C	t_{C0}	ε_r	ε_0
Capacitance	Initial Sensor radius	Sensor thickness	Initial sensor thickness	Relative permittivity	Dielectric constant

r_0	t_0	E	r_{C0}	t_{C0}	ε_r	ε_0
4.0 mm	3.7 mm	68.9 kPa	6.0 mm	0.33 mm	2.2	$8.854\times10^{-12}\,\mathrm{F\cdot m^{-1}}$

Next, we demonstrated the ability of the PHD to transduce external touch into an electrical signal by repeatedly pressing on a single sensor cell 99 times (Fig. 4.3a, right, S4.3). The average force delivered during the press of a sensor cell is approximately 2 N (SI text), this force causes a detectable $\Delta\mathbf{C} \sim 1$ pF. As our goal was not to precisely measure the force a finger applies but to demonstrate the sensitivity to touch of the PHD, we used our own fingers instead of a machine; consequently, there is variation in the measured capacitance between the peaks.

Additionally, using a pressurized air dispensing system, we actuated a single chamber of our pneumatic display while measuring the change in capacitance (Fig. 4.3b, 4.3c). We applied incremental pressures of air to the chamber, we then released the pressure and allowed it to deflate and repeated this cycle (Fig. 4.3c). We only tested up to 38 kPa, above that pressure we start to observe deformation of the hydrogel electrode layers. No discernable capacitance change was observed until at least $\Delta P \sim 10$ kPa was delivered to the chamber (Fig. 4.3b, 4.3c inset). Since we were inflating and deflating manually, the time for each actuation varied, thus the peak widths vary. The shapes of the peaks continue to evolve after initial pressurization due to the viscoelastic nature of the materials.

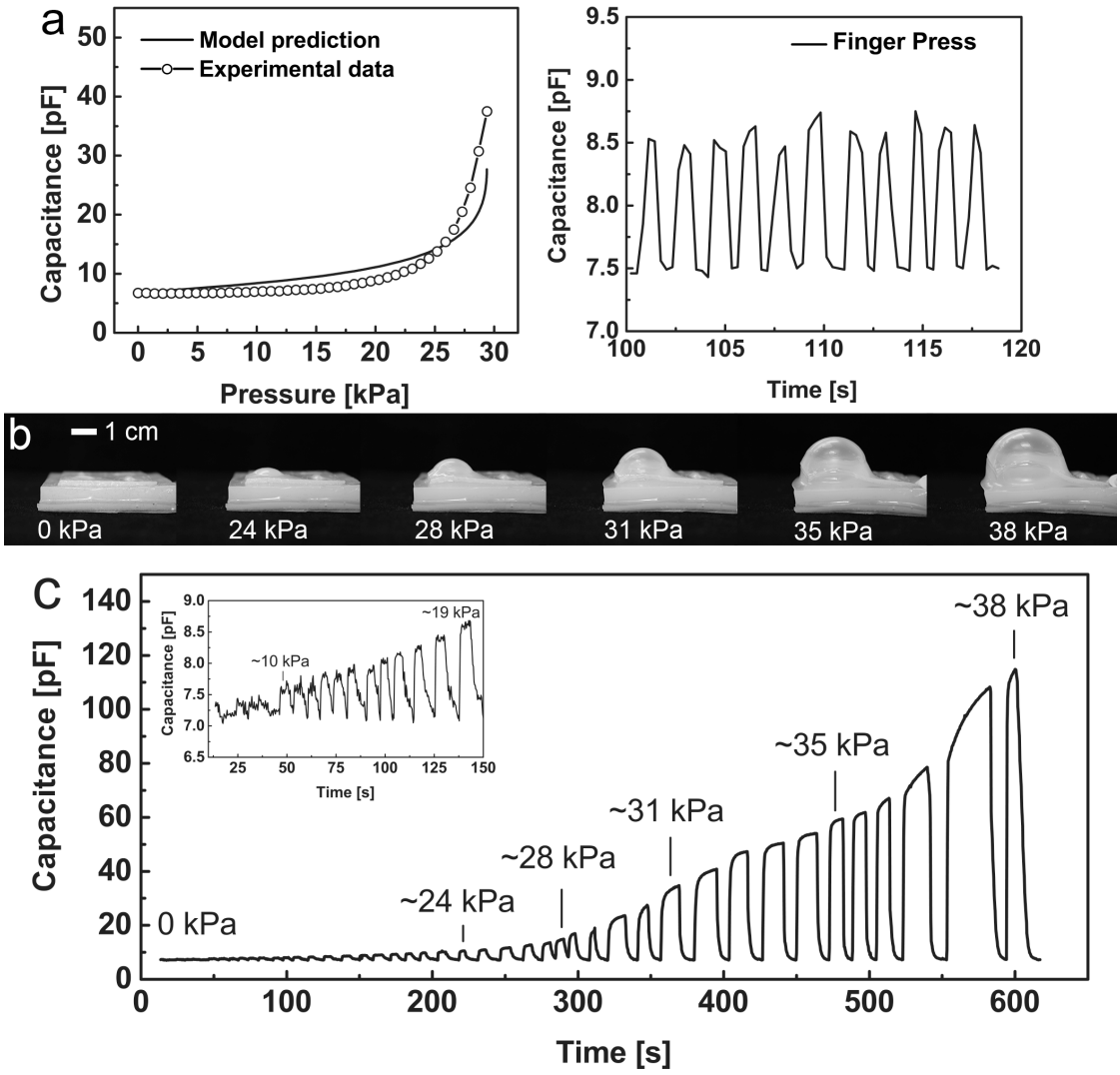

Figure 4.3| Sensor characterization. (a) Left, the measured (circles) and theoretical (line) capacitance as a function of inflation pressure. **Right**, repeatability of capacitor to sense stimulus when pressed by a finger. **(b)** Left to right, images of actuation at different applied pressures. **(c)** Capacitance dependence on inflation and deflation of actuator at increasing pressures; **(inset)** lower capacitance range magnified.

4.7 PHD Device Demonstration

To demonstrate our printed sensor array's ability to encode and read haptic information, we programmed a five-digit sequence into the PHD (SI text). We pressed on the individual capacitive buttons in an arbitrary sequence, sending a signal to an off-board microcontroller's memory (Arduino Mega 2560). The microcontroller then played back the recorded sequence through pneumatic actuation of the individual chambers (Fig. 4.4; supplemental video, SV1). We numbered the sensors one through four, and then punched in the code 2-4-3-2-1 (Fig. 4.4a). The PHD then individually inflated each underlying chamber associated with the sensor input (Fig. 4.4b). The PHD detected the **ΔC** of both the input stimulus (tactile sense) and output actuation (kinesthetic sense; Fig. 4.4c). We note that the peaks from the input are sharp and output are broad due to the duration of the different events.

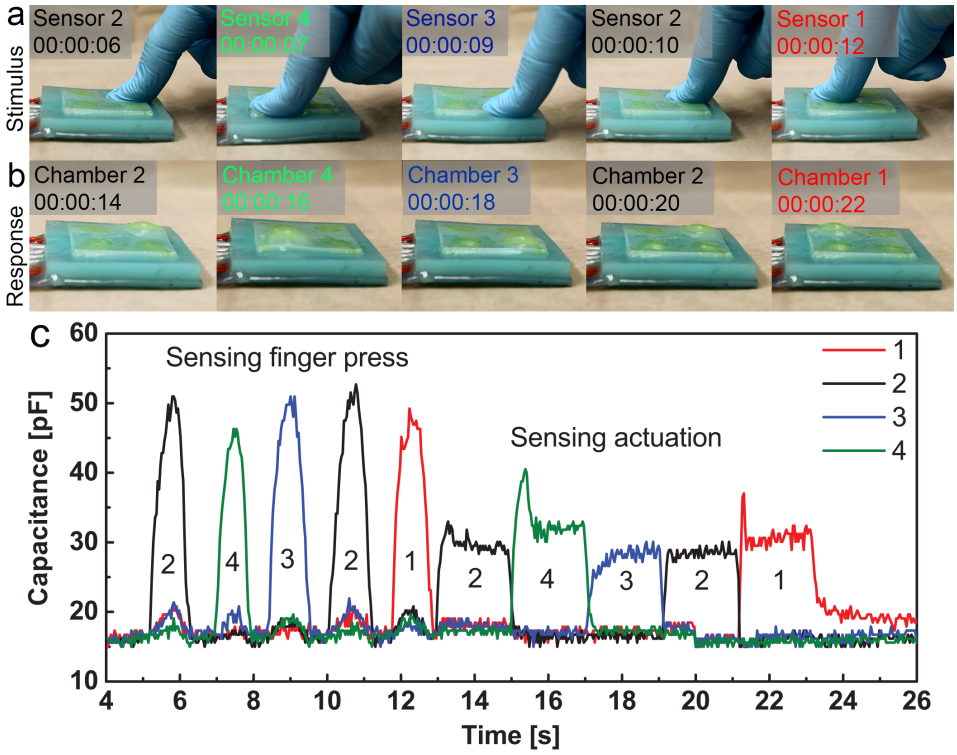

Figure 4.4. PHD device demonstration. (a) Left to right, digital images of inputting a code (2-4-3-2-1) using finger to push on the sensor. **(b)** Left to right, pneumatic haptic

display playing back the same code (2-4-3-2-1). **(c)** Capacitance change of sensor as the code is being input, and then played back through pneumatic actuation. Please see SV1 for video of programming and display sequence.

4.8 Conclusion

In summary, we have developed an inexpensive, hyperelastic, and printable skin for the sensory-motor coupling of soft machines. By tuning the rheological properties of elastomer precursors we formulated viscoelastic inks, which we patterned directly onto the actuators of our PHD. This capacitive skin enabled the PHD to detect a compressive force of ~ 2 N, and an internal pressurization of as low as ~ 10 kPa. As far as we know this is the first demonstration of a completely soft, feedback controlled haptic interface. As the majority of the mating surface between the skin and actuators is silicone, the device exhibited excellent adhesion and no delamination occurred even when high pressures (up to ~ 65.5 kPa) were applied to the actuating chambers. At these pressures, however, the inextensible sealing layer delaminated from the bottom of the PHD; this issue is general to PneuNets operated at high pressure.

While the hydrogels used here have some amount of solvent and are thus somewhat sensitive to environmental conditions, solvent-free systems, such as the polyacrylic acid ones recently demonstrated,[35] could be used to mitigate this issue. While this is a 2D array of capacitors, 3D systems are possible with more complicated CAD design. It is also possible to miniaturize these capacitors by increasing the dielectric constant of the insulating material through the addition of fillers and the use of smaller nozzle diameters for decreased layer thickness. With these two steps we can more accurately replicate the natural ability of biological skin to localize touch sensations. The reliable, low cost, and flexible design space using DIW of tactile and kinesthetic sensors will improve robotic technologies—which are normally confined to perform repetitive tasks in structured environments (i.e. mobile industry)—by allowing humans to work more closely with machines in applications such as search and rescue and domestic care. This same sensor

technology could also improve the quality of life for amputees by enabling intuitive use and automatic adjustment of prosthetic devices.

4.9 Supplemental Information

4.9.1 Material System

The silicone ink was formed by mixing and degassing 60 wt% Nuvasil® Loctite 5039 and 40 wt% Wacker ® Semicosil 912 in a Thinky ARM-310 at 2000 rpm for 120s. The UV catalyst (Wacker ® Elastosil CAT UV) for Semicosil 912 was added at a 1:10 ratio prior to mixing. Due to the secondary moisture cure of Loctite 5039, this ink was used immediately.

The polyacrylamide ink was formed by first mixing deionized water, ethylene glycol and acrylamide monomer (AAM) at room temperature. These constituents were magnetically stirred until the AAM was fully dissolved; at that point we slowly added polyacrylamide to the solution. After the solution was homogeneous, we added N,N'-methylenebisacrylamide, Darocure® 1173 photoinitiator, 1-decyl-3-methylimidazolium chloride ionic liquid, and Fluorescein O-acrylate.

All chemicals were used as received.

4.9.2 Rheological, Mechanical, and Electrical Measurements

Oscillatory rheometry was performed on both ink solutions using a cone (25mm, 2º) and plate geometry at a frequency of 1 Hz and an oscillatory stress from 0 to 900 Pa to determine the elastic modulus (G′), loss modulus (G″), and yield stress (σ_y) of the printable ink. Viscometry was performed on both inks as well, from shear rates of 0 to

10^3 s^{-1}. All data were taken using cone and plate geometry with ~0.5 ml of material on a TA Instruments Discovery Hybrid Rheometer DHR3 rotational shear rheometer.

We performed uniaxial tensile tests on a Z010 Zwick Roell using a 20 N load cell at a strain rate of 3.33 mm/s. We tested at least six repetitive samples of both printed and cast silicone. After printing and casting large rectangular geometries of silicone elastomer precursor, we used a razor blade to cut out six straight, rectangular test samples with approximate dimensions of 40x7x0.6mm.

We measured the electrical performance of the ionic liquid containing hydrogel using a Cascade CP06 Four Point Probe with four in-line probe tips and a Keithley 2400 Source-Meter. We prepared two thin (~25x25x1.3 mm^3) film specimens of the conducting hydrogel. The four-point probe system was configured for single resistance measurements by sourcing 0.001 A of current and measuring voltage. We measured voltage five times in three locations of each film. Using a probe spacing of s = 1.59 mm and an average film thickness of t = 1.3 mm, we calculated the thickness correction factor, a, for our measurements using the following equation[36, 37]:

For t/s > 0.5: $a = \frac{1}{1+\frac{0.52632}{(\frac{t}{s})^{1.9}}}$

We then calculated the conductivity by taking the inverse of the following general expression for resistivity:

$$\rho = sa2\pi\left(\frac{V}{I}\right)$$

We calculated a conductivity of σ ~ 10.8 mS/m for the ionic liquid containing hydrogel.

4.9.3 Direct-Write Assembly of Sensors

The ink was loaded into a syringe with an attached stainless steel dispensing tip in place. We created planar arrays of sensors by layering the polyacrylamide and silicone inks. Once the sensors were patterned, we printed an encapsulating layer of silicone ink. While patterning the ink materials, we exposed them to 5 mW cm^{-2} using a UV lamp (Omnicure ® S1500; Excelitas) with a wavelength range, λ = 320 - 500 nm. The part was fully cured after printing and not post-printing curing step was needed.

4.9.4 PHD Actuator Fabrication

The actuators of the PHD are composed of a highly resilient silicone elastomer (Ecoflex 00-30; Smooth-On, Inc.), with an elastic modulus of ~ 40 kPa at 100% strain and ultimate strain of $\gamma_{ecoflex}^{ult}$> 900%. We fabricated these devices using soft lithography from 3D printed molds. We designed a mold for the pneumatic actuators and then fabricated them in Rigid Opaque Blue material (Fig. S4.4, VeroBlue RGD840; Stratasys, Inc.) using a 3D printer (Objet24; Stratasys, Inc.). We blended green pigment (Silc Pig ®; Smooth-On, Inc.) into a matrix of uncured Ecoflex 00-30, then degassed the polymeric melt and poured it into the mold. We cured the Ecoflex for 60 min at 80 ºC. We removed this part from the mold and layered it onto an inextensible composite sheet of Ecoflex and carbon fiber veil (Fibre-Glast, Inc.). We glued the extensible layer to the inextensible one using a thin layer of Ecoflex precursor.

Next, we inserted electrical wires (1 mm outer diameter) and pneumatic tubing (1 mm inner diameter) into their respective channels (Fig. 4.1a). Finally, we filled the well surrounding the electrical wiring with the conductive polyacrylamide ink. This ensured excellent contact between the electronic (wires) and ionic (polyacrylamide hydrogel) conductors. This also allowed seamless electrical contact to the capacitive sensors, which would be printed on the surface of this Ecoflex part. We chose a haptic display

design with four actuators because it yields 16 unique combinations with a simple on-off motif for tactile communication yet is also a compact design. This specific geometry considered hand and finger ergonomics, as well as integration of pneumatic feed tubes and electrical wiring.

4.9.5 PHD Controls

We connected the electrical wiring of our haptic device to the off-board microcontroller (AT Mega 2560): the ground plane of each sensor to the ground of the microcontroller and each of the four sensor channels to four separate digital input ports on the microcontroller (Fig. S4.5). The outputs of the four sensors were read and processed by the Arduino's Capacitive Sensing Library. This library measures capacitance by counting the amount of time it takes for the digital pin to change states (HIGH to LOW, or LOW to HIGH voltage) and outputting the corresponding digital timestamp. This digital timestamp is proportional to the capacitance via the time constant τ ($\tau = R \cdot C$), where R is resistance and C is capacitance. Since our capacitance measurements were derived from timestamps, it was necessary to calibrate the measurements. Though this method was not the most accurate capacitive measurement option, it allowed us to analyze the capacitance values of all four sensors simultaneously and in real-time.

We wrote a simple program to continuously monitor the capacitance values of each of the sensors. When the minimum threshold value for capacitance (25 pF) was met by a sensor, we considered this a 'button-press' and the microcontroller stored that sensor's identification (ID; 1 through 4) into a First-In-First-Actuated (FIFA) queue of length five. After 5 unique button presses, our control algorithm switched from 'sensing' mode to 'actuation' mode.

Using four separate digital output ports, we connected the microcontroller to four solenoid valves (Parker X-Valve). These valves controlled the pressure inside the four actuation chambers via the pneumatic tubing. The pressure in each chamber was

increased by 35 kPa with a control signal of HIGH and reduced back to atmospheric pressure with a control signal of LOW. During ‘actuation’ mode, the microcontroller was set to transmit the HIGH signal on each of the output channels corresponding to the IDs stored in the FIFA queue (generated during ‘sensing’ mode). Each output signal of HIGH lasted for duration of 2 seconds before moving on to the next ID in the queue. Upon completion of the final actuation in the sequence, the microcontroller would revert back to ‘sensing’ mode to receive a new sequence of five button presses.

The average response time of each of these chambers was approximately 120 ms. This value is a combination of the minimum response time of the solenoid valves we used plus the average time it takes for the pressure of the chamber to increase to ~ 28 kPa.

4.9.6 Average Force of Finger Press

We pressed on a precision balance (Mettler Toledo MS403S) and recorded the amount of force reported. We repeated this ten times over four trials and then calculated the average applied force by the finger used in the experiments to be ~ 2 N.

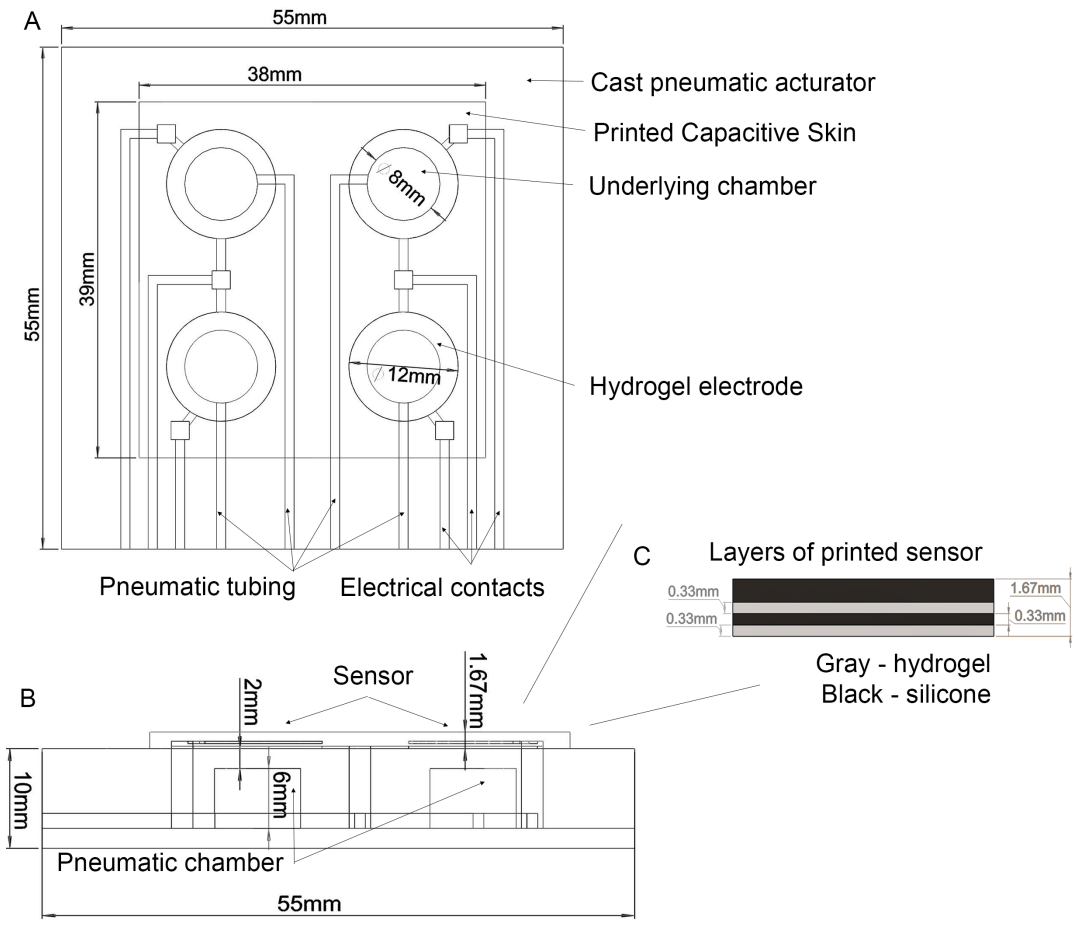

Figure S4.1| Schematic of PHD. (a) Top down schematic of PHD with overlaying capacitive skin. The four underlying pneumatic chambers are visible with the four overlaying sensors. Pneumatic and electrical lines are also shown. **(b)** Side view the PHD with overlaying capacitive skin. Two pneumatic chambers are shown with two overlaying sensors. **(c)** Expanded view of printed sensor, with printed electrodes in gray and printed insulator in black. The top layer of silicone is slightly thicker to ensure good encapsulation of sensors.

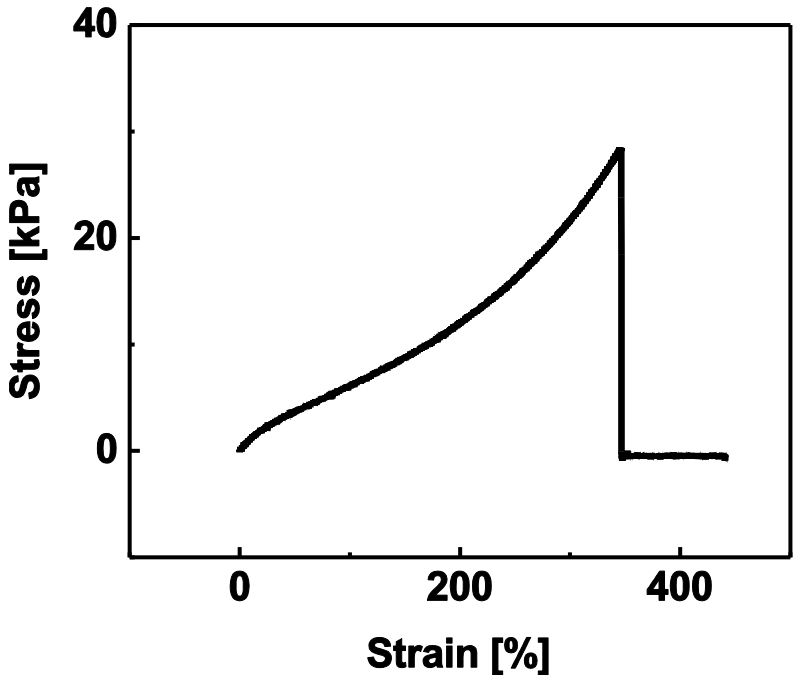

Figure S4.2| Uniaxial tensile test of conductive, polyacrylamide hydrogel.

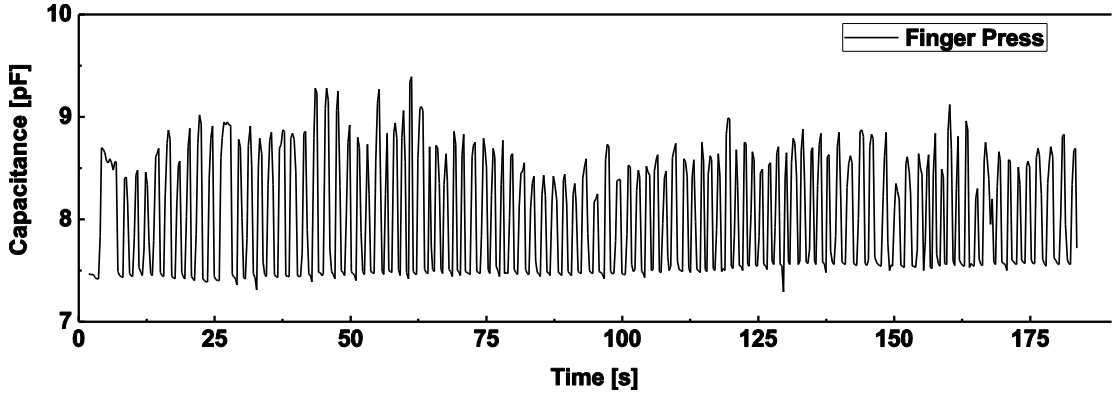

Figure S4.3| [99] repetitive presses of sensor with finger.

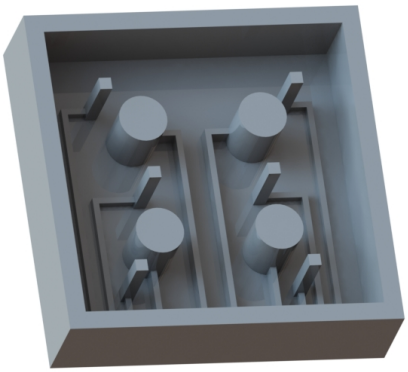

Figure S4.4| Soft lithographic mold for pneumatic haptic display.

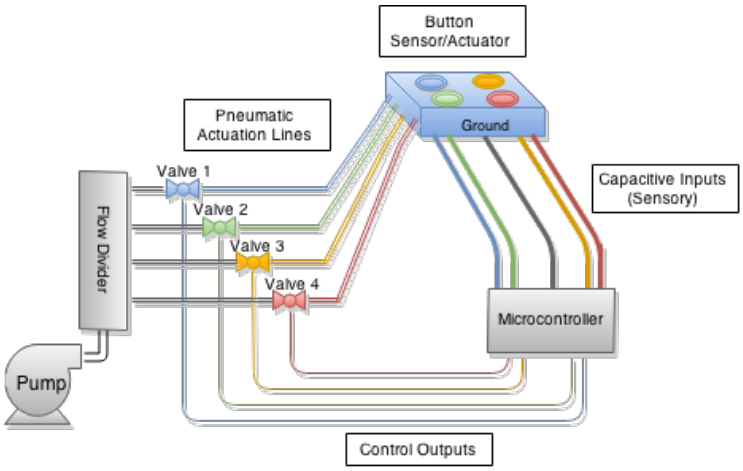

Figure S4.5| Off-board microcontroller configuration.

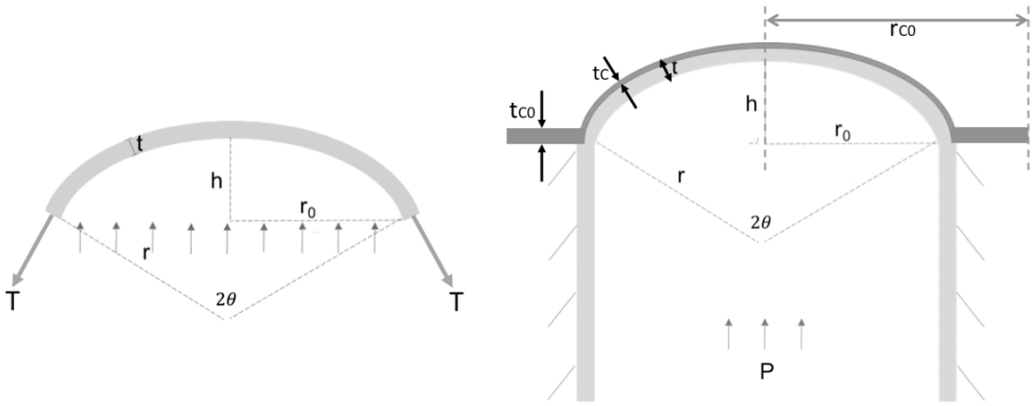

Figure S4.6| Free body diagram of actuator-sensor pair during pneumatic pressurization.

REFERENCES

[1] R. Pfeifer, M. Lungarella, F. Iida, *Commun. ACM* **2012**, *55*, 76.

[2] A. C. Guyton, *Textbook of Medical Physiology*, W.B. Saunders Company, **1981**.

[3] G. Frediani, D. Mazzei, D. E. De Rossi, F. Carpi, *Front Bioeng Biotechnol* **2014**, *2*, 31.

[4] D.-H. Kim, R. Ghaffari, N. Lu, J. A. Rogers, *Annu. Rev. Biomed. Eng.* **2012**, *14*, 113–128.

[5] P. Polygerinos, S. Lyne, Zheng Wang, L. F. Nicolini, B. Mosadegh, G. M. Whitesides, C. J. Walsh, in *2013 IEEE/RSJ International Conference on Intelligent Robots and Systems (IROS 2013)*, Ieee, **2013**, pp. 1512–1517.

[6] R. V. Martinez, J. L. Branch, C. R. Fish, L. Jin, R. F. Shepherd, R. M. D. Nunes, Z. Suo, G. M. Whitesides, *Advanced Materials* **2012**, *25*, 205–212.

[7] F. Ilievski, A. D. Mazzeo, R. F. Shepherd, X. Chen, G. M. Whitesides, *Angew. Chem. Int. Ed.* **2011**, *50*, 1890–1895.

[8] R. F. Shepherd, F. Ilievski, W. Choi, S. A. Morin, A. A. Stokes, A. D. Mazzeo, X. Chen, M. Wang, G. M. Whitesides, *Proceedings of the National Academy of Sciences* **2011**, *108*, 20400–20403.

[9] H. Zhao, Y. Li, A. Elsamadisi, R. Shepherd, *Extreme Mechanics Letters* **2015**, *3*, 89–104.

[10] C. M. Schumacher, M. Loepfe, R. Fuhrer, R. N. Grass, W. J. Stark, *RSC Adv.* **2014**, *4*, 16039.

[11] M. T. Tolley, R. F. Shepherd, B. Mosadegh, K. C. Galloway, M. Wehner, M. Karpelson, R. J. Wood, G. M. Whitesides, *Soft Robotics* **2014**, *1*, 213–223.

[12] A. D. Marchese, C. D. Onal, D. Rus, *Soft Robotics* **2014**, *1*, 75–87.

[13] B. Mosadegh, P. Polygerinos, C. Keplinger, W. Sophia, R. F. Shepherd, U. Gupta, J. Shim, K. Bertoldi, C. J. Walsh, G. M. Whitesides, *Advanced Functional Materials* **2014**, *24*, 2163–2170.

[14] D. Rus, M. T. Tolley, *Nature* **2015**, *521*, 467–475.

[15] Yong-Lae Park, Bor-Rong Chen, R. J. Wood, *IEEE Sensors J.* **2012**, *12*, 2711–2718.

[16] J. T. Muth, D. M. Vogt, R. L. Truby, Y. Mengüç, D. B. Kolesky, R. J. Wood, J. A. Lewis, *Advanced Materials* **2014**, *26*, 6307–6312.

[17] C. Yan, J. Wang, W. Kang, M. Cui, X. Wang, C. Y. Foo, K. J. Chee, P. S. Lee, *Advanced Materials* **2013**, *26*, 2022–2027.

[18] J.-Y. Sun, C. Keplinger, G. M. Whitesides, Z. Suo, *Advanced Materials* **2014**, *26*, 7608–7614.

[19] A. Frutiger, J. T. Muth, D. M. Vogt, Y. Mengüç, A. Campo, A. D. Valentine, C. J. Walsh, J. A. Lewis, *Advanced Materials* **2015**, *27*, 2440–2446.

[20] M. Ramuz, B. C. K. Tee, J. B. H. Tok, Z. Bao, *Advanced Materials* **2012**, *24*, 3223–3227.

[21] M. Kubo, X. Li, C. Kim, M. Hashimoto, B. J. Wiley, D. Ham, G. M. Whitesides, *Advanced Materials* **2010**, *22*, 2749–2752.

[22] M. Rashed Khan, G. J. Hayes, J.-H. So, G. Lazzi, M. D. Dickey, *Appl. Phys. Lett.* **2011**, *99*, 013501.

[23] M. Kollosche, H. Stoyanov, S. Laflamme, G. Kofod, *Journal of Materials Chemistry* **2011**, *21*, 8292–8294.

[24] W. Y. Du, S. W. Yelich, *Sensors and Transducers* **2008**, 1–25.

[25] J. E. Smay, G. M. Gratson, R. F. Shepherd, *Advanced Materials* **2002**, *14*, 1279–1283.

[26] D. Therriault, R. F. Shepherd, S. R. White, J. A. Lewis, *Advanced Materials* **2005**, *17*, 395–399.

[27] J. C. Conrad, S. R. Ferreira, J. Yoshikawa, R. F. Shepherd, B. Y. Ahn, J. A. Lewis, *Current Opinion in Colloid & Interface Science* **2011**, *16*, 71–79.

[28] R. A. Barry III, R. F. Shepherd, J. N. Hanson, R. G. Nuzzo, P. Wiltzius, J. A. Lewis, *Advanced Materials* **2009**, *21*, 2407–2410.

[29] J. N. Hanson Shepherd, S. T. Parker, R. F. Shepherd, M. U. Gillette, J. A. Lewis, R. G. Nuzzo, *Advanced Functional Materials* **2010**, *21*, 47–54.

[30] J. A. Lewis, *Advanced Functional Materials* **2006**, *16*, 2193–2204.

[31] J. Biggs, K. Danielmeier, J. Hitzbleck, J. Krause, T. Kridl, S. Nowak, E. Orselli, X. Quan, D. Schapeler, W. Sutherland, J. Wagner, *Angew. Chem. Int. Ed.* **2013**, *52*, 9409–9421.

[32] P. Brochu, Q. Pei, *Macromol. Rapid Commun.* **2010**, *31*, 10–36.

[33] C. Keplinger, J.-Y. Sun, C. C. Foo, P. Rothemund, G. M. Whitesides, Z. Suo, *Science* **2013**, *341*, 984–987.

[34] J. Bruneaux, D. Therriault, M.-C. Heuzey, *J. Micromech. Microeng.* **2008**, *18*, 115020.

[35] B. Chen, J. J. Lu, C. H. Yang, J. H. Yang, J. Zhou, Y. M. Chen, Z. Suo, *ACS Appl. Mater. Interfaces* **2014**, *6*, 7840–7845.

[36] L. B. Valdes, *Resistivity Measurements on Germanium for Transistors*, Proceedings of the I.R.E, **1954**.

[37] F. M. Smits, *Bell System Technical Journal* **1958**.

CHAPTER 5
CONCLUSION

3D printing has been utilized to create a wide variety of anatomic models and tools for procedural planning and training, but has yet to be used to create permanent, soft endocardial implants due to the unique challenges regarding hemocompatibility and durability of the printed materials. Here, I presented an approach for the rapid prototyping of patient-specific cardiovascular occluders via 3D printing and static molding of inflatable silicone/polyurethane balloons derived from volume rendered computed tomography (CT) scans. This approach provides custom-made implants fabricated using high quality, durable, and hemocompatible elastomeric materials. To illustrate the utility of this approach, I demonstrated the use of these devices for occlusion of the left atrial appendage (LAA), a structure known to be highly variable in geometry, and the primary source of stroke for patients with atrial fibrillation. I described the design workflow, fabrication, and deployment of these patient-specific LAA occluders as a proof-of-concept, and show their efficacy using 3D printed anatomic models, *in vitro* flow loops, and an *in vivo* large animal model.

Finally, I presented work on synthetic sensors that can be 3D printed, using direct ink writing (DIW) onto soft, fluidic elastomer actuators (FEAs). This 3D printing technique used two inks—one that was an ionically conductive hydrogel and another that was an electrically insulating silicone—which was patterned and photopolymerized into stretchable capacitive sensors. In that paper, the sensors were used to enable tactile sensing and kinesthetic feedback in a pneumatically actuated haptic device. The capacitive skin enabled the device to detect a compressive force from a finger press of ~2 N, and an internal pressurization of as low as ~ 10 kPa. By using a 5-axis conformal printer, and real-time surface mapping, it may be possible to directly print these soft sensors onto the surface of pre-fabricated left atrial appendage occluders.

APPENDIX - Second author publications

APPENDIX A

SELECTIVE MINERALIZATION OF TOUGH HYDROGEL LUMENS FOR SIMULATING ARTERIAL PLAQUE

Lihong Lao, Sanlin S. Robinson, Bryan Peele, Huichan Zhao, Benjamin C. Mac Murray, James K. Min, Bobak Mosadegh, Simon Dunham, and Robert F. Shepherd, *Advanced Engineering Materials*. **2016**, 19, 1, 1600591

A.1 Abstract

Recently, computational fluid dynamics (CFD) has been developed for modeling coronary artery pressure and flow, and predicting surgical outcomes for coronary artery disease (CAD). For accurate modeling, artificial arteries (phantoms) with occlusion need to be produced and used for measurement of fluid flow. This article demonstrates progress towards that goal—the molding of a hydrogel lumen using a tough polyacrylamide with regions selectively mineralized with calcium phosphate to fabricate phantoms that mimic plaque buildup. By tuning the degree of mineralization using conditions such as calcium concentration ($[Ca^{2+}]$, 0.4 M to 2 M), and crystallization time (t_c, 1 to 4 weeks), we control the extent of lumen occlusion. These synthetic, occluded lumens significantly reduce pressure (up to ΔP~7.79 kPa) during fluid flow compared to the non-calcified hydrogels (ΔP~1.24 kPa). Additionally, image and chemical analysis as well as compressive mechanical testing are performed to determine the effect of synthesis conditions on the composite's mechanical properties. For comparison to real arteries, we also present dynamic mechanical analysis of human aortic tissue.

A.2 Introduction

Coronary artery disease (CAD) is responsible for more than one third of all deaths in the U.S. and ~1.2 million hospitalizations annually.[1] CAD is characterized by the buildup of plaque in the coronary arteries, restricting blood flow, and thus oxygen perfusion to the myocardial tissue of the heart.[1, 2] Plaque is the region of thickening on the inner lining of the artery, which may result from intimal proliferation of smooth muscle cells, or formation of fat and inflammatory cells inside the intima.[2-4] As plaque grows it accumulates scar (fibrous) tissue and abundant calcium. Since crystallized calcium is hard, the plaque is often referred to as "hardening of the arteries". [3]

Both qualitative and quantitative assessment of how blood flows through these restricted pathways (stenoses) are used to assess the treatment of CAD in a patient. For example, computed tomography (CT) is as a non-invasive option for qualitative coronary angiography which now allows for acquisition of virtually motion-free images at isotropic spatial resolution of 400 μm.[5] Fractional flow reserve (FFR) is a quantitative assessment with a measurement that reports the potential decrease of coronary flow in a diseased artery, and thereby identifies a stenosis during coronary angiography and cardiac catheterization.[6] Due to the breadth and complexity of diagnostic tools, difficulty of patient access, and the variation in manifestations of the disease state itself it is useful to assess the flow dynamics and the performance of diagnostic and therapeutic medicine in controlled settings. Towards that goal, computational fluid dynamics (CFD) modeling has been developed that allows for modeling of coronary artery pressure and flow.[7, 8] Using CFD for diagnostics, however, remains uncertain when assessing complex flow and pressure calculations in plaque-laden arteries.[7, 9] Furthermore, simulating treatment or testing medical diagnostic tools cannot, presently, be done virtually.

For accurate modeling and validation, artificial arteries (phantoms) were produced and used for direct visualization of fluid through a stenosis.[10-16] Most prior designs have

been composed of inorganic materials such as glass,[10, 11] which do not match the material properties of soft tissues in real human arteries. Silicone-based elastomeric materials have also been widely used,[12, 13] such as Elastrat Sarl (Switzerland),[12] to construct phantom models; however, the phantoms were usually mono-layered and single material, and therefore did not reproduce the wall architecture or chemistry present in plaque. Other attempts have also been made to directly print vascular phantoms by 3D Polyjet printers, using either hard (acrylic) or elastomeric materials (polyurethane),[14] or by hydrogel molding, using polyvinyl alcohol (PVA).[16] In several cases, stenotic geometries were evaluated showing that these features will influence flow and deformational mechanics of the arterial wall.[15, 16] While these studies highlighted the importance of the mechanics of the stenosis, the materials (silicones and PVA) used were much softer than that of coronary calcium, which are orders of magnitude stiffer than healthy coronary tissue.[17] Ideally, these phantoms would represent a patient's specific arterial geometry, mechanics, and material properties for use in diagnostics and predicting the outcomes of invasive procedures.

In order to accurately simulate a patient's specific coronary arteries, we must be able to replicate both their shape and mechanical properties.[8, 18] Recently, hydrogels—swollen networks of hydrophilic polymer—have emerged as a viable material solution for mechanical devices. For instance, polyacrylamide (PAAm)-based hydrogels have been widely used as elastomeric matrices due to their high toughness and extensibility, as well as optical transparency.[19-21] With these properties, these hydrogel networks could provide support for liquid flow as a synthetic artery and have the potential for calcification to mimic the process of plaque formation that sometimes leads to CAD. In this paper, we describe a new approach to fabricate synthetic artery phantoms using tough polyacrylamide hydrogels that have been selectively mineralized to mimic plaque formation, both chemically and mechanically. We report compression tests to evaluate the mechanical properties of the calcified hydrogels, and image and chemical analysis of the calcium phosphate crystallization. Finally, we assessed the potential of these

synthetic lumens to be used as arterial phantoms via fluid flow at the rates and pressures typical of the human cardiovascular system.

A.3 Results and Discussion

We synthesized mineral-incorporated polyacrylamide hydrogels via photopolymerization and repeated mineralization in 0.4 M or 2 M calcium and phosphate solutions (Figure SA.1a, Supporting Information). Figure A.1 compares the SEM morphology of the bulk polyacrylamide hydrogels before and after repeated mineralization. The neat hydrogels showed a smooth and interconnected porous structure (Figure A.1a), consistent with prior reports.[22, 23] The mineralized samples, however, transformed from transparent to white from light scattering due to surface roughening and an index of refraction mismatch between hydrogel and mineralized crystal growth (Figure A.1b-f and Figure S A.1b, Supporting Information). The degree of crystallization and crystal morphology varied according to immersion time, t_c and solution concentration, $[Ca^{2+}]$.[24, 25] For short immersion times (one week) in low $[Ca^{2+}]$ concentrations (0.4 M), fine needle-like (acicular) crystals were formed along the pore walls (Figure A.1b, indicated by arrows); Energy dispersive X-ray spectroscopy (EDS) confirmed that these crystals are calcium phosphate, as indicated by calcium (Ca) and phosphorus (P) elements (Figure S A.1c, Supporting Information). When it was further immersed in the solution, repeatedly for four weeks, the minerals grew into flake-like (platy) crystals with a higher density (Figure A.1c). Increasing the ionic concentration of the solution to 2 M accelerated the mineral growth. As shown in Figure A.1d, finer and denser minerals were found in the gel after one week compared with those mineralized in 0.4 M solution (Figure A.1b). A still longer repeated incubation (four weeks) made minerals even denser, leading to a complete coverage of the gel by a thick layer of crystal needles (Figure A.1e). The morphology was analogous with what has been observed in the prior reports,[24, 26] and coronary plaque with tissue calcification.[27]

The increasing surface mineralization from the prolonged conditioning time is primarily due to surface nucleation on top of the already formed calcium phosphate crystals.[24, 25] We confirmed that the density of mineral on the interior of the gel is lower with a graded transition (Figure A.1f and Figure S A.1b, Supporting Information), likely due to the mineralized surface reducing diffusive transport of ionic species.[24] This is likely the reason for the drill-like appearance in the center of some hydrogel samples, especially for those mineralized in higher [Ca^{2+}] and longer t_c (the inset images in Figure A.1d, e). Therefore, the result is a gradient transition from a high elastic modulus mineral to a low elastic modulus hydrogel.

The chemical structures of the mineralized hydrogels were further verified by FTIR spectra, as shown in Figure A.2. In the neat polyacrylamide hydrogel (Figure A.2a), there were three characteristic peaks of the amide groups: 1652 cm^{-1}, 1606 cm^{-1} and 1417 cm^{-1} (denoted by asterisks), which represented –C=O stretching vibration of the amide (I) group, $–NH_2$ bending vibration of amide (II) group and –CN stretching vibration of amid group, respectively.[28] The broad peak between 3600-3000 cm^{-1} is attributed to the O–H of water, NH and CH_2 stretching of polyacrylamide.[26] The peaks at 2850 cm^{-1} and 1448 cm^{-1} were also due to CH_2 stretching and scissoring vibration, respectively.[26, 28] Because of the initial incorporation of phosphate ions, the neat hydrogel also has two characteristic peaks at 1066 cm^{-1} and 953 cm^{-1} (denoted by hollow triangles), which were stretching and bending of PO_4^{3-}, respectively.[25, 26] The peak at 1319 cm^{-1} may attribute to surface carbonate ions likely due to the absorption of atmospheric CO_2.[26]

When the hydrogel was repeatedly mineralized in calcium and phosphate solutions, there were noticeable decrease of amide peaks and increase of phosphate peaks (Figure A.2b-e), especially at 1652 cm^{-1} and 1066 cm^{-1} (or 1024 cm^{-1}, a slight shift in some samples), respectively. When calculating their relative strengths (peak height of PO_4^{3-} at 1066 cm^{-1} or 1024 cm^{-1} and peak height of amide at 1652 cm^{-1}), we found they

increased with [Ca^{2+}] and t_c. These results were consistent with the growth trend of the minerals in the hydrogels (Figure A.1).

The mechanical and material properties of plaque are dramatically different than arterial tissue.[17] Though plaque stretches circumferentially during blood pressure pulsation, it is also significantly compressed. Therefore, compressive tests are widely used to determine the mechanical behavior of atherosclerotic plaque tissues.[29, 30] To simulate the compressive mechanical properties of human arteries, we first measured the storage modulus (E') of healthy aortic tissue. Using dynamic mechanical analysis (DMA), we found a relatively frequency independent *E'* for healthy arteries that vary from E'~0.1 MPa to E'~2.5 MPa (Figure A.3a). For example, in human artery 1 and 3, *E'* was higher along the longitudinal cuts (E'_{avg}~0.6 MPa and E'_{avg}~1.1 MPa, respectively) than by circumferential cut (E'_{avg}~0.1 MPa and E'_{avg}~0.5 MPa, respectively). Prior reports showed the dynamic moduli varied in different parts of human arterial tissues and in patients with different ages, e.g. ~0.5-3 MPa in carotid, thoracic and abdominal aortae,[31] ~0.5-7 MPa in iliac and femoral arteries,[31] and ~13.5 MPa for human aortic valve tissue.[32] Our results of healthy aortic tissues fall within these ranges.

Our synthetic hydrogel (PAAm) demonstrated a similar frequency insensitive storage modulus, with the pure PAAm having a E'_{avg}~29 kPa, well below that of fixed human arteries. When the gels were mineralized in a low ionic concentration ([Ca^{2+}]~0.4 M) for one week the storage modulus increased to E'_{avg}~70 kPa, similar to the lower end of human arterial tissue. By controlling the immersion time (t_c) and ionic concentration ([Ca^{2+}]), we were able to tune the storage modulus of the synthetic hydrogel composite over the entire span of natural tissue. For example, increasing the ion concentration from 0.4 M to 2 M brought a significant increase of the dynamic modulus by ~75X in one week of mineralization (E'_{avg}~70 kPa vs. E'_{avg}~4.74 MPa, significance level p<0.05), and extending the immersion time from one week to four weeks brought a ~150X increase in 0.4 M ion solution (E'_{avg}~70 kPa vs. E'_{avg}~9.37 MPa, p<0.05), and ~3X in 2 M ion solution (E'_{avg}~4.74 MPa vs. E'_{avg}~15.81 MPa, p<0.05), respectively.

The difference of the moduli between the four week mineralized hydrogel in the 0.4 M and 2 M solutions was insignificant (E'_{avg}~9.37 MPa vs. E'_{avg}~15.81 MPa, p>0.05), as demonstrated by the overlapping of the top two curves. Both mineralization processes resulted in significantly higher storage moduli than healthy human arteries (p<0.05; sample size, n=3).

To determine what ranges of mechanical properties our synthetic materials can achieve, we performed monotonic compression tests over large strain ranges, as shown in Figure A.3b. The neat hydrogel showed an elastic modulus, E_{avg}~29 kPa, similar to that from the dynamic frequency sweep (Figure A.3a). Increasing both the ion concentration and mineralization time led to increased elastic moduli; however, the ultimate strain, ε_{ult}, was commensurately reduced. For example, samples mineralized in 0.4 M solution for four weeks had E_{avg}~2.2 MPa and ε_{ult}~0.13, and exposure to 2 M for four weeks resulted in a compressive storage modulus E_{avg}~2.4 MPa and ε_{ult}~0.06.

Prior reports on the mechanical properties of plaqued arterial tissue yield highly variable results.[33-35] For instance, a dynamic stiffness of 2.27±1.0 MPa has been observed for the calcified caps in human aortic plaques under a compression level of 1.2±0.2% and frequency ranging from 0.05 Hz to 10 Hz, 4-5 times stiffer than cellular caps.[33] In a static compressive mechanical test, non-fibrous human aortic plaque has been reported with a compressive modulus of 41±18 kPa under 24% strain, while that of fibrous and calcified plaques increased to 82±33 kPa (under 11% strain) and 355±245 kPa (under 3% strain), respectively.[34] Compressive behavior of calcified samples in carotid artery plaque was also reported with an average modulus of 140 kPa and 2.3 MPa at 5% and 20% compression, respectively.[35] These demonstrated our mineralized hydrogel has the potential to reach the stiffness of real human arteries with or without plaques under different controlled conditions.

We molded the tough hydrogel into synthetic lumens by UV curing the polyacrylamide in a transparent cylindrical mold (Figure S A.2a, Supporting Information). The lumens had an inner diameter, an outer diameter, and a total length of 2.74±0.15 mm, 6.48±0.20 mm and 60 mm, respectively (Figure A.4a). The inner diameter was similar to the mean value of the real coronary arteries from patients with acute coronary syndrome imaged via intravascular ultrasound.[36] The selective mineralization was realized by immersing the middle region of the lumen in the mineralization solution (0.4 M or 2 M) while both ends were submerged in deionized water (Figure A.4b), these fluids were renewed every 24 hours. Figure A.4c shows a lumen after mineralization in 0.4 M solution for four weeks (images of samples with short t_c can be found in Figure S2d,e, Supporting Information). We found the middle part calcified to completely white, while the sides remained transparent. The mineralization also occurred across the circumference of the lumen as indicated in Figure A.4d (left). Additionally, we found a swelling of the non-mineralized portion of the lumen during mineralization, i.e. the total length increased to L~74 mm (Figure A.4c), with the initial L_o~60 mm (Figure A.4a and inner tube in Figure A.4c); the circumferential wall also swelled and led to a higher expansion of the outer diameter (9.63±0.30 mm, ~48.6%) and shrinkage of the inner diameter (1.97±0.07 mm, ~28.1%) for the mineralized region (Figure A.4d, left) compared with the non-mineralized sides (Figure A.4d, right). In this view, an occlusion with ~33.0% nominal stenosis severity (the reduction of diameter)[16] has been selectively formed in the mineralized lumen.

To demonstrate the potential application of the mineralized hydrogel lumen as a phantom for a plaque occluded artery, we set up a fluid flow system to test the pressures during flux through the lumens (Figure A.5a). We cut the samples into 50 mm long lumens with a 10 mm center section that we mineralized to various extents, and then inserted them into fittings (Figure A.5b) connected to a water source. Figure A.5c shows the difference (ΔP) between the inlet (P_1) and outlet pressures (P_2) through various hydrogel lumens with the water flow (Q) from $37.9<Q<252.4$ mL min^{-1}; we chose the

maximum flow rate to approximate blood flow in the human internal carotid artery, Q~250 mL min^{-1}.[37, 38]

Overall, we found pressure drops across hydrogel lumens increased as the flow rate increased (Figure A.5), similar to measurements in natural arteries.[38] There was a strong correlation between the pressure drop, ΔP (P_2-P_1), across the lumen and degree of mineralization. The neat hydrogel lumen recorded a small ΔP ~1.24 kPa at the maximum flow rate. The one-week mineralization in 0.4 M solution did not bring significant difference in the pressure drop compared with the neat lumen (p>0.05), while the pressure driven flux for the gel mineralized in 2 M solution significantly deviated from that of the neat hydrogel at a higher flow rate (>150 mL min^{-1}; p<0.05). The drops were even more pronounced for lumens with a longer t_c of four weeks: under a maximum flow of 252.4 mL min^{-1}, the gel mineralized in 0.4 M solution generated a ΔP~5.58 kPa, and the one in 2 M solution led to a ΔP~7.79 kPa, about six times that of the non-mineralized neat sample.

In our model, the pressure drop was generally produced due to the stenosis of the lumen.[39] The difference of mechanical toughness between the middle mineralized region and two non-mineralized sides also contributes to the flow rate across the lumen. When blood flows through a natural lumen it expands; however, stiff plaque prevents this expansive deformation and may generate a local pressure difference.[40, 41] For example, prior CFD simulations of blood flow through a 60% diameter-reducing stenosis has been reported to generate a pressure drop of 2.53 kPa (19 mm Hg) under a hyperemic flow of 216 mL min^{-1}.[7] Another simulation across a 10 mm long 67% diameter-reducing carotid artery stenosis has also been reported to generate pressure drops ranging from severe 7.73 kPa (58 mm Hg) to mild 1.60 kPa (12 mm Hg) depending on the positions and shapes of the distal end of the plaque, under a mean blood flow of ~250 mL min^{-1}.[38] Figure A.5c demonstrates that our synthetic mineralization can achieve these features and be appropriately used for phantoms to complement CFD analysis and aid in modeling and predicting surgical outcomes for

CAD procedures. Our preliminary results are comparable with a prior study, where a pressure drop of 1.3-10.7 kPa (10-80 mmHg) was recorded with a flow rate of 30-210 mL min^{-1} along a synthetic stenosis model (with a higher nominal stenosis severity of 70%) made of PVA hydrogel as both lumen and occlusion.[16]

A.4 Conclusion

In summary, we have developed a mineralized hydrogel system as a synthetic model for coronary arteries with plaque buildup. By tuning the mineral concentration, [Ca^{2+}], and crystallization time, t_c, we controlled the mechanical properties and degree of occlusion of the hydrogel lumens. The occluded lumen generated large pressure drops and commensurately lower flow rates compared with non-mineralized hydrogels; these effects could be tuned to comparable or more severe conditions than those related to natural arterial occlusions. Due to the similarity of our synthetic material constituents to natural ones, these phantoms are likely better simulations for coronary calcification than previous alternatives. Since the mechanical properties of these hydrogel-based arteries mimic that of diseased ones *in vivo,* they could be used as a learning tool for clinical fellows to practice procedures (e.g., angioplasty, coronary artery bypass grafting (CABG), stent), or as an *in vitro* system to develop interventional or implantable devices. Furthermore, the molding technique allows these arteries to be fabricated in patient-specific geometries that will be useful for interventionalists and surgeons to plan for individual procedures.

Future improvement of our synthetic lumens will better mimic the shape and exact material properties of patient specific arteries for improved phantom fidelity. For example, the hydrogel lumen and the flow test could be better designed to simulate real artery behavior, such as molding branched arteries, replacing water with blood formula for the pressure test, and applying a pulsatile flow.[12, 13] Flow testing should also be performed on these materials using conventional medical imaging (CT, echocardiogram, and MRI) to assess their ability to simulate realistic tissue response

and not just a time and position averaged flow response. Finally, though not shown in this paper, it would be possible to accelerate the crystal growth and reduce the time required to cause the occlusion by further shortening the cycling time (t_c) and increasing calcium concentration ([Ca^{2+}]).

A.5 Experimental Section

A.5.1 Hydrogel preparation

The polyacrylamide hydrogels were synthesized using the following protocol.[20, 26] Acrylamide monomer (AAm; Sigma, A8887) was dissolved in deionized water, with AAm fixed at 2.2 M. The solution was subsequently mixed with a crosslinker, N,N′-methylene bisacrylamide (MBAA; Sigma, M7279) set at 0.01 the weight of AAm, a photoinitiator, Darocur® 1173 (BASF) was added at 0.15 wt% in solution, and ammonium phosphate dibasic ($(NH_4)_2HPO_4$; Sigma, 215996) was used at 0.4 M in solution. We stirred the solution overnight, at room temperature, until the solution was homogeneous and then poured it into a paper cup mold (diameter~62 mm, height~10 mm) with thickness of 3 mm and cured it via exposure to 365 nm light (350 W; OmniCure® S1500 A UV light curing system, Lumen Dynamics Group Inc) for 5 minutes. The sample was kept in a refrigerator (4 °C) overnight so the reaction could approach completion while limiting desiccation.[42]

A.5.2 Mineralization

To mineralize the hydrogels, we immersed them in a solution containing 0.4 M or 2 M calcium chloride ($CaCl_2$; Sigma, C1016) at room temperature.[24, 26] After 24 hours, the samples were extensively washed with deionized water to remove surface precipitates and immersed in a fresh solution containing $(NH_4)_2HPO_4$ with concentrations of 0.4 M

or 2 M, respectively. We repeated these steps from one to four weeks for increasing degrees of mineralization (Figure S1a, Supporting Information). After the desired time, we washed the mineralized gels and wipe-dried the surface for further analysis.

A.5.3 Morphology analysis

We used scanning electron microscopy (SEM) to observe the microstructure of the neat and mineralized PAAm hydrogel samples. To prepare the samples for the vacuum conditions of the SEM, we freeze dried them using liquid nitrogen.[22] We then coated the samples with a thin layer of gold palladium and observed them on a Tescan Mira3 FESEM. We used energy-dispersive X-ray spectroscopy (EDS) for elemental analysis.

A.5.4 Chemical analysis

We used a fourier transform infrared (FTIR) spectrometer (Nicolet Magna-IR® 560) to check the chemical composition of the freeze-dried neat and mineralized PAAm hydrogels. We cut a thin piece (~1 mm) of each sample for testing, and set the scan range to 4000-400 cm^{-1} and resolution to 2 cm^{-1}.

A.5.5 Mechanical test

We measured the mechanical properties of neat and mineralized hydrogels using dynamic mechanical analysis (DMA; TA Instruments, Q800) equipped with two parallel compression platens (12.7 mm in diameter). The samples were ~6.5 mm in diameter and ~3.0 mm in height (measured automatically via DMA software). We tested five parallel specimens for each set of samples. To obtain the dynamic storage moduli (E') of the hydrogels, the samples were compressed by preloading to 0.1 N contact force and applying a frequency sweep from 1 to 10 Hz using 0 to 2% compressive strain, *[L_0-*

$L]/L_0$, where L_0 is original specimen length and L is ultimate specimen length. We also measured the stress vs. strain relationship in monotonic compression using the DMA by preloading hydrogel samples to 0.1 N and compressing at a force ramp rate of 3 N min^{-1} with an upper force limit of 18 N. Compressive elastic moduli (E) were calculated from the 0 to 4% stress-strain curves. For convenience of expression, the neat and mineralized hydrogel was notated as NH and MH in the DMA curves, respectively.

A.5.6 Arterial DMA test

We also tested fixed, human aortic tissue (cadaveric, Weill Cornell Medicine) in tension using DMA. To ensure the samples would not dry out during testing we equipped the instrument with a small chamber that we filled with saline solution. In addition, we modified the clamps of the DMA with sandpaper to better grip the tissue specimens. Using a #11 scalpel, we cut circumferential and longitudinal samples from a large rectangular aortic specimen (the original tubular specimen had already been opened when we received them). We applied a pre-load force of 0.1 N, and then performed a frequency sweep from 0.1 to 10 Hz. The sample along longitudinal and circumferential cut was notated as HA (LC) and HA (CC) on the DMA curve, respectively.

A.5.7 Selectively mineralized lumens

Using polyacrylamide, we molded synthetic lumens by casting the acrylamide solutions into a transparent cylindrical mold (the inner diameter, outer diameter and total length was ~2.7 mm, 6.5 mm and 60 mm, respectively; Figure S2a, Supporting Information). To ensure the uniform crosslinking, we initially kept the mold with the solution vertically standing, after ~1 min curing, we flipped the mold to be horizontal and rotated it under the light so that all the parts of the tube would be exposed to the light. We then

placed the molded lumens into a 3D-printed mold designed to isolate and selectively mineralize a segment of the hydrogel (Figure S2b, Supporting Information). The three segment lengths (left, middle, and right) of the mold were 25 mm, 10 mm, and 25 mm, respectively. The middle section was initially filled with calcium chloride solution (0.4 M or 2 M) to mineralize the middle part of the lumen, the left and right sections were filled with deionized water. The joints of the mold assemblies were completely sealed by silicones (Ecoflex 00-30; Smooth-On Inc.) to avoid the calcium solution leaking from the inner region to the lumen extremities. The mineralization was then repeated alternatively between phosphate and calcium solutions for up to four weeks.

A.5.8 Liquid flow test

We measured the hydraulic flux through the hydrogel lumens using a custom built flow apparatus. The difference between input and output pressures (ΔP) displayed in two pressure gauges (McMaster Carr, 3847K71) along the lumens was measured while the flow rate (Q) was gradually increased at an interval of 25.2 mL min^{-1} (measured using an Omega, FLDA3422G; with measurement range of 0 to 325 mL min^{-1}).[43] The neat and selectively mineralized hydrogel lumen was notated as NHL and MHL in the pressure curves, respectively. We analyzed the experimental data using ANOVA. The significance level was set as $p<0.05$. Results were reported as mean ± standard deviation.

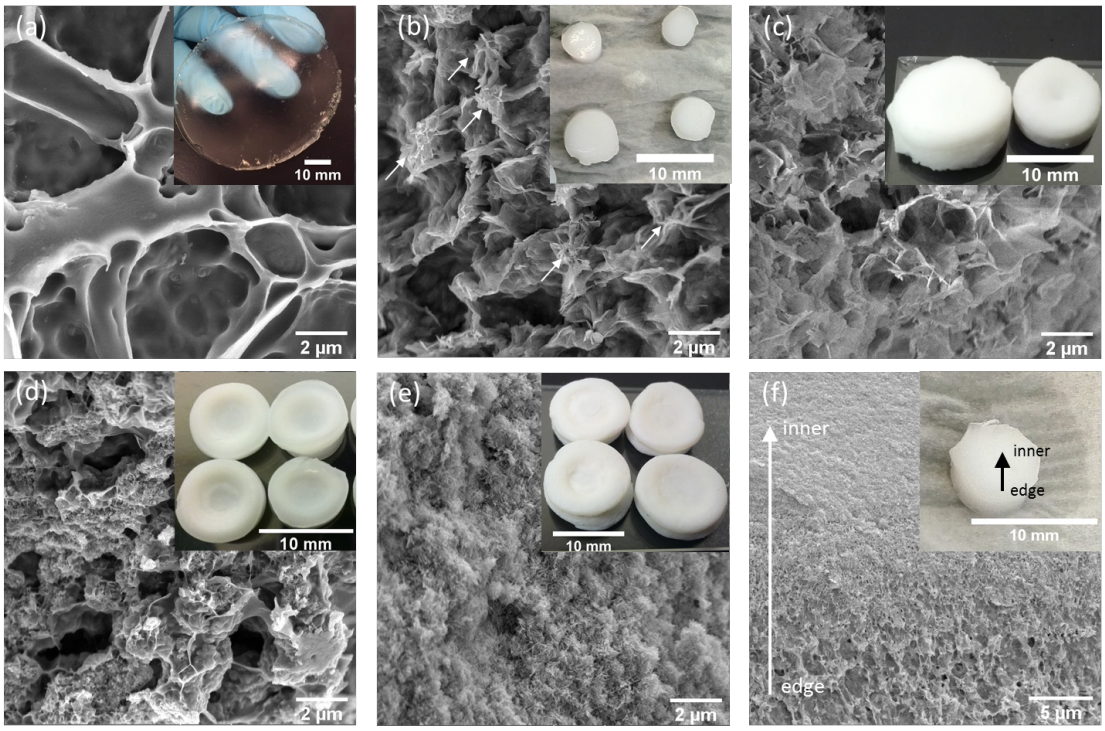

Figure A.1| SEM morphologies of polyacrylamide (PAAm) hydrogel loaded with phosphate ions. (a) before and (b-f) after repeated mineralization in calcium and phosphate solutions under different conditions: (b) 0.4 M solution for 1 week, (c) 0.4 M solution for 4 weeks, (d) 2 M solution for 1 week and (e) 2 M solution for 4 weeks, respectively. (f) Cross section of mineral gradient from edge to inner of a hydrogel sample after mineralized in 0.4 M solution for 1 week. Insets are the sample images.

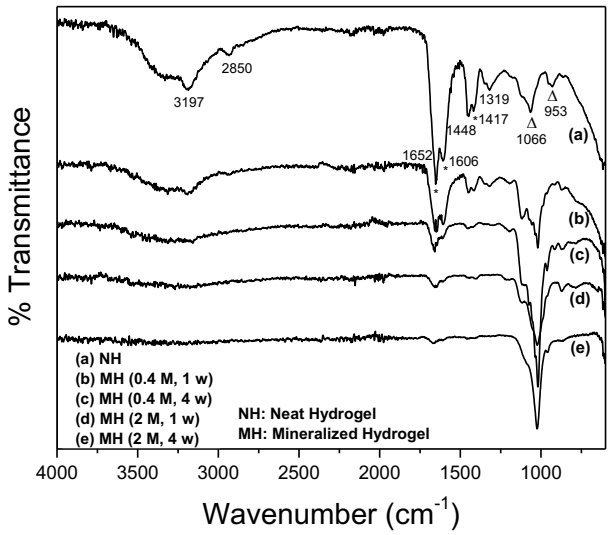

Figure A.2| FTIR spectra of polyacrylamide (PAAm) hydrogel loaded with phosphate ions. (a) before and (b-f) after repeated mineralization under different conditions. The symbols * and Δ in (a) represent characteristic peaks associated with amide and PO_3^{4-} groups of the polyacrylamide and minerals, respectively. NH and MH stand for neat hydrogel and mineralized hydrogel, respectively.

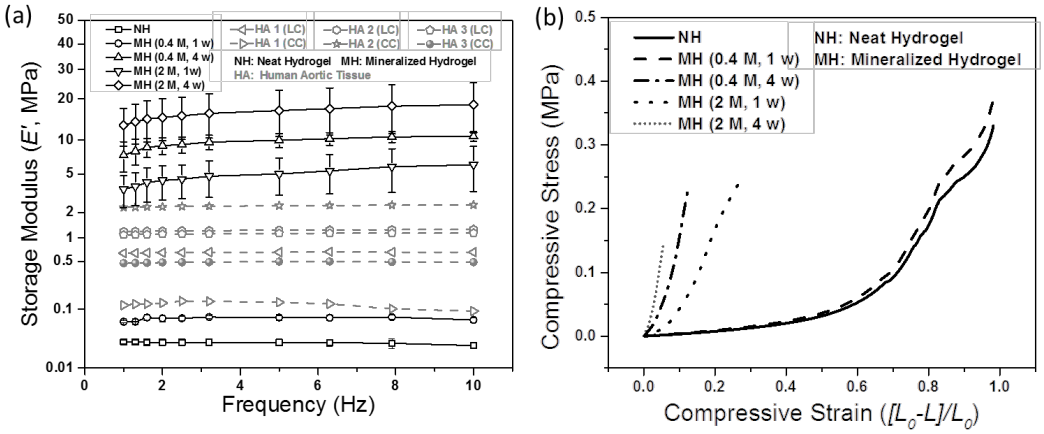

Figure A.3| Mechanical properties tested via dynamic mechanical analysis (DMA) for PAAm hydrogels before and after repeated mineralization under different conditions. (a) Storage modulus along with frequency sweep and (b) Compressive stress−strain curves. NH, MH, HA (LC) and HA (CC) stand for neat hydrogel,

mineralized hydrogel, human aortic tissue (longitudinal cut) and human aortic tissue (circumferential cut), respectively.

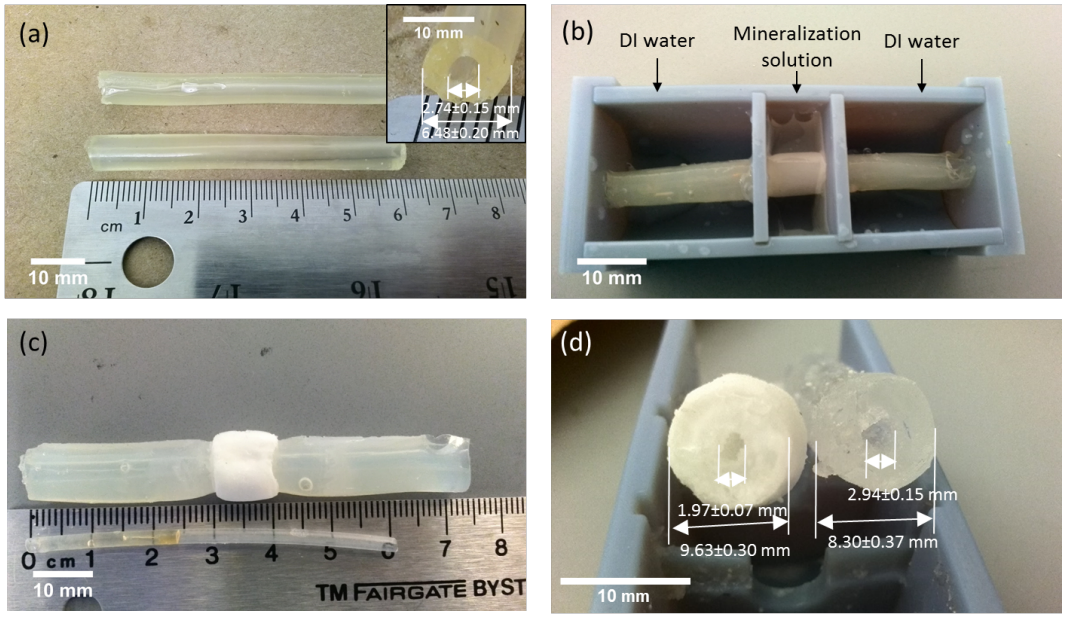

Figure A.4| Images of PAAm hydrogel lumen before and after repeated mineralization. (a) As-prepared PAAm hydrogel lumen with the inset cross section image. (b) Hydrogel lumen sitting in the 3D-printed mold for selective mineralization. (c) Hydrogel lumen after mineralization in 0.4 M solution for 4 weeks, compared with the original inner tube in the mold during curing and (d) Cross section view of the middle mineralized region (left) and non-mineralized region (right) within a same sample of (c).

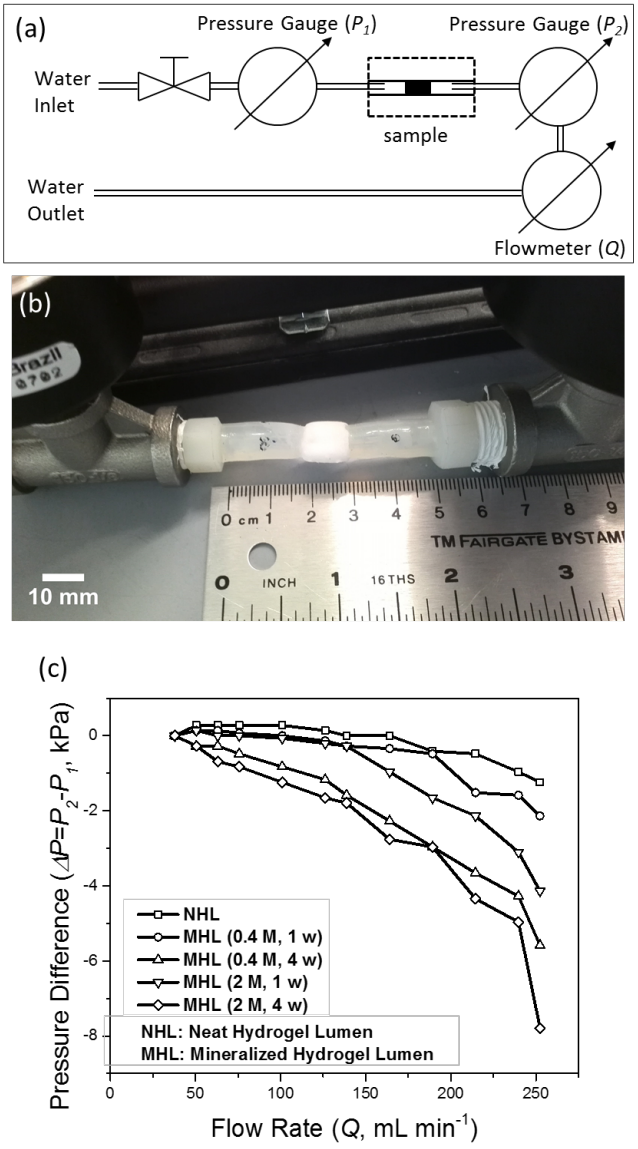

Figure A.5| Water flow test across PAAm hydrogel lumens before and after repeated mineralization. (a) Scheme of hydraulic flow test setup. (b) Image of a selectively mineralized hydrogel lumen sample connected within the flow system. (c) Pressure difference across various hydrogel lumens with the increase of flow rate. NHL and MHL stand for neat hydrogel lumen and mineralized hydrogel lumen, respectively. Supplemental information is available in the online version of this paper.

REFERENCES

[1] D. Lloyd-Jones, R. J. Adams, T. M. Brown, M. Carnethon, S. Dai, G. De Simone, T. B. Ferguson, E. Ford, K. Furie, C. Gillespie, A. Go, K. Greenlund, N. Haase, S. Hailpern, P. M. Ho, V. Howard, B. Kissela, S. Kittner, D. Lackland, L. Lisabeth, A. Marelli, M. M. McDermott, J. Meigs, D. Mozaffarian, M. Mussolino, G. Nichol, V. L. Roger, W. Rosamond, R. Sacco, P. Sorlie, V. L. Roger, T. Thom, S. Wasserthiel-Smoller, N. D. Wong, J. Wylie-Rosett, C. American Heart Association Statistics, S. Stroke Statistics, *Circulation* **2010**, *121*, e46.

[2] Y. S. Chatzizisis, A. P. Antoniadis, J. J. Wentzel, G. D. Giannoglou, *Atherosclerosis* **2014**, *236*, 351.

[3] J. C. Kovacic, P. Moreno, E. G. Nabel, V. Hachinski, V. Fuster, *Circulation* **2011**, *123*, 1900.

[4] M. R. Dweck, V. Puntman, A. T. Vesey, Z. A. Fayad, E. Nagel, *JACC Cardiovasc. Imag.* **2016**, *9*, 306.

[5] P. Maurovich-Horvat, M. Ferencik, S. Voros, B. Merkely, U. Hoffmann, *Nat. Rev. Cardiol.* **2014**, *11*, 390.

[6] J. M. Daessle, *Soins* **2011**, S3.

[7] C. A. Taylor, T. A. Fonte, J. K. Min, *J. Am. Coll. Cardiol.* **2013**, *61*, 2233.

[8] K. Govindaraju, I. A. Badruddin, G. N. Viswanathan, S. V. Ramesh, A. Badarudin, *Phys. Med.* **2013**, *29*, 225.

[9] B. K. Lee, *Korean Circ. J.* **2011**, *41*, 423.

[10] D. W. Liepsch, H. J. Steiger, A. Poll, H. J. Reulen, *Biorheology* **1987**, *24*, 689.

[11] M. Grigioni, A. Amodeo, C. Daniele, G. D'Avenio, R. Formigari, R.M. Di Donato, *Artif. Organs* **2000**, *24*, 946.

[12] R. Bordas, S. Seshadhri, G. Janiga, M. Skalej, D. Thevenin, *Interv. Med. Appl. Sci.* **2012**, *4*, 193.

[13] A. Ugron, M. I. Farinas, L. Kiss, G. Paal, *Exp. Fluids* **2012**, *52*, 37.

[14] C. N. Ionita, M. Mokin, N. Varble, D. R. Bednarek, J. P. Xiang, K. V. Snyder, A. H. Siddiqui, E. I. Levy, H. Meng, S. Rudin, *Proc. SPIE Int. Soc. Opt. Eng.* **2014**, *9038*.

[15] J. Brunette, R. Mongrain, J. C. Tardif, *J. Visual.* **2004**, *7*, 241.

[16] J. Ji, S. Toubaru, S. Kobayashi, H. Morikawa, D. L. Tang, D. N. Ku, *J. Biomech. Sci. Eng.* **2011**, *6*, 79.

[17] A. C. Akyildiz, L. Speelman, F. J. Gijsen, *J. Biomech.* **2014**, *47*, 773.

[18] Z. Sun, L. Xu, *Comput. Med. Imag. Graph.* **2014**, *38*, 651.

[19] J. Y. Sun, X. Zhao, W. R. Illeperuma, O. Chaudhuri, K. H. Oh, D. J. Mooney, J. J. Vlassak, Z. Suo, *Nature* **2012**, *489*, 133.

[20] C. Keplinger, J. Y. Sun, C. C. Foo, P. Rothemund, G. M. Whitesides, Z. Suo, *Science* **2013**, *341*, 984.

[21] C. Larson, B. Peele, S. Li, S. Robinson, M. Totaro, L. Beccai, B. Mazzolai, R. Shepherd, *Science* **2016**, *351*, 1071.

[22] S. Kim, G. Iyer, A. Nadarajah, J. M. Frantz, A. L. Spongberg, *Int. J. Polym. Anal. Ch.* **2010**, *15*, 307.

[23] L. M. Lira, K. A. Martins, S. I. C. de Torresi, *Eur. Polym. J.* **2009**, *45*, 1232.

[24] T. Yokoi, M. Kawashita, K. Kikuta, C. Ohtsuki, *Mater. Sci. Eng. C-Mater. Biol. Appl.* **2010**, *30*, 154.

[25] L. H. Lao, Y. Zhu, Y. Y. Zhang, Z. Y. Gao, F. Zhou, L. K. Chen, H. W. Ouyang, C. Y. Gao, *Adv. Eng. Mater.* **2012**, *14*, B123.

[26] M. I. A. Joshy, K. Elayaraja, R. V. Suganthi, S. N. Kalkura, *Cryst. Res. Technol.* **2010**, *45*, 551.

[27] H. E. Barrett, E. M. Cunnane, E. G. Kavanagh, M. T. Walsh, *J. Mech. Behav. Biomed. Mater.* **2016**, *56*, 45.

[28] L. T. Chiem, L. Huynh, J. Ralston, D. A. Beattie, *J. Colloid Interf. Sci.* **2006**, *297*, 54.

[29] C. K. Chai, L. Speelman, C. W. Oomens, F. P. Baaijens, *J. Biomech.* **2014**, *47*, 784.

[30] J. Walraevens, B. Willaert, G. De Win, A. Ranftl, J. De Schutter, J. V. Sloten, *Med. Eng. Phys.* **2008**, *30*, 1098.

[31] B. M. Learoyd, M. G. Taylor, *Circ. Res.* **1966**, *18*, 278.

[32] K. O. Lim, D. R. Boughner, *Circ. Res.* **1976**, *39*, 209.

[33] R. T. Lee, A. J. Grodzinsky, E. H. Frank, R. D. Kamm, F. J. Schoen, *Circulation* **1991**, *83*, 1764.

[34] R. T. Lee, S. G. Richardson, H. M. Loree, A. J. Grodzinsky, S. A. Gharib, F. J. Schoen, N. Pandian, *Arterioscler. Thromb.: Vasc. Biol. / Am. Heart Assoc.* **1992**, *12*, 1.

[35] E. Maher, A. Creane, S. Sultan, N. Hynes, C. Lally, D. J. Kelly, *J. Biomech.* **2009**, *42*, 2760.

[36] J. T. Schrauwen, D. J. Koeze, J. J. Wentzel, F. N. van de Vosse, A. F. van der Steen, F. J. Gijsen, *An. Biomed. Eng.* **2015**, *43*, 59.

[37] Z. F.Yang, H. T.Yu, G. P. Huang, R. Schwieterman, B.Ludwig, *J. Coast. Life Med.* **2015**, *3*, 245.

[38] B. K. Lal, K. W. Beach, D. S. Sumner, *J. Vasc. Surg.* **2011**, *54*, 1461.

[39] Z. Y. Li, J. H. Gillard, *J. Am. Coll. Cardiol.* **2008**, *52*, 499.

[40] A. Karimi, R. Razaghi, A. Shojaei, M. Navidbakhsh, *Biomed. Eng. - Biomed. Tech.* **2015**, *60*, 593.

[41] K. van der Heiden, A. Hoogendoorn, M. J. Daemen, F. J. Gijsen, *Thromb. Haemost.* **2016**, *115*, 501.

[42] J. Y. Li, W. B. K. Illeperuma, Z. G. Suo, J. J. Vlassak, *ACS Macro Lett.* **2014**, *3*, 520.

[43] B. C. Mac Murray, X. An, S. S. Robinson, I. M. van Meerbeek, K. W. O'Brien, H. C. Zhao, R. F. Shepherd, *Adv. Mater.* **2015**, *27*, 6334.

APPENDIX B

HIGHLY STRETCHABLE ELECTROLUMINESCENT SKIN FOR OPTICAL SIGNALING AND TACTILE SENSING

Chris M. Larson†, Bryan N. Peele†, Shuo Li†, Sanlin S. Robinson, Massimo Totaro, Lucia Beccai, Barbara Mazzolai, Robert F. Shepherd, *Science*, **2016**, 351(6277), 1071

† These authors contributed equally to this work.

B.1 Abstract

A hyperelastic light emitting capacitor, or HLEC, that can strain more than twice that of other stretchable displays is reported. This field-driven electroluminescent device is capable of stretching uniaxially to >480% strain and expanding its surface area by >635% while actively emitting light. These devices are layers of transparent hydrogel electrodes that sandwich a ZnS phosphor-doped dielectric elastomer layer, essentially thin rubber sheets that change illuminance and capacitance under deformation. An array of individually controllable HLEC pixels is fabricated using replica molding and subjected to stretching, folding, and rolling to demonstrate their use as stretchable displays. These sheets are then integrated into the skin of a soft robot, providing it with dynamic coloration and sensory feedback from external and internal stimuli.

B.2 Introduction

Biological systems employ a host of strategies for visual display and camouflage. Cephalopods, for example, can mimic their environment by changing skin color and

texture, as well as posture (*1*). Recent developments in soft robotics (*2, 3*), bioinspired design (*4, 5*), and stretchable electronics (*6*) reveal strategies that enable us to engineer some of the functions of cephalopod skin synthetically. For example, microfluidic networks filled with liquid dyes have been used as active camouflage and displays for soft mobile robots, giving them the ability to change their appearance via color, texture, and luminescence (*7*). More recently, electromechano-chemically responsive films were exploited to render fluorescent patterns under the control of electric fields (*8*), and adaptive optoelectronic camouflage systems have been used to mimic the visual appearance of cephalopod skin (*9*). Another approach is the use of active display technologies, such as polymeric light emitting devices (PLEDs) and organic light emitting diodes (OLEDs), which use stretchable, transparent electrodes based on indium tin oxide films (ITO) (*10*), graphene (*11*), single or multi-walled carbon nanotubes (SWNT, MWNTs) (*12, 13*), polyethylene-dioxythiophene: polystyrene-sulfonate (PEDOT:PSS) (*14*), or other percolated networks of conductive colloids or nanowires (*15*). Despite the broad applicability of LED-based systems for consumer displays, their electrical function is limited to ultimate strains, $\varepsilon_{ult} < 120\%$ (*16*), well below the ultimate strain of elastomers (e.g. silicones; $\varepsilon_{ult} \sim 400$ - 700%) that are used in soft robotics to mimic the movements of animals.

Biological skin also enables animals to sense their environments. A number of approaches have been used to create pressure sensitive electronic skins, including arrays of organic field-effect transistors (FETs) deposited on flexible parylene-polyamide substrates (*17, 18*) and inside stretchable rubber (*19*), as well as thin Au films and liquid-metal embedded in polydimethylsiloxane (PDMS) (*20, 21*). More recently, dielectric elastomer transducers (DETs), stretchable capacitors composed of highly extensible ionic hydrogels, have been used. These hydrogels are intrinsically soft, highly transparent in the visible spectrum (extinction coefficient, $\mu_{ext} \sim$10-6 μm-1) (*22*), can exhibit very high ultimate strain ($\varepsilon_{ult} \sim$2,000%) and toughness ($U \sim$9 kJ m-2) (*23*), and have relative changes in resistivity with strain that are orders of magnitude less than

electrodes based on percolated networks of conductive particles (e.g., metal nanoparticles, carbon powder, nanotubes) (*24*).

Presently, soft robots are primarily used because their low mechanical compliance enables safe human robot interaction; however, their potential is limited by a lack of suitable electronics that can stretch continuously with their bodies. No soft robot can dynamically display information on its body, and there are relatively few examples that can sense external and internal stimuli. Here we present a hyperelastic light emitting capacitor, HLEC, that enables both light emission and touch sensing in a thin rubber sheet that stretches to >480% strain (Fig. B.1A).

B.3 Design & Fabrication of HLECs

These HLECs are comprised of ionic hydrogel electrodes and composites of doped ZnS phosphors embedded in a dielectric matrix of silicone elastomer. We use electroluminescent phosphor powders that emit light via excitations within intrinsic heterojunctions under an AC electric field; unlike current-driven LEDs which require lithography to form p-n junctions, this material system can be processed using replica molding. Application of an AC electric field causes luminescence within the semiconducting phosphor at wavelength centers corresponding to the dopants in the ZnS lattice. Green and blue centers are typically produced using low (~0.01 wt. %) and high (~0.1 wt. %) concentrations of Cu, while yellow is produced using Mn (~1 wt. %) (25). White light can be achieved using combinations of these dopants.

The HLEC (Fig. B.1B) is a five-layer structure consisting of an electroluminescent dielectric layer that is sandwiched between two electrodes and encapsulated in low elastic modulus (E ~30 kPa) (*26*) silicone (Ecoflex 00-30, Smooth-on Inc.).

Our hydrogel electrodes are designed with a balance of high mechanical toughness, low volatility, and low electrical resistance under deformation (Fig. SB.1). Aqueous lithium

chloride (LiCl) is used as the ionic conductor due to its high conductivity (~10 S m-1), ionic strength, and hygroscopic nature, while polyacrylamide (PAM) is used as the elastomeric matrix for its high toughness (*27*) and optical transparency. Electrodes are synthesized by first dissolving acrylamide monomer (AAm), polyacrylamide, and N,N'-methylenebisacrylamide crosslinker in aqueous LiCl and casting the solution onto a UV-ozone treated silicone (Ecoflex 00-30) substrate. The aqueous PAM-AAm solution is then crosslinked under UV light (*28*), producing a highly stretchable and transparent electrode.

The EL layer is formed by mixing commercially available phosphor powders (Global Tungsten & Powders Corp.) (25 μm, ~8 % by volume) into silicone (Ecoflex 00-30) and then molding the dispersion into to a 1 mm-thick sheet. Finally, we bond the EL layer between the two electrode patterned silicone substrates and encapsulate the capacitor in an insulating layer of silicone.

B.4 HLEC Performance

B.4.1 Mechanical

The stress-strain curves of the HLEC and its silicone containing layers (Ecoflex and Ecoflex-EL composite) are all coincident, while the elastic modulus of the hydrogel is two orders of magnitude lower, allowing the HLEC to stretch freely without delaminating. Mechanical testing data (Fig. B.1C) and images (Fig. B.2A; Movie SB.1) show the excellent adhesion between the layers. The HLEC achieved a mean strain of 487 ± 59% (SD), as measured at five locations across the width of the illuminated section, with portions exceeding 500% prior to the external copper leads losing contact with the hydrogel electrodes. For these tests, the HLECs were operated at 700 Hz under a nominal electric field of ~25 kV cm^{-1} with a power consumption of 0.2 W and a luminous efficacy of 43.2 millilumens per Watt (mlm W^{-1}) (*28*). We use this same

replica molding technique to form an 8x8 array of 4 mm pixels (Fig. B.3A). This HLEC display can undergo many deformation modes including stretching, rolling, folding, and wrapping (Fig B.3B-E, Movie SB.2). Dynamic control of the pixels is shown in Figures B.3F-I.

B.4.2 Dielectric elastomer sensor

In addition to emitting light, the HLEC also serves as a dielectric elastomer sensor (DES) due to its construction as a parallel plate capacitor. Changes in the electrode area (A) and separation distance (d) cause the capacitance (C) to change according to $C/C_0 \propto Ad^{-1}$, allowing the HLEC to sense deformations from pressure and stretching. The capacitance of the HLEC changes as it is stretched under uniaxial (Fig. B.2B) and biaxial (Fig. SB.2) tension (*28*). We model the capacitance by expressing A and d in terms of the principal stretches, $\lambda 1$, $\lambda 2$, and $\lambda 3$, which represent the axial, transverse, and out-of-plane orientations, respectively (supplementary text below). For uniaxial boundary conditions, we observe the relative capacitance increases linearly as the sample is stretched (Eq. SB.11). For biaxial test conditions, we observe that the relative change in capacitance follows $C/C_0 = \lambda^4$, (Eq. SB.12); however, at higher strains the measured values are slightly lower due to a decrease in the permittivity of the dielectric (*24*).

B.4.3 Illuminance with stretching

The illuminance of the HLEC also increases as the device is stretched. We attribute this change to two interrelated phenomena: i) the increase in electric field (E) as d decreases, and ii) the decrease in areal number density of phosphor particles (η) as A increases. Starting with the Alfrey-Taylor equation (Eq. SB.13, Fig. SB.3) (*29*), we predict the scaling law in Equation B.1 by expressing $E/E0$ as a function of the principal stretches and by correcting for the change in η with stretching ($\eta/\eta_0 \propto A_0/A$) (supplementary text

below). The predicted trend is shown alongside luminescence measurements in Figure B.2C.

$$\frac{I}{I_0} = (\lambda_1\lambda_2)^{-1} exp\left[5.84\left(1-{\lambda_3}^{1/2}\right)\right] \quad \text{(B.1)}$$

B.5 Crawling Robot

To demonstrate our ability to monolithically integrate the HLEC into soft systems, we embedded three HLEC panels in a crawling soft robot by bonding six layers together. The top four layers comprise the electroluminescent skin, while the bottom two are used for pneumatic actuation (Fig. B.4A). Inspired by architectures developed for mobile soft robots (*30*), our pneumatic actuator uses a series of inflatable chambers embedded in silicone with a bottom layer comprised of inextensible fiber-elastomer composite (*28*). The inextensible layer induces a net bending moment as the pneumatic chambers are inflated; the resulting curvature is exploited to create an undulating gait.

B.5.1 Proprioception & exteroception

The crawling robot uses its HLEC skin to sense its physical state and environment (i.e. proprioception and exteroception). The capacitance of the HLEC changes with pneumatic actuation (Fig. B.4B) and externally applied pressure (Fig. B.4C, D). Actuation of the three underlying pneumatic chambers results in capacitance changes (ΔC) of up to 1,000% when the chambers are fully inflated. Additionally, each HLEC panel is largely decoupled from the state of the surrounding pneumatic chambers (Fig. SB.4) (*28*). The ability to identify the actuated state of the robot using the capacitive sensor readings enables proprioception.

To demonstrate the tactile sensing capabilities of the electronic skin, we pressed each of the HLEC panels on the robot and measured the capacitive response (Fig B.4C). A

firm finger press resulted in a ~25% increase in capacitance. The relative capacitance versus applied pressure, ranging from 0.9 kPa to 30.9 kPa, remains nearly constant over a period of 120 hours (Fig. B.4D).

Arrays of these tactile sensors enable exteroception in soft robotic systems. An array of three HLEC panels patterned into the three-chambered crawling robot enables eight distinct illuminated states (Fig. B.4E). The embedded HLEC remains functional as the robot is actuated through its crawling sequence (Fig. B.4F, Movie SB.3). During actuation, the embedded HLEC undergoes stretches of $\lambda 1 = 2.63$ and $\lambda 2 = 2.42$ in the longitudinal (front to rear) and transverse (side to side) directions, respectively, to produce a ~635% increase in the skin's surface area (Fig. SB.5). Similar to the single-panel HLEC (Movie S B.1), the luminescence of the embedded skin increases during actuation as its thickness is decreased.

B.6 Conclusion

Integrating these highly stretchable and compliant displays into soft actuators enables two new capabilities in soft electronics: (i) displays that actively change their shape and (ii) robots that actively change their color. Using replica molding we easily fabricated a multi-pixel array of individually addressable HLECs, and used the same process to monolithically integrate these displays into a soft robot capable of changing posture. The HLEC array imparts both dynamic coloration and the potential for feedback control, which would be useful in epidermal electronics (*31*) and robotics (*32*). While the luminous efficacy of our HLEC (43.2 mlm W^{-1}) is not as high as commercial AC powder electroluminescent devices (~4 lm W^{-1}) (32), it can be greatly improved by tuning the materials system and device architecture (e.g., higher transmissivity encapsulation layers, reduced thickness, optimized particle size). For applications requiring higher display resolution, HLECs could be made compatible with photolithography and other microfabrication techniques by using photo-polymerizable polymers. These techniques

would also allow us to decrease the thickness of the electroluminescent layer, thereby reducing the voltage required to power the HLEC.

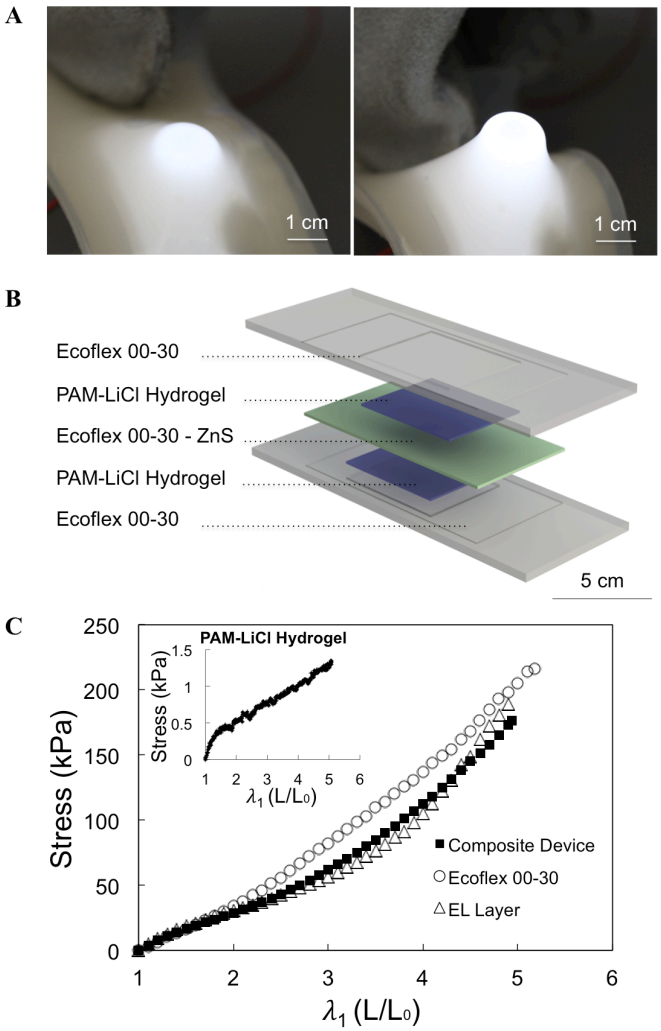

Figure B.1| Hyperelastic light emitting capacitor (HLEC). (A) Image of the HLEC conforming to the end of a pencil. (B) Exploded view of the HLEC showing its five-layer structure consisting of a ~1 mm thick electroluminescent layer (ZnS-Ecoflex 00-30) that is sandwiched between two PAM-LiCl hydrogel electrodes and encapsulated in Ecoflex 00-30. (C) Stress-stretch curves of Ecoflex 00-30, the electroluminescent layer, and the composite device. The hydrogel data is shown in the inset due to its much lower elastic modulus.

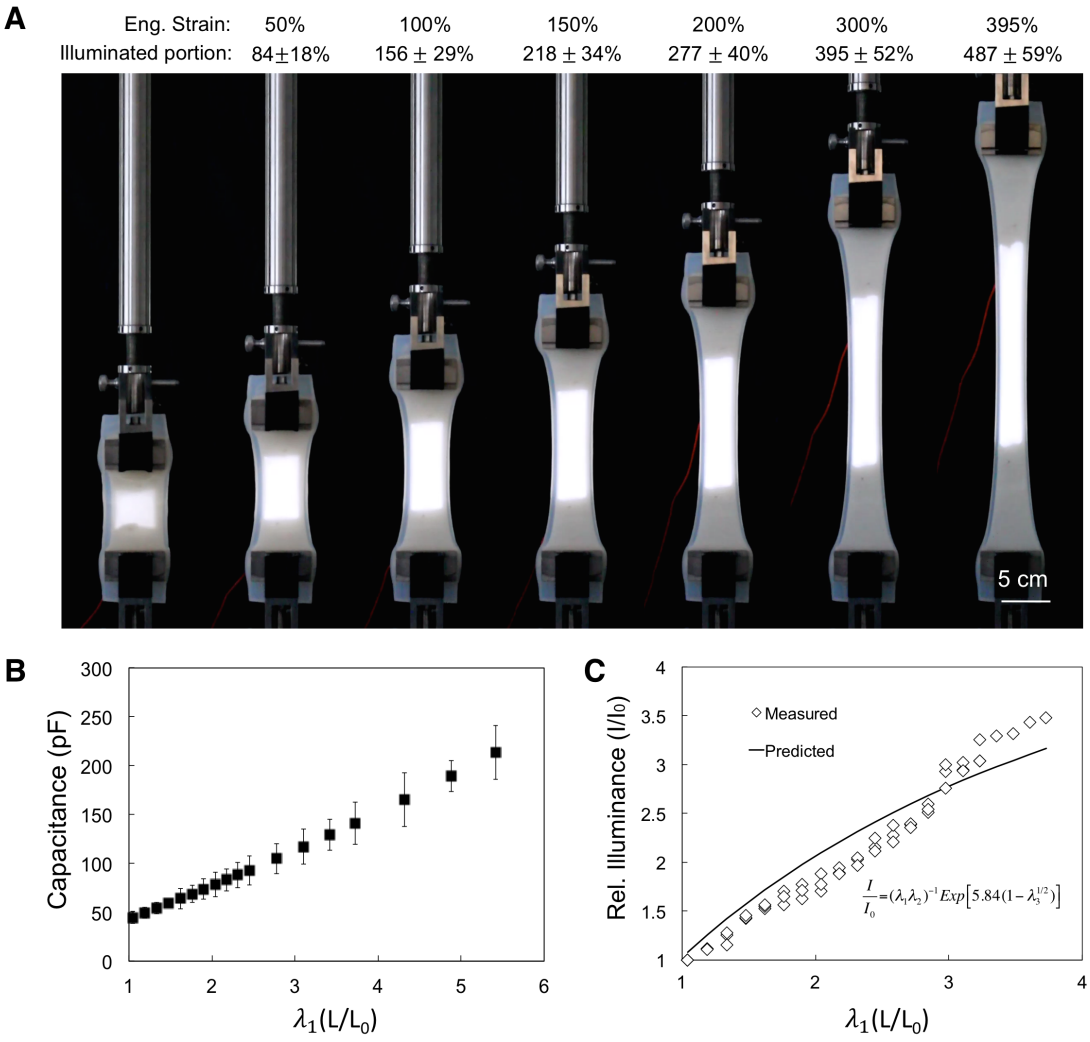

Figure B.2| The capacitive and luminescent behavior of the HLEC display under uniaxial stretching. (A) A nominal electric field of ~25 kV cm-1 was applied to the HLEC at the start of the uniaxial test. Five lengths were measured using image analysis software to obtain $\lambda 1$ across the width of the illuminated portion of the tensile bar. We report the mean and standard deviation of those measurements. At an engineering strain (grip-to-grip) of 395%, we measured the mean strain of the illuminated portion to be 487%, with a range of 420 - 549%. (B) The capacitance of the HLEC as a function of its uniaxial stretch (n = 4). (C) The relative illuminance of the HLEC versus its uniaxial stretch (n = 4) plotted alongside predicted values (supplementary text).

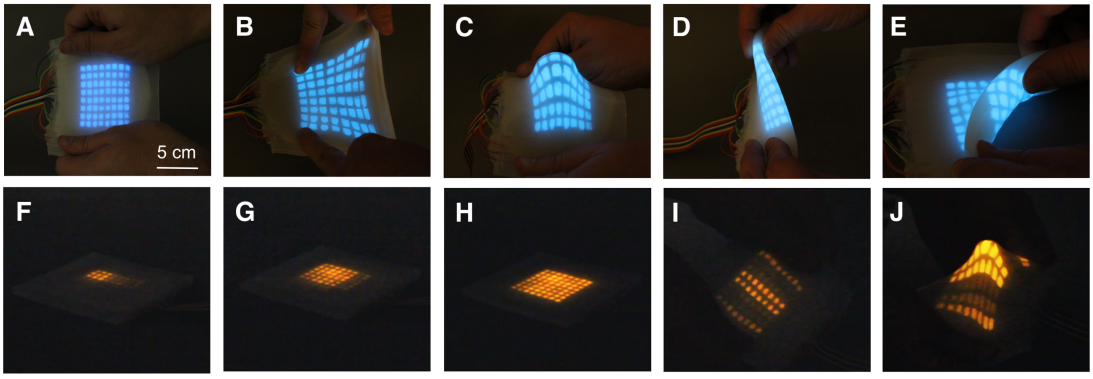

Figure B.3| Multi-pixel electroluminescent displays fabricated via replica molding. The device measures 5 mm thick, with each of the 64 pixels measuring 4 mm. We show the devices in various states of deformation and illumination: (A) undeformed, (B) stretched, (C) wrapped around a finger, (D) folded, (E) rolled, (F-H) subsets of pixels activated, and (I-J) subsets of pixels activated while being deformed.

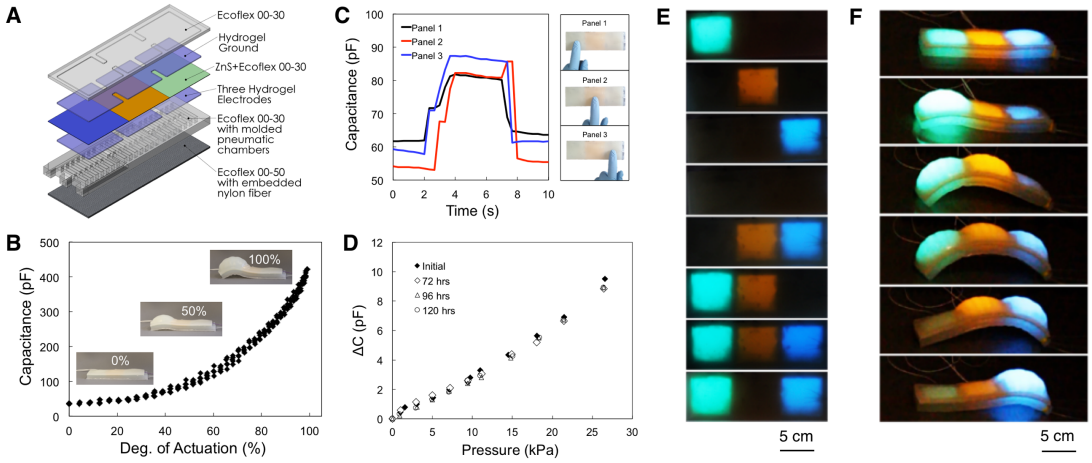

Figure B.4| HLEC skins endow soft robots with the ability to sense their actuated state, environment, and communicate optically. (A) Schematic of a three-chambered soft robot. A series of three independently actuated pneumatic chambers are embedded between the HLEC skin (top) and a strain limiting layer (bottom). (B) Capacitance plotted versus the actuation amplitude, defined as the relative change in deflection between the uninflated and fully inflated states (n = 5). (C) A firm finger press induces a ~25% increase in capacitance. (D) Change in capacitance versus applied pressure. We

observe a negligible change in the capacitive response of the sensors over a period of 120 hours. (E) Array of three HLEC panels, each emitting a different wavelength through selective doping of the EL phosphor layer. Each HLEC panel is activated independently. (F) An undulating gait is produced by pressurizing the chambers in sequence along the length of the crawler. This sequence produces forward locomotion at a speed of ~4.8 m hr-1 (~32 body lengths hr-1). As each pneumatic chamber is pressurized, the outer electroluminescent skin is stretched, increasing the electric field across the EL layer and thus the luminescence.

Supplemental Information is available in the online version of the paper.

REFERENCES

1. A. Barbosa, J. J. Allen, L. Mäthger, R. T. Hanlon. Hanlon, Cuttlefish use visual cues to determine arm postures for camouflage. *P. R. Soc. B-Biol. Sci.* 279, 84-90 (2012).
2. F. Ilievski, A. D. Mazzeo, R. F. Shepherd, X. Chen, G. M. Whitesides. Soft robotics for chemists. *Angew. Chem. Int. Ed.* 50, 1890-1895 (2011).
3. D. Russ, M. Tolley. Design, fabrication and control of soft robots. *Nature* 521, 467-475 (2015).
4. M. J. Spenko, G. C. Haynes, J. A. Sanders, M. R. Cutkosky, A. A. Rizzi. Biologicallyinspired climbing with a hexapedal robot. *J. Field Robot.* 25, 223-242 (2008).
5. E. Kreit *et al*., Biological versus electronic adaptive coloration: how can one inform the other? *J. R. Soc. Interface* 10 (2013).
6. J. A. Rogers, T. Someya, Y. Huang. Materials and mechanics for stretchable electronics. *Science* 327, 1603-1607 (2010).
7. S. A. Morin *et al*., Camouflage and display for soft machines. Sci*ence* 337, 828-832 (2012).
8. Q. Wang, G. R. Gossweiler, S. L. Craig, X. Zhao. Cephalopod-inspired design of electromechano-chemically responsive elastomers for on-demand fluorescent patterning. *Nat.Commun.* 5, 4899 (2014).
9. C. Yu *et al*., Adaptive optoelectronic camouflage systems with designs inspired by cephalopod skins. *Proc. Natl. Acad. Sci. U.S.A.* 111, 12998-13003 (2014). 10. P. E. Burrows *et al*., Ultra barrier flexible substrates for flat panel displays. *Displays* 22, 65-69 (2001).
11. T. H. Han *et al*., Extremely efficient flexible organic light-emitting diodes with modified graphene anode. *Nat. Photonics* 6, 105-110 (2012).
12. T. Sekitani *et al*., Stretchable active-matrix organic light-emitting diode display using printable elastic conductors. *Nat. Mater.* 8, 494-499 (2009).

13. M. K. Shin *et al*., Elastomeric conductive composites based on carbon nanotube forests. *Adv. Mater.* 22, 2663-2667 (2010).
14. M. S. White *et al*., Ultrathin, highly flexible and stretchable PLEDs. *Nat. Photonics.* 7, 811-816 (2013).
15. L. Hu, H. S. Kim, J. Y. Lee, P. Peumans, Y. Cui. Scalable coating and properties of transparent, flexible, silver nanowire electrodes. *ACS Nano* 4, 2955-2963 (2010).
16. J. Liang, L. Li, X. Niu, Z. Yu, Q. Pei. Elastomeric polymer light-emitting devices and displays. *Nat. Photonics* 7, 817-824 (2013).
17. T. Someya *et al*., Conformable, flexible, large-area networks of pressure and thermal sensors with organic transistor active matrixes. *Proc. Natl. Acad. Sci. U.S.A.* 102, 12321-12325 (2005).
18. K. Takei *et al*., Nanowire active-matrix circuitry for low-voltage macroscale artificial skin. *Nat. Mater.* 9, 821-826 (2010).
19. T. Someya *et al*., A large-area, flexible pressure sensor matrix with organic field-effecttransistors for artificial skin applications. *Proc. Natl. Acad. Sci. U.S.A.* 101, 9966-9970 (2004).
20. Y. L. Park, B. R. Chen, R. J. Wood. Design and fabrication of soft artificial skin using embedded microchannels and liquid conductors. *IEEE Sens. J.* 12, 2711-2718 (2012).
21. D. P. J. Cotton, I. M. Graz, S. P. Lacour. A multifunctional capacitive sensor for stretchable electronic skins. *IEEE Sens. J.* 9, 2008-2009 (2009).
22. C. Keplinger *et al*., Stretchable, transparent, ionic conductors. *Science* 341, 984-987 (2013).
23. J. Y. Sun *et al*., Highly stretchable and tough hydrogels. *Nature* 489, 133-136 (2012).
24. J. Y. Sun, C. Keplinger, G. M. Whitesides, Z. Suo. Ionic skin. *Adv. Mater.* 26, 7608-7614 (2014).
25. A. Kitai. *Luminescent Materials and Applications* (Wiley, West Sussex, 2008), pp. 249-268.

26. R. F. Shepherd, A. A. Stokes, R. M. D. Nunes, G. M. Whitesides. Soft machines that are resistant to puncture and that self seal. *Adv. Mater.* 25, 6709-6713 (2013).

27. Y. Bai *et al*., Transparent hydrogel with enhanced water retention capacity by introducing highly hydratable salt. *Appl. Phys. Lett.* 105, 151903 (2014).

28. G. F. Alfrey, J. B. Taylor. Electroluminescence in single crystals of zinc sulphide. *Proc. Phys. Soc. B* 68, 775 (1955).

29. R. F. Shepherd *et al*., Multigait soft robot. *Proc. Natl. Acad. Sci. U.S.A.* 108, 20400-20403 (2011).

30. D. H. Kim *et al.*, Epidermal electronics. *Science* 333, 838-843 (2011).

31. J. Kim *et al*., Stretchable silicon nanoribbon electronics for skin prosthesis. *Nature Commun.* 5 (2014).

32. A. T. Conn, J. Rossiter. Smart radially folding structures. *Mechatronics, IEEE/ASME Trans.* 17, 968-975 (2012).